AALBORG UNIVERSITY

Design of an Internal Down-Lead System for a 400 kV Composite Tower and Investigation of Lightning Performance

Yin, Kai

Publication date:
2022

Document Version
Publisher's PDF, also known as Version of record

Link to publication from Aalborg University

DESIGN OF AN INTERNAL DOWNLEAD SYSTEM FOR A 400 KV COMPOSITE TOWER AND INVESTIGATION OF LIGHTNING PERFORMANCE

BY
KAI YIN

DISSERTATION SUBMITTED 2022

AALBORG UNIVERSITY
DENMARK

Design of an Internal Down-Lead System for a 400 kV Composite Tower and Investigation of Lightning Performance

Ph.D. Dissertation
Kai Yin

Dissertation submitted November, 2022

Curriculum Vitae

Kai Yin

Kai Yin was born in Jinzhong, Shanxi province, P. R. China in October 1991. He received his B.Sc. degree in Electrical Engineering from North China Electric Power University, Hebei, China, in 2015. Receiving his M.Sc. degree in High Voltage and Insulation Technology from North China Electric Power University, Beijing, China, in 2018. He is currently pursuing a Ph.D. degree at the Department of Energy, Aalborg University, Aalborg, Denmark. His research interests include lightning protection, insulating materials, and flashover mechanism.

Abstract

The recent development of modern renewable energy and the growing electrical power system bring a huge demand for environmentally friendly transmission lines. Aiming to this goal, the 'Power Pylons of the Future (PoPyFu)' project designed an innovative composite material pylon with a 'Y' shape profile for 400 kV AC transmission lines. This pylon consists of lightweight composite materials and has a compact configuration. Compared with the conventional pylons made of steel, the composite pylon requires less right-of-way, lower manufacturing cost, fewer maintenance efforts, and presents an attractive appearance. Meanwhile, this kind of pylon has been confirmed to possess a perfect lightning shielding performance due to its special structure. With these attractive advantages, this pylon is believed to be a promising candidate as a next-generation of transmission tower.

However, the down-lead configuration, which directly concerns the transmission pylon safe operation when lightning strikes the tower, has not been determined. In this project, a conductor going through the hollow cross-arm and pylon body is proposed as the down-lead system. In order to inhibit the partial discharge inside the pylon, the gap between the down-lead and cross-arm is filled with a suitable insulating material. Based on this down-lead scheme, the Ph.D. research work mainly focuses on the optimization of the down-lead system, insulation verification, and proposing empirical formulas to estimate the backflash critical current for this novel pylon. The primary research contents are summarized as follows:

The lightning performance of the pylon with the conductor passing through the filled cross-arm and pylon body as a down-lead system has been studied. The electromagnetic transient (EMT) model is established in PSCAD/EMTDC to obtain the transient response to lightning surges. In the modeling of the equivalent circuit, the surge impedance of the inclined down-lead circumscribed by composite materials is expressed in integral form and validated by the Finite Element Method (FEM). In addition, the mutual coupling effect between separated down-leads and the parasitic capacitance is considered. The simulation results show that the lightning performance of the Y-shaped pylon is worse than that of conventional steel Eagle and Donau towers at the same voltage level, and the down-lead system is needed to be optimized to improve the composite pylon's lightning performance. Then, potential multi-factors that may affect the lightning performance have been studied including the downlead configu-

ration, pylon span, the permittivity of the filling material, and parasitic capacitances. The results show that the configuration of the down-lead has a large influence on the lightning performance, but the effect of the filling material can be neglected. Finally, two down-leads through cross-arms and connecting with a steel mast are proposed as the optimal grounding form. With this optimized down-lead system, the backflashover rate of the Y-shaped pylon is much lower than that of these traditional steel ones.

To make the cross-arm lightweight and easier to assemble, the cable as down-lead through a hollow cross-arm is proposed as the next step of the optimization strategy. The feasibility of this scheme is investigated from the perspectives of electrical insulation and lightning performance. Based on experimental tests on a scaled cross-arm model combined with the electrostatic simulation, the corona inception characteristic as a function of the cable radius is obtained. In addition, the impact of the corona under switching overvoltage on the cable down-lead has also been evaluated. Then, the appropriate cable dimensions to meet the insulation requirements are determined. Considering the corona sheath around the cable, the lightning critical current is obtained through the EMT simulation. The cable down-lead insulation strength under lightning impulse overvoltage has been verified by impulse test on the scale cross-arm combined with the FEM simulation. The research shows that the pylon with cable as a down-lead has satisfying insulation properties and lightning performance, and the design of cable used as a down-lead is feasible for a Y-shaped composite pylon.

Since the down-lead configuration of the composite pylon is different from the traditional lattice tower, it is necessary to improve empirical formulas to realize a fast lightning performance estimation for this novel pylon. First, the equivalent circuit of the down-lead system is simplified to facilitate expression by formulas. Then, the bifurcation structure of the down-lead is considered in the expression. Based on the lattice diagram method originally proposed in CIGRE Technical Brochure 63, the new formulas are derived and modified to be applied for both Y composite and traditional steel towers. Compared with the original method, the results obtained by this improved method demonstrate a fairly good agreement with the simulation results for both traditional and composite towers. The critical current at the full range of front time is obtained, and the errors for the Y-shaped pylon by the new method are restricted within 13 %, while the error of the CIGRE original method exceeds 23 % when the lightning front time is in the 97.5 % confidence interval. Finally, the Monte Carlo procedure proves the superiority of the new empirical formulas.

In summary, in this Ph.D. project, efforts have been made to design and validate the down-lead system for the Y-shaped composite pylon. Meanwhile, new empirical formulas are proposed to realize the rapid lightning performance evaluation. The Ph.D. work is of great significance for the design and application of Y-shaped composite pylons in electrical engineering.

Resumé

Den seneste udvikling af moderne vedvarende energi og det voksende elektriske kraftsystem medfører en enorm efterspørgsel efter miljøvenlige transmissionsledninger. Med sigte på dette mål designede 'Power Pylons of the Future (PoPyFu)'-projektet en innovativ kompositmateriale-pylon med en 'Y'-profil til 400 kV AC-transmissionslinjer. Denne pylon består af lette kompositmaterialer og har en kompakt konfiguration. Sammenlignet med de konventionelle pyloner lavet af stål kræver den sammensatte pylon mindre vigepligt, lavere produktionsomkostninger, færre vedligeholdelsesindsatser og fremviser et attraktivt udseende. I mellemtiden er det blevet bekræftet, at denne type pylon har en perfekt lynafskærmningsydelse på grund af dens specielle struktur. Med disse attraktive fordele menes denne pylon at være en lovende kandidat som næste generation af transmissionstårn.

Den nedadgående konfiguration, som direkte vedrører transmissionspylonens sikker drift, når lynet rammer tårnet, er dog ikke fastlagt. I dette projekt foreslås en leder, der går gennem den hule tværarm og pylonlegemet som down-lead system. For at forhindre den delvise udledning inde i pylonen, fyldes mellemrummet mellem ned- og tværarm med et passende isoleringsmateriale. Baseret på denne down-lead-ordning vil ph.d. Forskningsarbejdet fokuserer hovedsageligt på optimering af down-lead-systemet, isoleringsverifikation og forslag til empiriske formler til at estimere den kritiske tilbageslagsstrøm for denne nye pylon. Det primære forskningsindhold er opsummeret som følger:

Lynydelsen af pylonen med lederen, der passerer gennem den fyldte tværarm og pylonkroppen som et nedadgående system, er blevet undersøgt. Den elektromagnetiske transient (EMT)-model er etableret i PSCAD/EMTDC for at opnå den transiente reaktion på lynstød. I modelleringen af det ækvivalente kredsløb udtrykkes overspændingsimpedansen af den skrå nedadgående ledning omgivet af kompositmaterialer i integral form og valideres af Finite Element Method (FEM). Derudover overvejes den gensidige koblingseffekt mellem adskilte down-leads og den parasitære kapacitans. Simuleringsresultaterne viser, at lynydevnen af den Y-formede pylon er dårligere end konventionelle stål Eagle- og Donau-tårne på samme spændingsniveau, og down-lead-systemet skal optimeres for at forbedre kompositpylonens lynydevne. Derefter er potentielle multifaktorer, der kan påvirke lynets ydeevne, blevet undersøgt, herunder downlead-konfigurationen, pylonspænd, permittiviteten af fyldmaterialet og para-

sitære kapacitanser. Resultaterne viser, at konfigurationen af down-lead har stor indfly-
delse på lynets ydeevne, men effekten af fyldmaterialet kan negligeres. Til sidst fores-
lås to nedadgående ledninger gennem tværarme og forbindelse med en stålmast som
den optimale jordingsform. Med dette optimerede down-lead-system er backflashover-
hastigheden af den Y-formede pylon meget lavere end for disse traditionelle stål.

For at gøre tværarmen let og nemmere at samle, foreslås kablet som nedføring gen-
nem en hul tværarm som næste trin i optimeringsstrategien. Gennemførligheden af
denne ordning undersøges ud fra perspektiverne af elektrisk isolering og lynydeevne.
Baseret på eksperimentelle tests på en skaleret tværarmsmodel kombineret med den
elektrostatiske simulering opnås korona-indledningskarakteristikken som funktion af
kabelradius. Derudover er indvirkningen af den transiente korona under skiftende over-
spænding på kablets nedadgående ledning også blevet evalueret. Derefter bestemmes
de passende kabeldimensioner for at opfylde isoleringskravene. I betragtning af ko-
ronakappen omkring kablet opnås den lynkritiske strøm gennem EMT-simuleringen.
Kablets nedadgående isoleringsstyrke under lynimpulsoverspænding er blevet verifi-
ceret ved impulstest på skalaens tværarm kombineret med FEM-simuleringen. Un-
dersøgelsen viser, at pylonen med kabel som down-lead har tilfredsstillende isoler-
ingsegenskaber og lynydeevne, og designet af kabel, der anvendes som down-lead, er
gennemførligt for en Y-formet komposit pylon.

Da den nedadgående konfiguration af den sammensatte pylon er forskellig fra det
traditionelle gittertårn, er det nødvendigt at forbedre empiriske formler for at realis-
ere en hurtig lyn-ydeevnevurdering for denne nye pylon. For det første forenkles det
ækvivalente kredsløb i down-lead-systemet for at lette udtryk ved formler. Derefter be-
tragtes bifurkationsstrukturen af ned-ledningen i udtrykket. Baseret på gitterdiagram-
metoden, der oprindeligt blev foreslået i CIGRE Technical Brochure 63, er de nye
formler udledt og modificeret til at blive anvendt til både Y-komposit- og traditionelle
ståltårne. Sammenlignet med den oprindelige metode viser resultaterne opnået ved
denne forbedrede metode en ret god overensstemmelse med simuleringsresultaterne
for både traditionelle og sammensatte tårne. Den kritiske strøm ved hele fronttidsom-
rådet opnås, og fejlene for den Y-formede pylon ved den nye metode begrænses inden
for 13 %, mens fejlen i CIGRE originalmetoden overstiger 23 %, når lynet fronttid
er i 97,5 % konfidensintervallet. Endelig beviser Monte Carlo-proceduren de nye em-
piriske formlers overlegenhed.

Sammenfattende er det i denne ph.d. projekt er der blevet gjort en indsats for at
designe og validere down-lead-systemet til den Y-formede kompositpylon. I mellemti-
den foreslås nye empiriske formler for at realisere den hurtige lyn-ydelsesevaluering.
Ph.D. arbejde har stor betydning for design og anvendelse af Y-formede kompositpy-
loner i elektroteknik.

Preface

This Ph.D. thesis summarizes the outcomes from the Ph.D. project entitled "Design of an Internal Down-Lead System for a 400 kV Composite Tower and Investigation of Lightning Performance", which is supported by AAU Energy, Aalborg University, Denmark, Chinese Scholarship Council, and Otto Mønsteds Fond, Denmark. I would like to express my acknowledgment to the above institutions to support me in the conference participation and study abroad during my Ph.D. study.

This Ph.D. project was done under the supervision of Prof. Claus Leth Bak, Assoc. Prof. Filipe Miguel Faria da Silva, and Assist. Prof. Qian Wang. First, I would like to express my sincere gratitude to my supervisor Prof. Claus Leth Bak, for his guidance, encouragement, and valuable suggestions during my Ph.D. period. I would also like to thank my co-supervisors Filipe Miguel Faria da Silva and Qian Wang. The completion of the present thesis is attributed to their insightful suggestions and patient revision. Then, I would like to sincerely thank Prof. Xiangrong Chen for providing me an opportunity to visit the Zhejiang University, Hangzhou, China, where I have broadened my knowledge in many aspects and collaborated with my colleagues there on experiments and papers. My special gratitude goes to Prof. Chen and colleagues at Zhejiang University, for their kind help in my Ph.D. research.

Also, I would like to thank all my colleagues at AAU energy, Aalborg University for their help and support, as well as for the living environment and the endless friendship. Thanks to Zhengfa Zhang, Zhaoxin Wang, and Mohammad Ghomi for their scientific assistance and help in daily life. I would personally give my tremendous appreciation to my friends Tianbao Gu, Wei Fan, Cheng Chi, Weiheng Zhang, Wenyuan Cao, and Yuchen Fang for always being there for me and wonderful time together in Aalborg. Sincere thanks to my roommate as well as office mate Hanchi Zhang for the three-year companion and help.

In the end, I would like to extend my deep gratitude to my family for their unconditional love and care, which are the source of my energy. Thanks my girlfriend Yirui Yang for your encouragement, trust, and waiting. Thanks for the happiness and precious memory you bring to me. With all of your love, my world has become complete.

Kai Yin
Aalborg University, November 17, 2022

Contents

Contents

Report

Chapter 1

Introduction

The lightning performance of a transmission pylon is directly related to the safe operation of the whole transmission system [1, 2]. The reasonable and reliable design of the transmission pylon down-lead systems is of great significance for transmission line protection in engineering practice [3]. This chapter starts with the background and motivations of this Ph.D. project, which aims to estimate the lightning performance of the novel Y-shaped pylon for future overhead lines (OHLs). Subsequently, the state of the art for composite transmission towers and the research problems are demonstrated. Finally, the Ph.D. project objectives and research activities are described and the outlines of the present Ph.D. thesis are also given.

1.1 Background

1.1.1 Growing Demand for Transmission Lines

In the past decades, the statistical review of world energy production and consumption reveals that the global energy demand is undergoing exponential growth (Fig. 1.1) [4, 5]. Meanwhile, due to the gradual depletion of fossil-based energy, the exploration and use of green energy sources such as offshore wind and solar power are booming. At the same time, there is a huge demand for transmission line construction to ensure continuous access to electricity. Due to the decentralized nature of the distribution of renewable energy, expansion of the power system and transmission lines is necessary to realize energy resources dispatch geographically.

To date, approximately 44,700 km of new or refurbished transmission lines are needed in Europe by 2030 [6]. According to the report issued by the European Network of Transmission System Operators (ENTSO-E), 35 GW of transmission capacity is currently in the process of planning and construction (Fig. 1.1) [7]. This plan puts Europe on track to realize the Green Deal and brings huge economic and environmental benefits including 110 TWh energy savings, a decrease of generation cost of 4

billion € and 55 Mtons of CO_2 emissions avoided each year until 2040.

Extra High Voltages (EHV) OHLs are applicable for long-distance and high-capacity transmission, and 400 kV EHV transmission lines with alternative voltage are major options for expansion and upgrading of power networks due to well-established manufacturing techniques and abundant operation experience. However, the construction of a large number of OHLs and conventional steel towers will attract environmental concerns from aspects of corridors, land use, electromagnetic interference, and visual impacts [8]. CIGRE has recommended the design of a new transmission tower with a compact pattern and limited environmental impact to mitigate these issues [9].
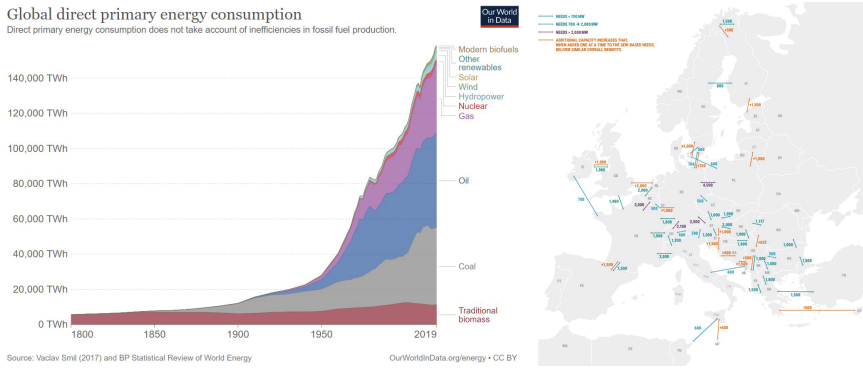
Fig. 1.1: Global primary energy consumption in past 200 years (left) [4]. Needs for transmission capacity increases identified in the 2030 horizon (right) [7].

1.1.2 Advantages of 'Y' Composite Tower

With the development of material science and manufacturing technology, a composite tower made of Fiber Reinforced Plastic (FRP) as an alternative to the conventional tower has drawn more and more attention. According to the project of 'Power Pylons of the Future' [10], a fully composite pylon has been proposed to adapt to the trend of installing new environmental-friendly overhead lines. Figure 1.2 shows the appearance of the fully composite pylon, which is designed to carry double-circuit 400 kV AC lines. This pylon has an axially symmetric structure of a 'Y' shape with integrated cross-arms without insulator strings. The cross-arm is comprised of the FRP tube, polymeric weather sheath/sheds, and metallic end fittings. Phase conductors are attached to the cross-arm directly by specially designed non-conductive clamps. In order to protect the phase conductors from lightning strokes, two shield wires are attached to the tips of the pylon. Compared with the steel tower, there are numerous merits of the composite tower as follows:

- **Compact configuration** - The composite material is more reliable and lightweight for enabling advanced geometries and realizing miniaturization. It is easy to transport, lift, assemble and install.

Fig. 1.2: The concept map of the Y-shaped pylon proposed by 'Power Pylons of the Future' [11].

- **Environmentally friendly** - The composite pylon has a small footprint and requires less right-of-way. Meanwhile, the compact structure means the limited interference of the electromagnetic field generated.

- **Fewer maintenance efforts** - Anti-UV resin blended with high-performance glass fiber has been entrusted with excellent aging resistance properties for the FRP composite. Composite poles are unaffected by rust, termites, woodpeckers, and vermin, and have an expected service life of 80 years even in harsh environments [11].

- **Better lightning performance** - Compared with the standard steel tower, the composite tower has a lower height and narrower corridor width, which means the composite pylon has a lower probability of being struck by lightning. In addition, the lightning protection angle of a composite pylon is normally smaller than that of the traditional tower, which allows the pylon to present a better lightning shielding performance [12].

- **Attractive appearance** - The composite pylon is designed to have a positive appearance.

1.2   State of the Art

1.2.1   Development of Composite Pylon

The earliest composite pylons can be traced back to the 1960s [13]. However, as initial composite pylons are mainly made from resin-based polymers which have poor anti-aging performance and relatively short service lifetime, they have not been used in a large scope [14]. With the progress of material science and technology, composite pylon has again drawn people's attention [13]. Carbon fiber, glass fiber, nylon66, and hybrid fiber are used as reinforcing materials into epoxy resin to strengthen the tower

body [15]. Pultrusion and filament winding processes are used to produce the material, and the performance of composite pylon has been improved [13].

To date, the mainstream composite tower structure can be classified into two types: lattice towers and pole towers. In 1996, Ebert Composites Corporation designed a kind of composite lattice tower for 230 kV OHLs on the south coast of California (Fig. 1.3). The tower body retains the conventional lattice tower pattern and the bracings are made of FRP instead of steel to constitute the main structure. This composite tower can be easily assembled and erected due to only one-third of the weight of the same size steel tower. The composite lattice tower is always applied in transmission OHLs with high voltage levels. According to the operation report, the tower performed exceptionally well in the highly-corrosive coastal area over 10 years [16].

Fig. 1.3: The 230 kV composite transmission tower built by Ebert [16].

The pole tower is originally applied for a medium voltage distribution system. Ebert company employed a pultrusion technique and produced a kind of fiberglass composite pole with good load capacity and substantially lighter weight. The tapering pole is mounted with three insulators and applied as the utility pole (Fig. 1.4) [17].

In 2009, State Grid Corporation of China initiated the research of a composite cross-arm project, in which glass fiber reinforced polyurethane composite pole with composite cross-arms for a 110 kV transmission line was designed and operated since 2010 (Fig. 1.5(a)) [18]. In order to strengthen the mechanical property of the tower body, double poles are crossing fixed and erected in certain areas. RS Technologies Inc. also adopted the same strategy to design a kind of commercialized FRP tower with two poles [19] in Fig. 1.5(b).

Fig. 1.4: The composite utility poles produced by Ebert corporation [17].

(a)   (b)

Fig. 1.5: (a) 110kV composite towers are composed of a single pole (left) and double-pole (right) [18]. (b) Double-pole pylon manufactured by RS Technologies Inc. [19].

With the further improvement of the mechanical properties of composites, the single-pole tower is used in EHV transmission lines. In recent years, the Dutch TSO TenneT company proposed an innovative tower concept as shown in Fig. 1.6 [20]. The Wintrack II tower has a column installed with composite cross-arms. Each composite cross-arm is comprised of two post insulators, which provide mechanical support and electrical insulation for conductors. In 2018, two 380 kV line sections were built between the towns of Bleiswijk and Beverwijk in the Netherlands using these innovative pylons [21].

Fig. 1.6: Wintrack II towers designed by Dutch TSO TenneT [21].

The current development trend of the composite pylon is directed toward compact patterns and EHV application. The composite lattice tower has the advantage of good mechanical performance and can be applied for a wide range of voltage levels of transmission lines. However, the lattice towers have large foundations and occupy more land. Taking a 400 kV lattice tower as an example, the width of the foundation ranges from 5 m to 8.5 m [22–26]. While for the pole tower, it has a relatively small footprint, and the radius of the pole foundation is normally no more than 1.5 m [25]. Due to the advanced production technique, nowadays the composite pole is fully competent as an EHV transmission tower. With the concern of right-of-way and visual impact, the unibody pole tower such as the 400 kV Y-shaped tower with a small footprint and aesthetical appearance studied in the Ph.D. research, has great potential to become the next generation transmission pylon.

1.2.2 Composite Pylon Components

A. Composite Pylon Body

The composite lattice tower body consists of hollow square tubular FRPs, which are assembled by pinned truss connections, steel plates, and end clamps. Mechanical fasteners are used to fix the cross-arms and join the tower legs. Central Power Research Institute in India has performed a mechanical load test on a 66 kV full-scale lattice tower and found that the tower has a better mechanical performance than a steel tower at the condition of 17% right-of-way and 16% height saved [27].

Composite poles commonly contain multi-layers. Inner layers are manufactured with a high-performance thermoset resin to ensure adequate toughness and strength, and the matrix is strengthened by electrical grade E-glass /carbon reinforcements in the form of unidirectional roving. The external pole is covered by UV protected veil. Both ends of the pole are sealed by caps not only to avoid condensation but also to prohibit the hollow pole from shearing into the soil [28]. Sometimes the lower half of the pole is made of steel and connects with the shield wires by a vertical conductor to improve the lightning performance (Fig. 1.5(a)).

B. Cross-Arm

The cross-arm plays a role in bearing the mechanical stress and preventing flashover between phase conductors. Based on the structure, the composite cross-arm is mainly divided into two classifications: hollow inflatable cross-arm and filled cross-arm. The hollow cross-arm has a relatively simple preparation process, a shorter manufacturing cycle, a lower cost and conveniently manual installation [29]. A hollow cross-arm is often used as a post insulator in lattice towers. Due to its limited transverse loading capacity, the hollow cross-arms commonly serve as compression members and are anchored together with tension insulators [30, 31]. In some field stress intensity regions, partial discharge may be induced inside the hollow cross-arm. Thus, the cross-arm

filled with insulation materials is used as the alternative. For example, polyurethane foam is always used as filling material for the 750 kV post insulator [32]. Meanwhile, the stuffed cross-arm possesses improved buckling properties and wider application [33]. In reference [34], a composite-filled sandwich structure is proposed to increase the bending and compressive load capacity for cross-arm as depicted in Fig. 1.7.
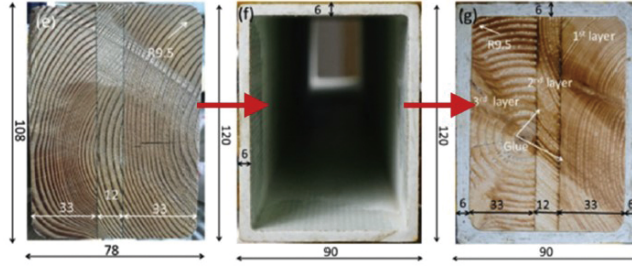
Fig. 1.7: Pultruded FRP beam with wooden sandwich core [34].

Of particular concern is that the presence of the filling materials inside the cross-arm introduces issues with the interface. Due to the characteristic difference between shell and core materials, the interface becomes a vulnerable area, and it is easy to produce partial discharge or even breakdown (Fig. 1.8).

Fig. 1.8: Carbonization channel on the interface of polyurethane foam and FRP after flashover.

To solve this problem, scholars in the field of materials try to prepare polymers with better interface contact stability. Liu *et al*. prepared a ternary blend syntactic foam composed of hollow organic microsphere-filled siliconized epoxy resin in Fig. 1.9(a) [35]. The dielectric constant and dielectric loss of this resin is decreased compared with the pure epoxy matrix, and the thermal stability of the composites is considerably improved owing to the hollow polymer microsphere and grafted siloxane bond. This kind of syntactic foam possesses superior penetration resistance and hydrolysis resistance. Although the breakdown strength decreases with the increase of the microsphere content (Fig. 1.9(b)), the withstand voltage still meets the insulation requirements [31, 36]. However, this filling material has not been used in practice, and it needs to be validated by a long-term operation.

There is a special case where metal components are inside the cross-arm, such as
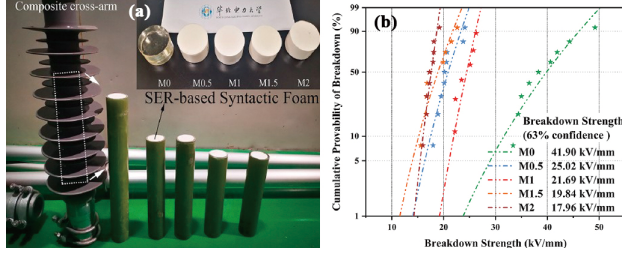
Fig. 1.9: (a) Pictures of real cross-arm, the synthetic foam samples and the poured FRP tubes. (b) Weibull distribution of the breakdown strength of the samples. M*x* indicates that the microsphere filling concentration is *x*% [35].

a conductor passing through the cross-arm studied in this Ph.D. project. The introduction of the metal parts will complicate the electric field around and inside the cross-arm. The corresponding research for the Y-shaped pylon cross-arm has been performed in a previous Ph.D. project [37]. The full-scale model was built in ANASY software, and the Finite Element Method was employed to compute the electric field strength in different places of interest, including the sheath and conductor surface, areas of clamps, and interface of down-lead inside the cross-arm. The simulation results show that the electric field magnitudes on the surface of the down-lead inside the cross-arm exceed the corona onset threshold. In this project, two methods are proposed to solve this issue. One method is selecting an appropriate insulation material as the filling material for the cross-arm, which will be presented in Chapter 2 in details. Another method is attaching an insulation cover for the down-lead, and the feasibility of this way will be discussed in Chapter 4.

C. Housing and Sheds

Insulator housing and sheds are designed to increase the creepage distance and to strengthen the insulator's withstand voltage. Their performance highly depends on profile design, material characteristics, and service environmental conditions [38]. Concerning the material type, the polymer has been increasingly used as insulator housing and sheds due to its lower maintenance cost and better reliability than that of porcelain or glass [38]. According to the operation report and references, silicone rubber (SIR), ethylene propylene diene monomer (EPDM), and a blend of EPDM with silicone rubber are recommended as materials for housing and sheds. In reference [39, 40], dynamic mechanical, thermal, and electrical property tests were carried out on the sheds made of SIR, EPDM, and SIR/EPDM blend rubbers. The tested results showed that SIR has better tensile strength, modulus, and elongation at break, while EPDM has the advantages of higher breakdown strength, surface and volume resistivity, and higher decomposition temperature, but worse in heating aging. By contrast, the blend polymer SIR/EPDM possesses better storage modulus and humidity aging resistivity. Addition-

ally, the surface conditions of 150 kV SIR and EPDM insulator sheds operated in the coastal area for 17 years were assessed through visual inspection, wettability classification, Fourier Transform Infrared spectroscopy, morphology analysis, and Energy Dispersive X-Ray analysis by N.C. Mavrikakis and P.N. Mikropoulos [38]. The details of suspension insulators with SIR and EPDM sheds are shown in Fig. 1.10. They found that the anti-tracking and erosion performances of these materials are almost unaffected by field aging and proposed removing pollutant deposits as an effective maintenance strategy to restore the shed performance (Fig. 1.11). A similar conclusion was drawn in reference [41] that the intense electric field and water droplet corona hardly result in SIR housing degradation and erosion even in a long-term operation.

Insulator	A		B	
150 kV Line	L–M		L–C II	
Pollution severity IEC 60815	Light		Medium	
Age in service	17 years		17 years	
Total length	1900 mm		1900 mm	
Arcing distance	1600 mm		1600 mm	
Creepage distance	5250 mm		5460 mm	
Specific creepage distance	35 mm/kV		36.4 mm/kV	
Number of sheds	23 (small)/ 24 (large)		40	
Shed diameter	100/135 mm		135 mm	
Shed thickness	4-8 mm		5-10 mm	

Fig. 1.10: The parameters of the evaluated composite insulators with sheds made of SIR and EPDM [38].
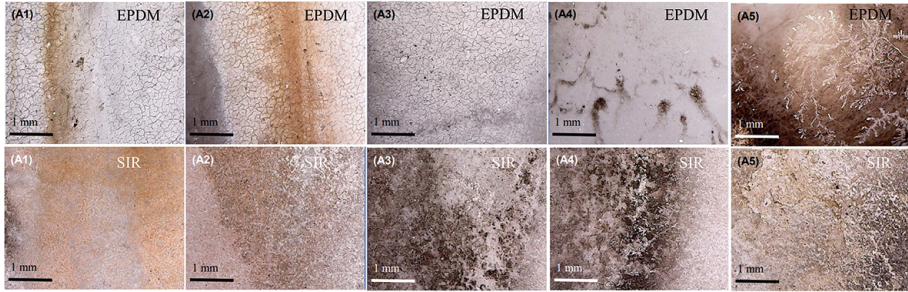
Fig. 1.11: The comparison of the surface morphology of SIR and EPDM as insulator shed after a long-term operation [38].

For the profile design of the sheds for the composite cross-arms, Tohid *et al.* compared the effect of two different shed profiles: uniform sheds, and alternating large and small sheds on the electric field distribution along and inside the cross-arm of the Y-shaped pylon [42]. The two kinds of shed patterns and arrangements are depicted in Fig. 1.12(a) and (c). The local electric field simulation was carried out at three regions of interest: on the shed surface, within the housing layer, and at 0.5 mm above the insulation surface, and there is no obvious difference in the distribution of field strength

with two different shed patterns (Fig. 1.12(b) and (d)). However, in wet and polluted environments, the shed profile has a prominent influence on the flashover voltage. As indicated in [43], 22 kinds of composite with different shed overhang (P) and shed spans (s) were examined under standard wet and artificial pollution conditions. It is reported that excessively adding the number of sheds and enlarging shed diameter in a fixed insulator length may lead to flashover overvoltage reduction. According to IEC 60815-3 [44], the shed pattern is characterized by the ratio of the shed overhang to spacing (P/s), under-side/upper-side inclination angle (α/β). It is recommended that $s \geq 65$ mm, $P/s \leq 1.25$, $\alpha > 3°$ and $\beta > 10°$ [45]. Meanwhile, the alternating sheds are recommended from perspectives of avoiding shed arcing, pollution deposition, and dry band formation [44].
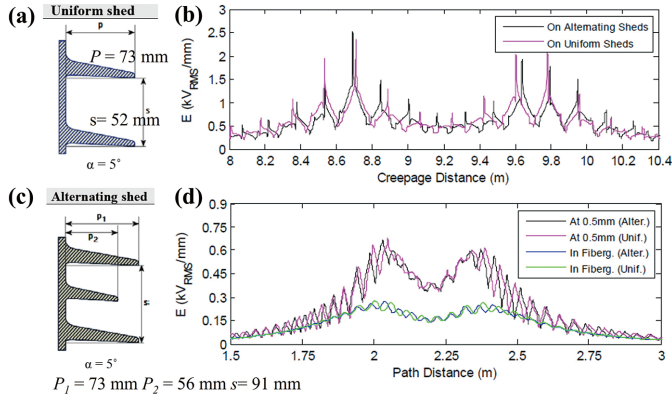
Fig. 1.12: (a) Typical uniform sheds. (b) The electric field strength along the surface of sheds. (c) Typical alternating small and large sheds. (d) The electric field magnitudes within the housing layer and at 0.5 mm above the insulation surface [42].

1.2.3 Lightning Performance of Composite Pylon

A. Lightning Shielding Performance

Lightning is one of the most important factors influencing the safe operation of transmission lines [46]. Thus, limiting overvoltage caused by a lightning stroke and avoiding outages have essential significance for the safe operation of transmission towers. For high voltage long-distance transmission lines, shield wires are normally employed and located over the phase conductors to intercept the direct lightning strokes and protect the phase conductors [47]. The geometry of the shield wires directly relates to the shielding performance. Compared with the conventional towers, the height of the composite tower conductors is lower, and the phase-to-earth clearance is closer (Fig. 1.13). The shield angle (α), the angle between a vertical line extending downward from the shield wire and the line of shield wire to phase wire, is another indicator
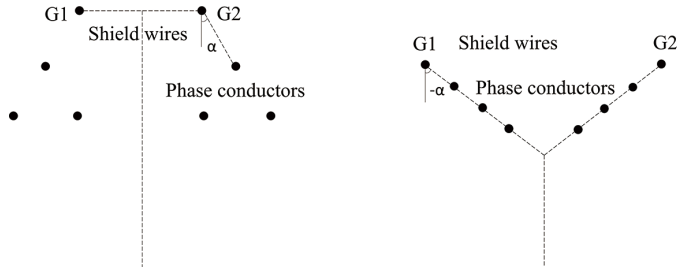
Fig. 1.13: The geometry configuration of shield wires and phase conductors. The left figure is the traditional steel tower, and the right one is the Y-shaped composite pylon. G_1 and G_2 refer to shield wires.

of lightning shielding performance. For effective shielding, the shielding angle should be kept as small as possible in general rules [48]. Normally, the shield angle of the composite tower is less than that of the conventional steel tower.

The composite tower has a lower probability of being struck by lightning due to its lower height and narrower width. Thus, for medium voltage transmission lines, the omission of shield wires with the installation of surge arresters is another possible alternative. The Compact Plus Tower was created to lessen the electromagnetic fields produced by the transmission lines and improve the visual impact [49]. As can be seen in Fig. 1.14, the absence of shield wires and the narrow phase spacing are remarkable features. Furthermore, the insulators are positioned as cross-arms on the top of the poles, and surge arresters link with the top phase that serves as a shield wire for the other two phase conductors [49]. However, this method is unsuitable for 220 kV or above transmission lines.

Fig. 1.14: The Compact Plus Tower [49].

The lightning shielding performance of the Y-shaped pylon has already been studied in a previous Ph.D. project [10]. The revised electro-geometric method is used to estimate the shielding failure rate (SFR), which is no more than 0.0008 flashes/100

km-year, far lower than the acceptable value range from 0.1 to 20 flashes/100 km-year for transmission towers. The previous research also shows that the shielding failure flashover rate of this 'Y' composite pylon is almost zero. The relevant lightning tests on a down-scaled pylon model agree with the theoretical results, verifying that the Y-shaped pylon has good shielding performance.

B. Ground Mode of Composite Pylon

The shield wires should be grounded by down-leads to reduce the overvoltage induced by lightning terminating on the shield wires. The function of a down-lead is to provide the path for lightning conducting and shunt the current to the ground, reducing the lightning trip-out rate and enhancing the reliability of the power supply. Taking into account the performance characteristics of composite material and ground down-lead, the technical feasibility, configuration reliability, and assembly convenience, there are primarily two grounding methods:

- (1) Grounding down-lead vertically along the external tower body at a certain distance away from the tower body.

- (2) Grounding down-lead vertically through the pylon body.

The external ground mode (1) is often employed for a single pole tower such as in Fig. 1.5. China Electric Power Research Institute proposed two ways of external grounding in Fig. 1.15. For lattice composite towers or double-pole towers (Fig. 1.5), ground mode (2) is a common way for the down-lead (Fig. 1.16). The down-lead passing through the center of the composite tower can be fixed by crossed metal bracings, at the same time, the surge impedance of the down-lead can be reduced by the bracings. To date, there is no research regarding the ground mode (2) used for single-pole composite towers. Therefore, the grounding mode passing through the pylon body is highly worth to be studied.
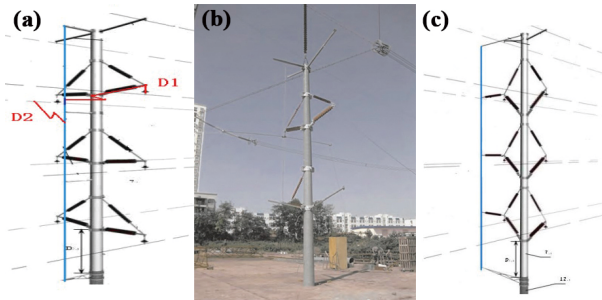
Fig. 1.15: (a) The vertical down-lead is paralleled with the mast in the middle of the double-circuit lines and (b) the field test for this ground mode. (c) The down-lead is suspended on the side of the lines [18].
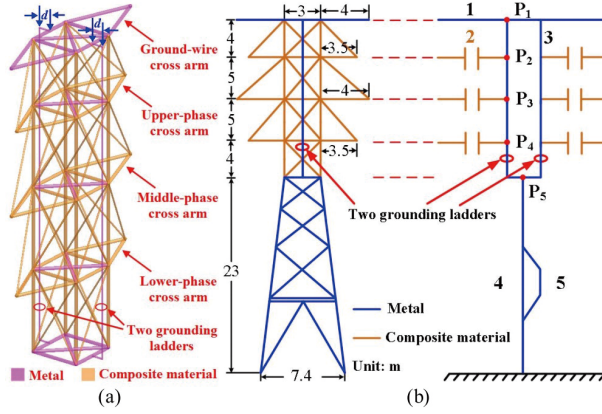
Fig. 1.16: (a) Composite lattice tower head. (b) Down-lead ground mode of the composite tower and the equivalent circuit of the tower [50].

C. Backflashover Rate of Composite Pylon

The lightning performance of OHLs is represented by how many lightning flashovers per year per 100 kV length of distribution lines, which is called the backflashover rate (BFR). In general, the backflashover is caused by direct lightning strikes and electromagnetic pulses due to lightning hitting the ground in the proximity of OHLs. For direct lightning striking caused backflashover, the first computational process is to establish the electromagnetic transient (EMT) model for the down-lead system. Then, the lightning-induced overvoltage stressed on the insulator is simulated and the critical current (I_c) can be obtained based on the insulator flashover criterion. Finally, the BFR is calculated based on I_c [51]. The detailed modeling process of tower components will be presented in Chapter 2.

A lightning performance test was conducted for the full-scale 110 kV composite pole in Fig. 1.15 with the externally grounded down-lead. As the ground impedance is 7 Ω, the composite cross-arm can withstand 1230 kV standard IEEE lightning voltage, and the lightning trip-out rate is 0.28 times/100km/year [18]. Y. Huangfu *et al.* studied the lightning performance for a 330 kV composite transmission tower with counterpoise ground electrodes [50]. The effect of the different lightning current front time (T_f), down-lead radius, number and position, and soil resistivity has been investigated by finite-difference time-domain simulation (FDTD) [52] and the electromagnetic transient program (EMTP) [53]. They found the tower with double ground down-leads has the lowest overvoltage compared with single or triple down-leads when the tower is struck by lightning, and the corresponding I_c is above 140 kA for lightning current with T_f of 2.6 μs. In addition, the radius of the down-lead conductor makes little difference in the lightning performance of the composite tower.

The flashover induced by indirect strikes is usually related to the transmission line configuration and height of OHLs. In general, the standard Monte Carlo procedure

and electromagnetic field calculation are combined to evaluate an annual number of flashovers. The procedure for the calculation of BFR consists of three stages [54]:

- In stage 1, A large number of lightning events characterized by lightning current amplitude (I_a), front time (T_f), and the distance between the transmission line and strike location are generated randomly using the Monte Carlo approach. Wherein, the generated values of the lightning current parameters follow the statistical distribution of lightning flashes. The stroke locations are assumed evenly distributed in the vicinity of transmission lines with enough distance to include all the strikes that may induce a flashover.

- Stage 2 is the modeling of induced overvoltage calculation. Firstly, the spatial electromagnetic field with a vertical lightning channel is calculated. Then, the field-to-transmission line coupling model is adopted to get the induced overvoltage [55, 56]. Simplified formulas can be performed to get the voltage values [57, 58], but for higher accurate appraisal, time-domain EMTP codes or electromagnetic transient simulation are commonly used [59, 60].

- Stage 3 is BFR calculation. The annual numbers of backflash events are estimated by the following equation (1.1).

$$F_p = \frac{n_f}{n_{\text{tot}}} S_a N_g \tag{1.1}$$

Where n_f is the number of flashover events, and n_{tot} is the total randomly generated lightning events. S_a is the lightning stroke area, and N_g is the annual ground lightning density (flash/km^2/year).

The Ph.D. project mainly focuses on the transient overvoltage and BFR caused by direct lightning on the shield wires. The backflash due to indirect stroke is not covered in this thesis, and the lightning performance mentioned in the following content only refers to tower backflash performance.

1.3 Project Motivations

Power Pylons of the Future (PoPyFu) project launched in 2013 proposed an advanced concept of a 'Y' tower as shown in Fig. 1.17, aiming to meet the requirement for constructing new environmental-friendly overhead lines. The innovative 'Y' tower has a variety of advantages as the new generation transmission tower aforementioned in the Background. However, the BFR of the composite pylon is seriously lacking systematic research. Originally, a proper grounding method has not been determined to bring ground potential to the shield wires. In reference [61], a bare conductor going through a hollow cross-arm proposed as the ground method has been studied, and the electrostatic field indicated that the local electric field (E-field) magnitudes around the

bare down-lead are higher than the corona inception threshold, and the filling material for cross-arm is needed to avoid inner partial discharge. Based on the initial study of the fully composite pylon, two possible methods are considered as shown in Fig. 1.17:

- **Method 1** - A grounding conductor/cable passing through the hollow/filled FRP tube and the pylon body;

- **Method 2** - A grounding lead (either a cable or a bare conductor) going down outside the cross-arm and the pylon body.
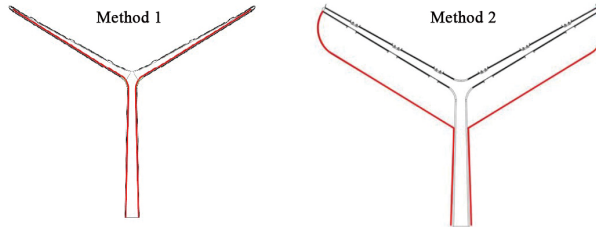
Fig. 1.17: Two possible grounding methods for the composite pylon.

The pylon with method 1 as the down-lead routing way has narrower transmission width, and no additional components are required to fasten the down-leads. Meanwhile, the internal ground method has less visual impact and an aesthetical appearance. Therefore, the down-lead going through the FRP cross-arm tube is the preferred option in the present Ph.D. project. At this time, the down-lead system of this pylon is different from the traditional steel tower. It is necessary to propose new methods or models to study the lightning protection performance of this tower, and the feasibility of this down-lead system must be verified before generalization.

1.3.1 Research Questions

- Adoption with the ground method 1, whether the lightning protection behavior of the Y-shaped pylon can meet the requirements for safe operation?

- Whether the optimization of the whole or partial down-lead system can be carried out to improve the lightning protection performance of the 'Y' tower?

- Whether the cable passing through the hollow cross-arm is a feasible ground method to improve lightning protection behaviors?

- In high voltage engineering, empirical expressions play important roles in the fast estimation of lightning protection performance. Whether empirical formulas commonly used for the assessment of the lightning performance of transmission towers are suitable for the newly designed pylon?

1.3.2 Research Objectives

With the above research questions, the objectives of this Ph.D. project are summarized as follows:

- **Establish an electromagnetic transient model with high accuracy for the Y-shaped pylon**
  The multi-stage segmentation is adopted for down-lead modeling. Resorting to Finite Element Method (FEM) software, the self and mutual capacitance and inductance between two separated down-leads are obtained, and the parasitic capacitance of the down-lead is determined. Then, the equivalent circuit of the down-lead system can be built in PSCAD/EMTDC to obtain the transient overvoltage with lightning striking.

- **Optimization of down-lead system**
  Changing the dielectric properties of the cross-arm filling materials, the radius of the cross-arm, and the structure of the down-lead are considered to improve the lightning performance of the Y-shaped pylon. Based on the results, the filling materials are determined and the grounding lead system of the pylon is optimized.

- **A down-scale model test to verify the feasibility of the down-lead scheme**
  A down-scale cross-arm model made by FRP is built to investigate the internal cross-arm insulation strength. Combined with the partial discharge test, lightning impulse test, and FEM simulation, the feasibility of the down-lead system is validated in different scenarios including switching overvoltage and lightning striking.

- **Propose empirical formulas based on lattice diagram method**
  Based on the traditional lattice diagram method, the lightning critical current of the Y-shaped pylon is formulated. Then, the equivalent surge impedance of the down-lead is simplified and the empirical formulas are derived from the surge traveling process along the down-lead system. The Monte Carlo procedure is used to verify the formulas' accuracy.

1.3.3 Project Limitations

There are still several limitations in this Ph.D. project, as listed in the following:

- Since the steel lattice towers including Eagle and Donau towers are studied for comparison with the 'Y' composite tower, the same metal rods are employed as the ground electrodes for all towers to facilitate the comparison. For Y-shaped and Eagle pylons, coupling rods in series are easily threaded at the tower ends owing to their tower bodies being masts. However, for the Donau tower with a lattice structure, four-legged counterpoises with about 15 meters or a square

grid base should be applied as the ground systems [51, 62]. Therefore, in actual engineering, different ground structures should be considered for these towers.

• In the process of investigating lightning performance in this Ph.D. project, the I_c is simulated with different T_f regardless of their relationship. However, the directly measured current by Tokyo Electric Power Company showed that there is a correlation among the T_f, maximum rise rate, and current amplitude [63, 64]. For model simplification, only relationship between lightning front time and rise rate is taken into consideration.

• The BFR is deduced from the equation (1.2) (description in Chapter 2). Wherein C_p is a coefficient that is directly related to the pylon span and transmission line height. In this Ph.D. research, the effects of the pylon span and position of the transmission line on the BFR have not been studied, and C_p takes a constant value of 0.6 recommended by reference [51]. In addition, the backflashover caused by strikes to the ground is not involved.

$$BFR = C_p N_L \left(1 - P_c(I_c)\right) \tag{1.2}$$

1.4 Thesis Outline

The dissertation is organized into 6 chapters to present the research work on the down-lead system design for the Y-shaped pylon and the corresponding lightning performance investigation. A brief description of each chapter is given here below:

• **Chapter 1 - Introduction**
In chapter 1, the background of the Ph.D. project is presented. Then the state-of-the-art regarding development, application, and challenge of the composite transmission pylon are introduced. Finally, the motivation, research questions, and project objectives are clarified.

• **Chapter 2 - Lightning Performance of 'Y' pylon**
Chapter 2 presents a detailed representation of the electromagnetic transient model for the down-lead system of the Y-shaped pylon including the surge impedance calculation, modeling of the tower components, and ground impedance. Based on that, the critical current and backflashover rate of the 'Y' pylon are given. For comparison purposes, the lightning performance of Eagle and Donau transmission towers applied for the same voltage level is investigated.

• **Chapter 3 - Optimization of Down-Lead System for 'Y' Pylon**
In this chapter, the pylon components, configuration, and parameters are optimized to increase the insulation strength and pylon critical current. The insulation reliability after optimization has been verified.

- **Chapter 4 - Feasibility of Cable As Down-lead**
  Chapter 4 proposes a scheme that uses a cable through the cross-arm tube as a down-lead to ground the shield wires. Through experiments on a cross-arm scale model, the parameters of the cable are determined. Then, the insulation level of the cross-arm at switching surge and lightning striking conditions has been investigated.

- **Chapter 5 - Formula Expression of Lightning Performance**
  Chapter 5 gives a brief review of the existing empirical formulas used for lightning performance estimation. Then novel equations based on the lattice diagram method are proposed for the Y-shaped pylon, which exhibits an obvious superiority in terms of lightning performance prediction accuracy.

- **Chapter 6 - Conclusion**
  In this chapter, concluding remarks and the main contributions of this Ph.D. thesis are summarized, and the future research perspectives in the design of composite pylon are outlined.

1.5 List of Publications

The research outcomes from the Ph.D. project have been disseminated in the form of publications, which include 6 journal papers and 3 conference papers. Table 1.1 describes the corresponding relationship between papers and individual thesis chapters.

Journal Papers

J1. **K. Yin**, M. Ghomi, H. Zhang, F. F. da Silva, C. L. Bak, Q. Wang, H. Skouboe, "The design and optimization of the down-lead system for a novel 400 kV composite pylon," *IEEE Transactions on Power Delivery*, Accepted. DOI: 10.1109/TPWRD.2022.3193562.

J2. **K. Yin**, M. Ghomi, H. Zhang, C. L. Bak, F. F. da Silva, Q. Wang, "Lightning transient response of bifurcation structure pylon and its empirical expression with high accuracy and general application," *International Journal of Electrical Power and Energy Systems*, Second review.

J3. **K. Yin**, G. Zhu, Yi. Shi, H. Zhang, F. F. da Silva, C. L. Bak, X. Chen, "Feasibility of cable through a hollow cross-arm as down-lead for a 400 kV Y-shaped composite pylon," *Electric Power Systems Research*, Under review.

J4. M. Ghomi, H. Zhang, C.L. Bak, F.F. da Silva, **K. Yin**, "Integrated model of transmission tower surge impedance and multilayer grounding system based on full-wave approach," *Electric Power Systems Research*, vol. 198, pp. 107355, Sep. 2021.

J5. H. Zhang, Q. Wang, F.F. da Silva, C.L. Bak, **K. Yin**, H. Skouboe, "Backflashover Performance Evaluation of the Partially Grounded Scheme of Overhead Lines with fully Composite Pylons," *IEEE Transactions on Power Delivery*, vol. 37, no. 2, pp. 823-832, Apr. 2022.

J6. H. Zhang, M. Ghomi, Q. Wang, F.F. da Silva, C.L. Bak, **K. Yin**, H. Skouboe, "Comparison of backflashover performance between a novel composite pylon and metallic towers," *Electric Power Systems Research*, vol. 196, pp. 107263, Jul. 2021.

Conference Papers

C1. **K. Yin**, F.F. Da Silva, C.L. Bak, H. Zhang, Q. Wang, H. Skouboe, "Electric Field Computation and Optimization for A 400 kV Y-shaped Composite Cross-arm," in *2021 International Conference on Electrical Materials and Power Equipment (ICEMPE)*, pp. 1-4, Apr. 2021.

C2. **K. Yin**, M. Ghomi, F.F. Da Silva, C.L. Bak, H. Zhang, Q. Wang, "The effect of frequency-dependent soil electrical parameters on the lightning response of a 'Y' shaped composite pylon for 400 kV transmission lines," in *22nd International Symposium on High Voltage Engineering (ISH 2021)*, pp. 2046 – 2051, Nov. 2021.

C3. **K. Yin**, M. Ghomi, F.F. Da Silva, C.L. Bak, H. Zhang, Q. Wang, H. Skouboe, "Lightning performance and formula description of a Y-shaped composite pylon considering the effect of tower-footing impedance," in *2021 35th International Conference on Lightning Protection (ICLP) and XVI International Symposium on Lightning Protection (SIPDA)*, pp. 1-6, 2021.

The publications finished during the Ph.D. period but not included in the Ph.D. thesis are listed below:

- **K. Yin**, Q. Xie, H. Ruan, Q. Duan, F. Lü, X. Bian, T. Zhang, "Causation of ultra-high surface insulation of $Bi_{0.95}Y_{0.05}FeO_3$/epoxy composites: Simultaneous sine-variations of dielectric and trap properties with filler content," *Composites Science and Technology*, vol. 197, no. 8, pp. 108199, Sep. 2020.

- **K. Yin**, J. Yan, H. Zhang, Q. Duan, Q. Wang, C. Zheng, Z. Zhang, Q. Xie, "The effect of gradient conductivity of doped $BiFeO_3$ as filler on the surface insulation performance of epoxy composite," *Journal of Physics D: Applied Physics*, vol. 53, no. 39, pp. 395502, Jul. 2020.

- **K. Yin**, "Progress in Vacuum Flashover Mechanism: Validity of ETPR Theory," in *2020 29th International Symposium on Discharges and Electrical Insulation in Vacuum (ISDEIV)*, pp. 93-104, Sep. 2021.

Table 1.1: Relationship between published papers and thesis chapters

Chapter	Associated Publications
Chapter 1	
Chapter 2	J1, C2, J4, J5, J6
Chapter 3	J1, C1, J3
Chapter 4	J3, C1
Chapter 5	J2, C3
Chapter 6	

Chapter 2

Lightning performance of 'Y' pylon

In this chapter, the structure of the Y-shaped pylon is described, and the modeling of the pylon equivalent circuit is discussed. Aimed at the Y-shaped pylon, the formulas for the surge impedance of the down-lead inside the cross-arm are proposed. Meanwhile, both the mutual coupling between two down-leads and parasitic capacitances are considered. Finally, the critical current and backflash rate of the 'Y' composite pylon are attained and a comparative study is conducted between the composite pylon and conventional pylon on lightning performance.

2.1   Configuration of 'Y' Composite Pylon

The initial design of a double circuit 400 kV fully composite pylon is illustrated in Fig. 2.1. The height of this kind of tower is 22.5 meters. The vertical mast height and radius are 16.5 m and 0.5 m, separately. The integration of insulators in a form of a unibody cross-arm has a cone shape to carry the three phase conductors. The cross-arm forms a 30° to the horizontal line, and the overall length of a cross-arm is 12 m. Aluminum Conductor Steel Reinforced (ACSR) conductors with radii of 0.0175 m are chosen as phase conductors in the form of duplex bundles, which are mounted at the uni-body cross-arms. Each pair of duplex bundle conductors is linked by a flat conductor fitting. The semi-conductor carbon composites are used as a transition layer in the interface of conductors and fittings. The diameter of the conductor wrapped with a semi-conductor layer (d_c) is 0.04 m, and the conductor span S_c is 0.3 m. The bundle conductors are fixed by non-conductive (alumina ceramic) clamps with a height of 0.4 m and a width of 0.6 m. The clamp structure limits the E-field distortion around the phase conductors under the safe degree and keeps enough insulation distance ($h_{conductor}$=0.3 m) to avoid puncture in the extremely overvoltage case
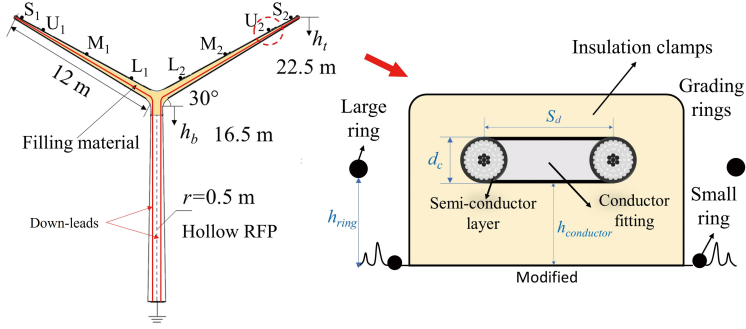
Fig. 2.1: Structure parameters of the composite 'Y' pylon and cross-section of the clamps. S represents the shield wire. U, M, and L represent the upper, middle, and lower phase conductors. Source: **J3** [67]

such as lightning overvoltage. According to IEC/TS 60815-3 [44], the phase-to-phase clearance and the phase-to-earth clearance are determined to be 3.6 m and 2.8 m, respectively [65]. Two copper wires with radii of 0.0175 m as down-leads are arranged inside the pylon's body and unibody cross-arm. There is no connection between the two down-leads. The pylon mast is a hollow FRP cylinder, while the cross-arm is filled with composite materials between the housing and down-lead.

According to the previous HV test carried out on the full-scale composite cross-arm, the E-field on the cross-arm surface exceeds the critical corona discharge magnitude in wet conditions, and the application of corona rings should be considered [10]. The electrostatic field optimization aimed at above 330 kV composite cross-arm also presents that the cross-arm equipped with appropriate grading rings can keep the E-field distribution within the safe operation range [66]. Therefore, each side of the phase conductors is mounted with double grading rings to relieve the E-field distortion. The large rings are 0.25 m (h_{ring}) above the surface of the cross-arm with radii of 0.02 m and the small rings are embedded in the FRP with a radius of 0.016 m.

2.2 EMT Model for Y-shaped Pylon

The lightning performance of the transmission tower needs to be appropriately assessed to grant adequate protection. In this Ph.D. research, the EMT model of the Y-shaped pylon is modeled in PSCAD/EMTDC [68]. The modeling of each component of the down-lead system is described in this section.

2.2.1 Representation of Lightning Stroke

A. Lightning Equivalent Model

In the lightning transient study, the lightning stroke is always represented by a

Norton equivalent current source, which consists of an ideal current source in parallel with an equivalent impedance [63]. According to a recent study, the lightning channel impedance is recommended to be 1000 Ω [69].

B. Lightning Current Waveform

The lightning current waveform is the basis of the analysis of the BFR. There are varieties of lightning current models with different waveshapes and parameters. At present, the commonly used lightning current models mainly include IEEE double exponential model [70], CIGRE concave model [63], triangular wave model [71], and Heidler model [72].

(1) IEEE bi-exponential model

This lightning current waveform is composed of double exponential waveforms and its equation expression $i(t)$ is given as (2.1)

$$i(t) = I_0 \left(e^{-\alpha_1 t} - e^{-\beta_1 t} \right) \tag{2.1}$$

Where I_0 is the lightning amplitude, α_1 and β_1 are the time constant.

(2) CIGRE Concave model

According to the CIGRE Brochure C4.23 [63], the current front can be expressed by

$$i = At + Bt^N \tag{2.2}$$

The suitable expression for the tail waveform is (2.3)

$$i = I_1 e^{-\left[\frac{t-t_n}{t_1} \right]} - I_2 e^{-\left[\frac{t-t_n}{t_2} \right]} \tag{2.3}$$

Where A, B, N, t_n, I_1, and I_2 are the functions related to the steepness (S_m). Meanwhile, the lightning steepness is also given, and the correlation between the lightning steepness and its current magnitude I_0 follows (2.4) [51]

$$S_m = 4.83 I_0^{0.47} \tag{2.4}$$

(3) Triangular model

The triangular lightning waveform has a linearly rising wavefront and tail waveform, and the front and tail formulas are expressed below. Where T_f and T_t are the front time and tail time, respectively.

$$i = \frac{I_0}{T_f}, t < T_f$$
$$i = \frac{I_0}{2(T_t - T_f)} (t - T_f) + I_0, t \geq T_f \tag{2.5}$$

(4) Heidler model

Heidler model defines functions as

$$I = (I_0/\eta) \left((t/\tau_1)^2 / 1 + (t/\tau_1)^2 \right) e^{-t/\tau_2} \tag{2.6}$$

Where η is expressed as:

$$\eta = e^{-(\tau_1/\tau_2)(2\tau_1/\tau_2)^{-2}} \tag{2.7}$$

This model considers the first and subsequent return strokes, and the return stroke is represented as the sum of two Heidler functions. The parameters are given for reproducing the lightning strokes and the equivalent amplitude and front time are shown in Table 2.1.

Table 2.1: Heidler lightning waveform

Lightning waveform	I_0 (kA)	τ_1 (μs)	τ_2 (μs)	Equivalent I_0 (kA)	Equivalent T_f (μs)
First stroke	28	1.8	95	26	4
Return stroke	10.7/6.5	0.25/2	2.5/230	10.7	0.62

The observed lightning waveform and IEEE, CIGRE, Triangular, and Heidler models are plotted in Fig. 2.2. It can be seen that the realistic representation of the stroke current amplitude has a slow rise rate in the initial state and a gradually increased S_m. CIGRE lightning waveform conforms to these characteristics, and it is used to simulate I_c in this research. Heidler waveforms are recommended as the first and return lightning models for the simulation.

C. Probability Distribution of Lightning Parameters

The statistical distribution of the lightning parameters based on a large number of tested data from Berger [73] and Anderson [74] can be approximated by a log-normal distribution. The probability density function of I_0, T_f, and T_t can be approximately expressed by

$$f(x) = \frac{1}{\sqrt{2\pi}\zeta x} e^{-\frac{1}{2}\left(\frac{\ln(x/M)}{\zeta}\right)^2} \tag{2.8}$$

The mean value μ of the lightning parameter can be determined by the two coefficients M and ζ. They are recommended to be 31.1 kA and 0.484 for I_0, 3.83 μs and 0.553 for T_f, and 77.5 μs and 0.577 for T_t, respectively [51].

$$\mu = Me^{\frac{\zeta^2}{2}} \tag{2.9}$$

2.2.2 Determination of Surge Impedance

In general, the distributed parameter circuit is suitable for analysis of the lightning response. Determining the surge impedance of metal parts is the first step in EMT model building [75]. The down-lead system mainly consists of two parts: the vertical

down-lead inside the tower body and the inclined down-lead inside the cross-arm.
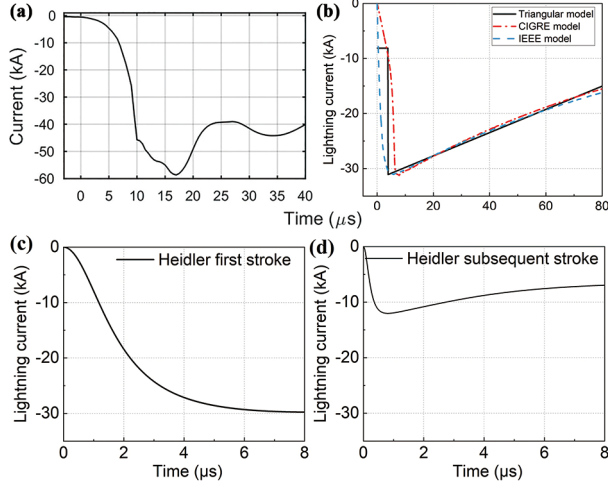
Fig. 2.2: (a) Typical lightning waveform observed in nature [71]. (b) The IEEE, CIGRE, and Triangular 3.83/77.5 μs waveform with I_0=31.1 kA. Heidler (c) first and (d) return stroke waveforms.

A. Surge Impedance of Vertical Segment of Down-Lead

For the calculation of vertical surge impedance of down lead inside the pylon body, there are several formulas for this parameter similar in different forms [76–78]. According to Michael A.'s work [76], the responses of a cylindrical metal pole to a lightning current with ramp waveform is given by (2.10). Because the response to a lightning impulse wave shape approximates the response to a ramp wave, the surge impedance of a cylindrical pole for an impulse of current can be used to represent the vertical down-lead impedance.

$$Z=60\left[\ln\left(\sqrt{2}\frac{ct}{r}\right)-1+\frac{r}{2ct}+\left(\frac{r}{2ct}\right)^2\right] \tag{2.10}$$

Where r is the single down-lead conductor radius. c is the light speed. The maximum tower top potential will occur at time $t = 2h/c$, and h is the height of the down-lead. For $ct \gg r$, $h \gg r$, it is generally suggested for a cylinder.

$$Z=60\left[\ln\left(\sqrt{2}\frac{2h}{r}\right)-1\right] \tag{2.11}$$

B. Surge Impedance of Inclined Down-Lead

The down-lead inside the cross-arm of the pylon is inclined and wrapped with the FRP materials, whose surge impedance cannot be calculated by the traditional formulas used for the lattice towers. It is necessary to propose formulas to characterize the

surge impedance of the oblique down-lead. The surge impedance response of a conductor to high-frequency lightning impulse can be represented by the square of the ratio of capacitance to inductance [51]. Thus, the distributed parameter circuit is employed to build the equivalent circuit and obtain the transient overvoltage when lightning current passes through the cross-arm. Referring to the multistory method of the tower modeling [78, 79], each down-lead inside the cross-arm is thought to be divided into four parts as shown in Fig. 2.3(b). Each section is composed of self-inductance and self-capacitance. Here, the mirror image method is employed as the approach to deduce the inductance and capacitance of the segmented cross-arm [2]. The lateral cross-section interface and external structure of the cross-arm are depicted in Fig. 2.3. Assuming x is the horizontal extension from the tower center, namely, $x = l\cos 30°$. The radius of cross-arm b as a function of x is $b_b - (b_b - b_t)x/6\sqrt{3} = 0.45 - 0.325x/6\sqrt{3}$.
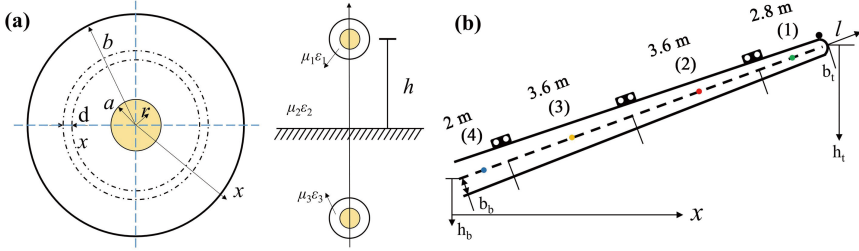
Fig. 2.3: (a) The cross-section of the cross-arm and the mirror image of overhead down-lead inside the cross-arm. (b) The schematic of a real composite cross-arm. Source: **J2** [80].

(1) Inductance of down-lead inside the cross-arm [80].

In linear media, the self-induction flux linkage of the coil Ψ is proportional to the excitation current I. This ratio is the self-inductance L, which is primarily composed of the external inductance L_e [81]. The inner flux linkage of the cross-arm core can be neglected due to the skin effect.

$$L = \frac{\Psi_e}{I} = L_e \tag{2.12}$$

The magnetic field strength of one point is the superposition of the H_e produced by the cross-arm and its image, and the number of turns is 1. The external flux linkage of the cross-arm core Ψ_e:

$$\Psi_e = \int d\Psi_e = \int d\Phi \tag{2.13}$$

$$\Psi_e = \frac{Il}{2\pi} \int_a^b \left(\frac{\mu_1}{x} + \frac{\mu_1}{2h - x}\right) dx + \frac{Il}{2\pi} \int_b^{2h-b} \left(\frac{\mu_2}{x} + \frac{\mu_2}{2h - x}\right) dx$$
$$+ \frac{Il}{2\pi} \int_{2h-b}^{2h} \left(\frac{\mu_3}{x} + \frac{\mu_3}{2h - x}\right) dx \tag{2.14}$$

$$\Psi_e = \frac{Il}{2\pi} \left[\mu_1 \left(\ln\frac{b}{a} + \ln\frac{2h - a}{2h - b}\right) + 2\mu_2 \left(\ln\frac{2h - b}{b}\right) + \mu_3 \left(\ln\frac{b}{a} + \ln\frac{2h - a}{2h - b}\right) \right] \tag{2.15}$$

Due to $\mu_1 = \mu_3$, μ_2 is equal to the μ_0. Ψ_e is

$$\Psi_e = \frac{Il}{\pi}\left(\mu_1 \ln \frac{b}{a}\frac{2h-a}{2h-b} + \mu_0 \ln \frac{2h-b}{b}\right) \tag{2.16}$$

Where a is the radius of the down-lead. The inductance for a segment of down-lead is

$$L = \int_{l_1}^{l_2}\left(\frac{\Psi_i}{I} + \frac{\Psi_e}{2I}\right)dl$$

$$= \int_{l_1 \cos 30^\circ}^{l_2 \cos 30^\circ} \frac{1}{2\pi}\left(\mu_1 \ln \frac{b}{a/\cos 30^\circ}\frac{2h-a/\cos 30^\circ}{2h-b} + \mu_0 \ln \frac{2h-b}{b}\right)dx \tag{2.17}$$

(2) Capacitance of down-lead inside the cross-arm [80].

Then the capacitance to the ground of the cross-arm can be calculated. The conductor charge density of down lead inside the cross-arm is ρ. The electric field at a certain point between the image and the object is

$$E(x) = \frac{\rho}{2\pi\varepsilon}\left(\frac{1}{x} + \frac{1}{2h-1}\right)e_x \tag{2.18}$$

The voltage between the image and the object is

$$U = \frac{\rho}{2\pi}\int_a^b \frac{1}{\varepsilon_1}\left(\frac{1}{x} + \frac{1}{2h-x}\right)dx + \frac{\rho}{2\pi}\int_b^{2h-b} \frac{1}{\varepsilon_2}\left(\frac{1}{x} + \frac{1}{2h-x}\right)dx$$

$$+ \frac{\rho}{2\pi}\int_{2h-b}^{2h-a} \frac{1}{\varepsilon_3}\left(\frac{1}{x} + \frac{1}{2h-x}\right)dx \tag{2.19}$$

$$= \frac{\rho}{2\pi}\left[\frac{1}{\varepsilon_1}\left(\ln\frac{b}{a} + \ln\frac{2h-a}{2h-b}\right) + \frac{2}{\varepsilon_2}\left(\ln\frac{2h-b}{b}\right) + \frac{1}{\varepsilon_3}\left(\ln\frac{b}{a} + \ln\frac{2h-a}{2h-b}\right)\right]$$

Due to $\varepsilon_1 = \varepsilon_3 = \varepsilon_0 k$, and k is the relative dielectric constant. ε_2 is equal to the ε_0. U is

$$U = \frac{\rho}{\pi}\left(\frac{1}{\varepsilon_1}\ln\frac{b}{a}\frac{2h-a}{2h-b} + \frac{1}{\varepsilon_0}\ln\frac{2h-b}{b}\right) \tag{2.20}$$

The capacitance for a segment of down-lead is

$$C = \int \frac{2\rho}{U}dl = \int_{l_1 \cos 30^\circ}^{l_2 \cos 30^\circ} \frac{2\pi}{\frac{1}{\varepsilon_1}\ln\frac{b}{a}\frac{2h-a/\cos 30^\circ}{2h-b} + \frac{1}{\varepsilon_0}\ln\frac{2h-b}{b}}dx \tag{2.21}$$

Of particular concern is that the velocity of the propagation v inside the down-lead segments is also changed accordingly as shown in (2.22) [51]:

$$v = 1/\sqrt{LC} \tag{2.22}$$

C. Simulation Verification For Calculation Results

In order to validate the correctness of the theoretical calculation, a 3D full-scale cross-arm is built in COMSOL (Fig. 2.4) and the electrostatic simulation is used to estimate the self-capacitance value of each down-lead segment. 1 V voltage is given on the down-lead above a lossy ground, the capacitance can be obtained through Maxwell Capacitance Matrix. Assuming the filling material for the cross-arm is FRP and the k is 2.64 [10], the simulation and calculation results are obtained and compared in Table 2.2. The theoretical values are well matched with the simulation results, and the largest error is only 1.36%.
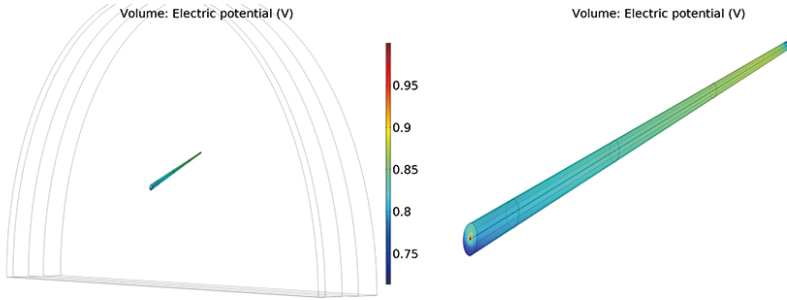
Fig. 2.4: The potential distribution of the cross-arm derived from simulating self-capacitance of down-lead segments.

The magnetic field simulation can provide the self-inductance of each segment. Treating the down-lead segment as coil, and defining the coil current 1A passing into one terminal. The self-inductance can be obtained in Global Evaluation. The difference between the simulation and calculation results is very limited as shown in Table 2.3.

Table 2.2: The simulation and calculation values of self-capacitance of each down-lead segment.

	Segment 1	Segment 2	Segment 3	Segment 4
Simulation results	21.002 pF	28.741 pF	29.619 pF	17.297 pF
Theoretical results	21.023 pF	28.349 pF	29.688 pF	17.054 pF
Error (%)	0.001	1.36	0.03	1.17

Table 2.3: The simulation and calculation values of self-inductance of each down-lead segment.

	Segment 1	Segment 2	Segment 3	Segment 4
Simulation results	3.825 μH	4.741 μH	4.733 μH	2.642 μH
Theoretical results	3.723 μH	4.739 μH	4.680 μH	2.573 μH
Error (%)	2.67	0.042	1.12	2.61

D. Simplification of Inclined Down-lead

Although the integral form formulas evaluate the surge impedance of the down-lead with high accuracy, it is too complicated for calculation in general. Thus, a simplification of the down-lead segment is proposed to facilitate formula expression. As shown in Fig. 2.5, taking the geometric center of the inclined cross-arm as the rotation point, each down-lead segment rotates to a horizontal position. In addition, each rotated segment has a uniform radius which is equal to its mean radius. At this time, the inductance and capacitance of each simplified segment are expressed as follows:

$$L = \frac{\mu_0 l \cos \theta}{2\pi} \left(\ln \frac{2h - a}{a} \right) \tag{2.23}$$

$$C = 2\pi l \cos \theta / \left(\frac{1}{\varepsilon_1} \ln \frac{b}{a} \frac{2h - a}{2h - b} + \frac{1}{\varepsilon_0} \ln \frac{2h - b}{b} \right) \tag{2.24}$$
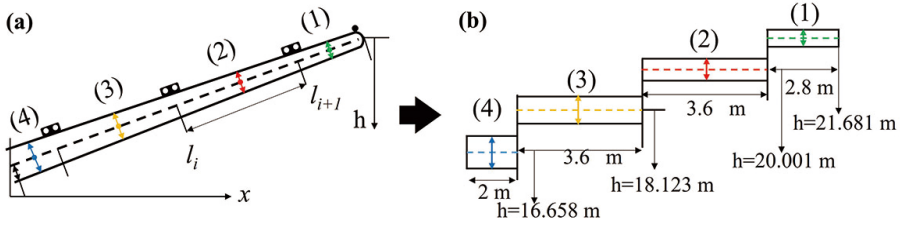
Fig. 2.5: (a) The schematic of a real composite cross-arm divided by four segments. (b) The schematic of the simplified cross-arm segments. Source: **C3** [82].

Compared with the results of integral formulas in Table 2.4, the errors of the simplified formulas applied for the four down-lead segments are no more than 1.05 %.

Table 2.4: Comparison of surge impedance results obtained by integral formulas and simplified formulas.

	Segment 1	Segment 2	Segment 3	Segment 4
Integral calculation results	420.80 Ω	408.84 Ω	397.05 Ω	388.42 Ω
Simplified formula results	425.22 Ω	411.67 Ω	398.94 Ω	389.82 Ω
Error (%)	1.05	0.69	0.48	0.37

COMSOL 2D RF-module can be employed to validate the simplified formulas for down-lead impedance. RF-module simulations in the research are based on the electromagnetic mirror method. The surge impedance is equal to the ratio of the conductor voltage to ground and internal current at the high-frequency domain. As the model does not involve computing the potential field, no additional assignment is required for the voltage and current sources. The voltage V is a line integral result of the electric field E from the down-lead to the ground, and the current I is calculated by a

close loop integral of the magnetic field along the closed semicircle O as shown in Fig. 2.6. Where the O bisects the solution area. The electric field distribution of the cross-section down-lead is exhibited in Fig. 2.7. The calculation values from proposed formulas and simulation values are listed in Table 2.5, and through the comparison, the largest difference is about 2.40%.

Table 2.5: Comparison of the surge impedance results obtained by simplified formulas and RF simulation. Source: **J1** [83].

	Segment 1	Segment 2	Segment 3	Segment 4
Simplified formula results	425.22 Ω	411.67 Ω	398.94 Ω	389.82 Ω
RF simulation results	434.03 Ω	421.54 Ω	408.34 Ω	396.34 Ω
Error (%)	2.07	2.40	2.36	1.67
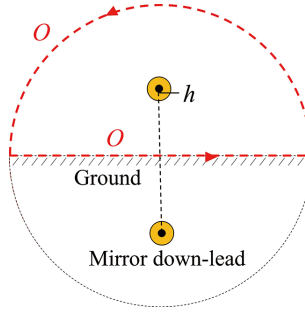
Fig. 2.6: The schematic of the integral path to compute the surge impedance of the down-lead segment. Source: **J1** [83].
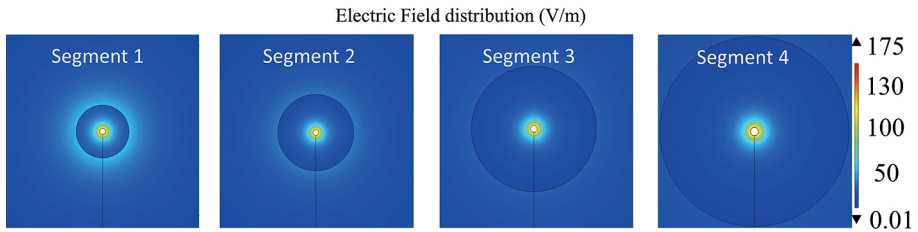
Fig. 2.7: The electric field distribution (V/m) of the cross-section of four down-lead segments. Source: **J1** [83].

2.2.3 Coupling Effect Between Down-leads

When a lightning current passes through one down-lead before reaching the pylon joint, the other down-lead will induce a voltage component due to their mutual electromagnetic interaction. The coupling effect between two down-leads can be established

by the external series capacitance and impedance matrices, which are determined by the down-lead geometric position and electric characteristics [2]. Based on the simplified down-lead model and assuming the down-leads hang over a perfect conductor ground, the image method is adopted to derive the series capacitance [84]. As illustrated in Fig. 2.8(a), the shunt capacitance matrix C_p between two down-lead segments i and j can be obtained as

$$C_p = \left\{ \frac{1}{2\pi\varepsilon} \begin{bmatrix} \ln \frac{2y_i}{a} & \ln \frac{D_{ij}}{d_{ij}} \\ \ln \frac{D_{ji}}{d_{ji}} & \ln \frac{2y_j}{a} \end{bmatrix} \right\}^{-1} \tag{2.25}$$

The derivation of the impedance matrix L_I should be considered the contribution of the earth return path [2]. Carson's ground model proposed a solution using a complex image method as shown in Fig. 2.8(b), and the corresponding impedance matrix between down-lead segments i and j can be written as

$$L_I = \frac{j\omega\mu_0}{2\pi} \begin{bmatrix} \ln \frac{2(y_i+p)}{a} & \ln \frac{D_{ij}'}{d_{ij}} \\ \ln \frac{D_{ji}'}{d_{ji}} & \ln \frac{2(y_j+p)}{a} \end{bmatrix} \tag{2.26}$$
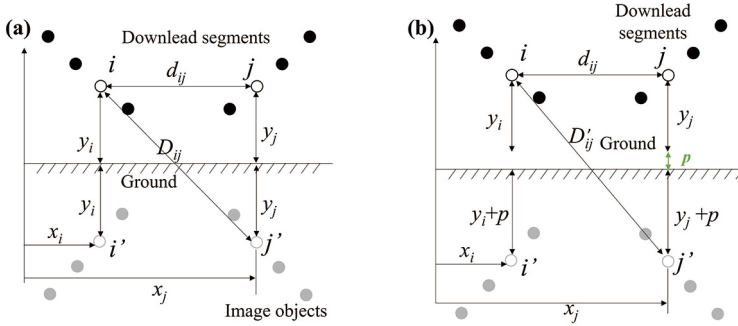
Fig. 2.8: Geometry of down-lead segments with the application of (a) image method and (b) complex image method. Source: **J2** [80].

The matrix elements are frequency (ω) dependent, and $y_i = y_j$. Where

$$D_{ij}' = \sqrt{4(y_i + p)^2 + (x_i - x_j)^2} \tag{2.27}$$

Meanwhile, the complex depth p is equal to

$$p = \sqrt{1/(j\omega\mu_e\sigma_e)} \tag{2.28}$$

Where σ_e and μ_e are the ground conductivity (S/m) and permeability (H/m), respectively [2]. In PSCAD, the mutual coupling function can be enabled in the module of down-lead segments at the conditions of the Frequency Dependent (Phase) Model and Carson ground impedance adopted [85].

2.2.4 Capacitance between down-lead and phase conductors

The substitution of uni-body composite cross-arms for the suspended insulators causes the spatial distance of the down-lead and phase conductors to be very close. Meanwhile, the coated dielectric with a higher permittivity results in a higher mutual parasitic capacitance between the down-lead and phase conductors compared with that of lattice towers. The FEM simulation is used to obtain the capacitances. One conductor is given a non-zero potential while other phase conductors and down-leads are grounded (Fig. 2.9). Then, the capacitance value can be acquired through the Maxwell Capacitance Matrix (Table 2.6).
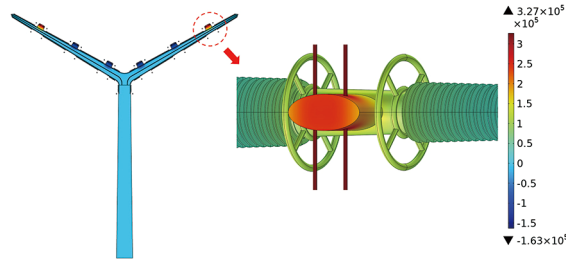
Fig. 2.9: The potential distribution plot generated when calculating parasitic capacitances with 327 kV applying.

Table 2.6: Parasitic capacitances of the down-lead.

	Upper phase to down-lead	Middle phase to down-lead	Lower phase to down-lead
Capacitance (pF)	46.17	51.41	50.43

2.2.5 Ground Model

In the design of the ground system, concentrated rods are mounted on the bottom of the pylon body. The length of the electrode is varied (3, 9, and 12 m, respectively) to investigate the effect of different ground conditions on tower overvoltage. When the current flows into the soil through the pylon electrode, potential gradients are set up and affect the reflection voltage during the surge traveling process. The grounding impedance performance normally depends on the current amplitude flowing through the rod and its frequency range. There are two commonly used ground models.

A. Current Dependence Model

Current-dependence ground model is used to represent the concentrated electrode such as the ro assuming that the soil is uniform. High magnitudes of lightning current

(I_R) flowing through the grounding system would cause soil ionization and decrease the footing resistance below the measured low-current values (R_0). The critical gradient E-field E_0 is approximated to 400 kV/m [51]. The critical current amplitude I_g is

$$I_g = \frac{\rho_0 E_0}{2\pi r_0{}^2} \tag{2.29}$$

Where ρ_0 is the soil resistance. The soil components in Denmark are mainly composed of clay and sand. Here, the ρ_0=100 Ω·m is suggested as the soil resistance for calculation [25]. The footing resistance R_i of the pylon is current dependence. It can be expressed as a function of I_R

$$R_i = \frac{R_0}{\sqrt{1 + (I_R/I_g)}} \tag{2.30}$$

The footing resistance of the electrodes under low-current conditions R_0 is related to the electrode length L_g and radius r_0 as (2.31) shown [86].

$$R_0 = (\rho_0/2\pi L_g) \left[\ln(4L_g/r_0)\text{-}1 \right] \tag{2.31}$$

B. Frequency Dependence Model

The current dependence ground model mentioned above reflects the impedance behavior in response to low-frequency current. However, the frequency spectrum of the standard lightning current ranges from 0 Hz to dozens of GHz. Therefore, the frequency-dependent effects of the grounding electrode subjected to lightning current should be contained in the ground model. The frequency-dependence modeling of the ground can be achieved by a full-wave electromagnetic field approach, and it shows a fairly good agreement with the actual data performed by experiments [62, 87]. To obtain the harmonic behaviors of the ground impedance as depicted in Fig. 2.10, each electrode is thought of as divided into small segments. The electromagnetic field equations between segments are represented by a matrix form [88]. The grounding impedance matrix is attained by the domain numerical solution of Maxwell's equations based on the method of moment. Then, it is formulated as state-space equations [62], which can be transferred from the frequency domain to the time domain and embedded in the FDNE module in PSCAD.

2.2.6 Flashover Criterion

A. Linear CFO

The standard lightning impulse crest voltage for which the insulation exhibits a 50 % probability of withstanding is called CFO. The CFO is associated with the length
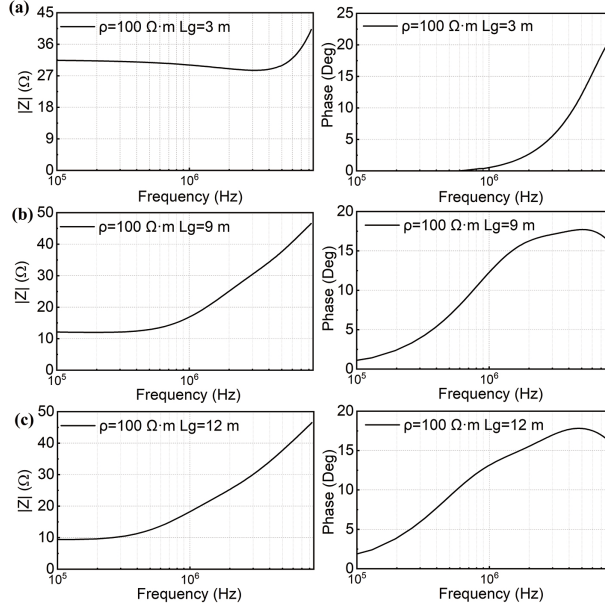
Fig. 2.10: The impedance of the vertical electrodes with different lengths. Source: **J2** [80].

of the insulation distance D, gap type, and lightning polarity. A simplified expression of CFO shows the linear relationship with insulation length, therefore, the CFO can be given by multiplying the CFO gradient and the insulation length. For air gap and insulators under 1.2/50 μs IEEE lightning impulse waveshape, the CFO gradient is suggested to be 605 kV/mm and 560 kV/mm for the negative and positive polarity [51].

$$CFO^- = 605D$$
$$CFO^+ = 560D \tag{2.32}$$

B. Volt-Time Curve

The impulse breakdown voltage across the insulator depends on the crest and the duration of the applied voltage, which can be depicted by the Volt-Time curve. A simple formula for the prediction of the 50% flashover voltage is given as [89, 90]

$$V(t) = \left(400 + \frac{710}{t^{0.75}}\right)D \tag{2.33}$$

Where t is the time in μs [90]. If the overvoltage waveform or the peak horizontal line on the insulator intersects with the Volt-Time Curve, it is considered to trigger a flashover. This method is mostly applicable to the IEEE lightning current [91].

C. LPM criterion

The Leader Progression Model (LPM) is a flashover criterion based on the physical process of discharge observed in experiments. When the stressed voltage reaches the threshold value, streamers emanate from electrodes. Once streamers cross the gap, ionizing waves propagate along the streamer channel and the leader starts to develop. As the applied voltage maintains an adequate electric field between the gap, the leaders collapse the gap in the form of arc [92]. The corresponding physical breakdown process is shown in Fig. 2.11.
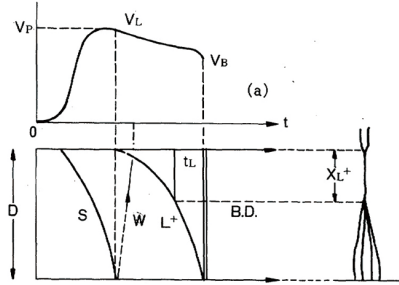
Fig. 2.11: The breakdown process of the positive rod-plane gap. V_p is the peak of lightning impulses. Where V_L is the instantaneous voltage at the start of the leader, V_B is the instantaneous breakdown voltage, s is the streamer, w is ionizing waves, L^+ is the leader, B.D. means the breakdown, D is the gap distance, X_L^+ is the leader length [92].

The CIGRE Brochure WG C4.23 gives the leader progression velocity of lightning impulse voltage with time as [63]:

$$\frac{dX_L}{dt} = Ku(t)\left(\frac{u(t)}{D - X_L} - E_l\right) \tag{2.34}$$

Where $u(t)$ is the applied voltage on the gap, E_l is the leader onset E-field and K is the coefficient of the leader progression velocity. E_l and K are determined by the gap configuration and the polarity of the impulse voltage, which are recommended in Table 2.7. The flashover characteristics between two grading rings can be regarded as an air gap discharge. Normally, 85 % - 95 % of lightning polarity is negative [51]. Thus, the K and E_l are set to 10^{-6} m^2/V^2/s and 670 kV/m [63], respectively.

Table 2.7: Parameter E and k recommended for different configuration and polarity.

Configuration	Polarity	k ($m^2\ v^{-2}\ S^{-1}$)	E (kV/m)
Air gaps, post insulator, and long rod insulator	Negtive	1×10^{-6}	670
	Positive	0.8×10^{-6}	600
Cap and pin insulators	Negtive	1.3×10^{-6}	600
	Positive	1.2×10^{-6}	520

When the leader develops to a certain length with the remaining gap distance less than h_f, the leader will immediately breakdown the gap. The threshold h_f is given by [93]

$$h_f = 3.89/\left(1 + 3.89/D\right) \qquad (2.35)$$

For the three aforementioned methods, the LPM model is based on the physical process and can be used for any lightning current waveform. Therefore, in the following chapters, the LPM algorithm is modeled in a custom module in PSCAD.

2.3 Lightning Performance Estimation For Towers

In this section, equivalent circuits of the transmission system are modeled in the PSCAD program to investigate the tower's lightning protection behaviors. For the modeling of the transmission line, a double-circuit transmission line with 7 pylons is the base of the simulation with a flash of lightning striking on the top of the middle pylon. The Frequency Dependent (Phase) Model is adopted to operate. Assuming 5% phase voltage fluctuation, the transmission line voltage is set to 420 kV, and the transmission capacity is 1000 MVA (Fig. 2.12). In order to improve the precision of the model, the LPM model is used to judge whether flashover happens, and the frequency dependence ground model is employed. The equivalent circuits of the down-lead systems are introduced in the following content.
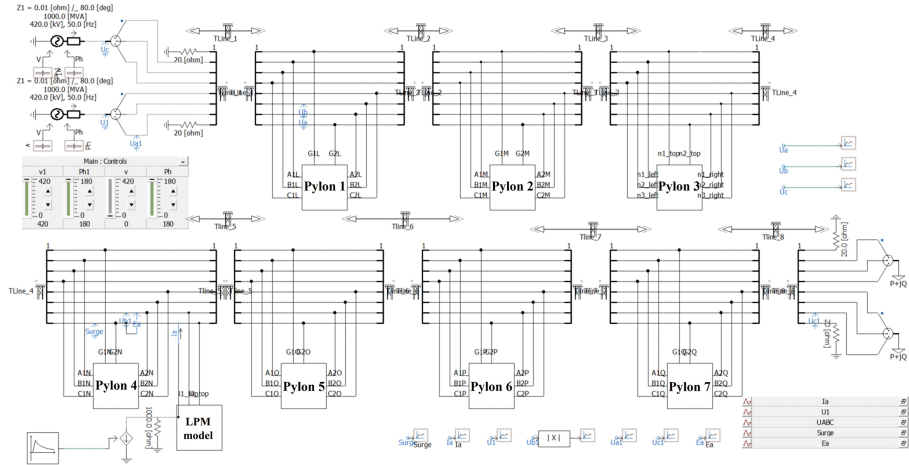

Fig. 2.12: The PSCAD modeling interface of transmission lines. Source: **J2** [80].

2.3.1 The Equivalent Circuit of Y-Shaped Pylon

For a Y-shaped pylon, two down-leads made of copper are connected with shield wires separately. Each down-lead is divided into five segments where four segments are inclined parts and one segment represents the vertical part. The mutual coupling effect is enabled in the TLine configuration. The schematic of the equivalent circuit for the Y-shaped pylon and the PSCAD modeling are shown in Fig. 2.13. The span between pylons is 250 m considering the mechanical load-bearing capacity.
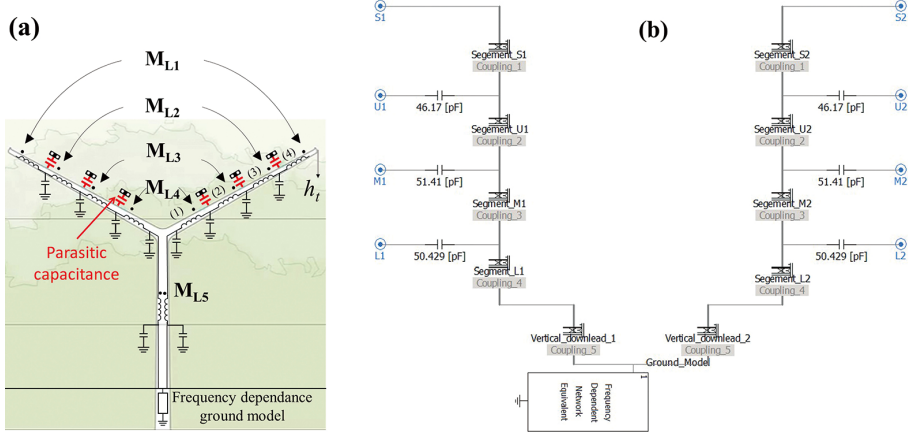
Fig. 2.13: (a) The schematic circuit of Y-shaped down-lead system. (b) The PSCAD modeling interface of the pylon.

2.3.2 The Equivalent Circuit of Steel Towers

The lightning performance of steel towers such as Donau and Eagle towers at the same voltage level is studied for comparison. Eagle and Donau towers' structures and ground electrodes are shown in Fig. 2.14. The length of the suspended insulator is 3.2 meters. The multi-story model is adopted for the modeling of steel towers. For horizontal parts including steel cross-arm and bracings, the surge impedance is given by [2]

$$Z_h = 60 \ln \left(2h / r_h \right) \qquad (2.36)$$

Where h and r_h are the height and radius of horizontal components. Additionally, the bracings of the Donau tower can reduce the surge impedance of the tower body by around 10 %. Consequently, a surge impedance Z_b must be connected in parallel with the tower body in the equivalent circuit modeling, and Z_b is equal to 9 times the surge impedance of the tower body [78]. The equivalent circuits of two steel towers established in PSCAD are depicted in Fig. 2.15. In addition, the tower span is set to 300 m for lattice steel towers.
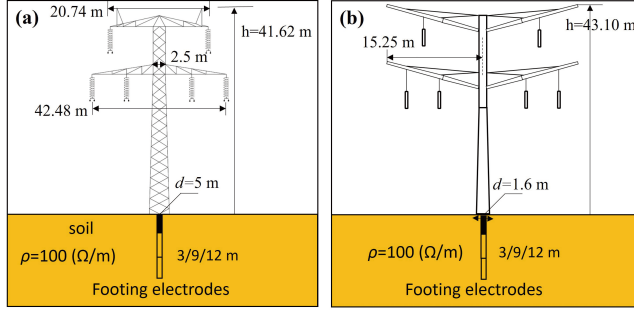
Fig. 2.14: (a) Donau tower and (b) Eagle tower configuration. Source: **C2** [94].
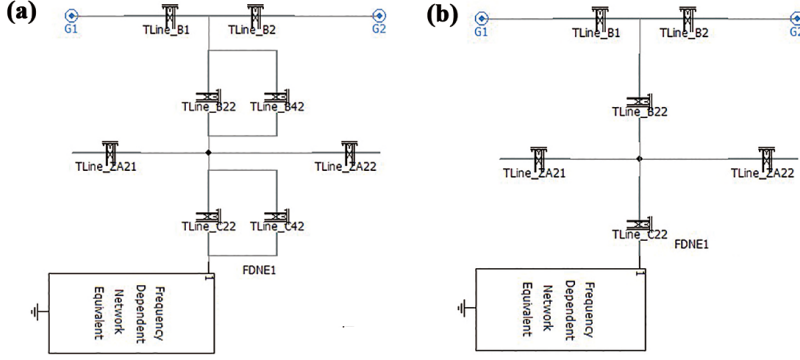
Fig. 2.15: The PSCAD modeling of (a) Donau and (b) Eagle towers.

2.3.3 Lightning Performance Comparison

The critical lightning current I_c for three kinds of towers is obtained by PSCAD simulation. $P_c(I_c)$ is the function that denotes the accumulative probability of lightning current from 0 to I_c. The BFR is calculated by

$$P_c(I_c) = \int_0^{I_c} \frac{1}{\sqrt{2\pi}\zeta x} e^{-\frac{1}{2}\left(\frac{\ln(x/M)}{\zeta}\right)^2} dx \tag{2.37}$$

$$BFR = 0.6 N_L \left(1 - P_c(I_c)\right) \tag{2.38}$$

The number of strikes to the line per 100 km per year (N_L) is demonstrated as [95]:

$$N_L = \frac{N_g}{10} \left(28 h_t^{0.6} + W\right) \tag{2.39}$$

Where W is the horizontal distance between two shielding wires. Considering the worst N_g for the last decade in Denmark is equal to 1.39 flashes/km^2·year [25], the N_L for the Y-shaped pylon is 28.1 flash/100km per year.

The I_c and BFR results are exhibited in Table 2.8 when the lightning strikes at the zero-crossing point of the upper phase voltage. The lattice Donau tower possesses the best lightning protection behaviors. With the same ground electrode, the 'Y' pylon has the lowest I_c. The composite tower has a lower height means a shorter time of the surge traveling along the down-lead, which is beneficial to decrease the overvoltage at the striking point. However, the surge impedance of the down-lead is much higher than the traditional steel towers, resulting in a high BFR even if the long ground rod is adopted. Therefore, optimization for the Y-shaped pylon to increase its lightning protection performance is needed.

Table 2.8: Lightning performance of Donau, Eagle, and Y-shaped pylons.

Lightning Current Waveform	Tower	Electrode Length	I_c (kA)	N_L (flashes/100km-year)	BFR (flashes/100km-year)
CIGRE 3.83/77.5	Y	3 m	105.6		0.0973
		9 m	128.8	28.1	0.0280
		12 m	132.8		0.0228
	Donau	3 m	116.5		0.0742
		9 m	161.1	38.9	0.0079
		12 m	168.3		0.0057
	Eagle	3 m	109.2		0.1177
		9 m	140.4	41.5	0.0229
		12 m	158.3		0.0096

2.4   Summary

In this chapter, the lightning waveform, EMT model for tower down-lead system, ground model, and flashover criterion are discussed, and the modeling for a Y-shaped pylon is mainly emphasized. To improve the model precision, the inclined down-lead surge impedance is expressed in integral form and verified by COMSOL simulation. In addition, the mutual coupling effect and the parasitic capacitance are considered. The steel Donau and Eagle towers are modeled for comparison and the results display that the Y-shaped pylon has the worst lightning protection performance. Further work is needed to optimize the composite pylon and increase its critical current.

Chapter 3

Optimization of Down-Lead System for 'Y' Pylon

As discussed in Chapter 2, the original lightning protection design of the 'Y' composite pylon cannot achieve the expected level. Thus, many factors are going to be investigated to provide an efficient scheme to improve the pylon I_c, such as the down-lead configuration and length, the pylon span, the permittivity of the filling material, the propagation velocity along the down-lead, and shunt capacitances. The optimization content consists of two parts: (1) the optimization of the inclined down-lead inside the cross-arm. (2) the vertical down-lead optimization. In addition, the insulation strength of the composite pylon after optimization is going to be verified. Finally, the lightning protection effect of the optimized tower will be compared with that of the traditional towers.

3.1 Down-Lead Inside Cross-Arm Optimization

3.1.1 Length of Down-Lead

The down-lead length affects the surge traveling time from the striking point to the ground (T_p), and it will further affect the overvoltage level of the tower after being struck by lightning. The effect of the varied down-lead length in the range from 26 m to 30 m on the transient overvoltage across the cross-arm between upper phase voltage and shield wire (U_L) is analyzed. When the tower is struck by lightning with a 31.1 kA crest current (3.83/77.5 μs), the U_L and corresponding I_c are shown in Fig. 3.1. The results illustrate that as the length of the down-lead increases, U_L correspondingly increases and the crest point is delayed. However, the down-lead length cannot be shortened largely due to the fixed pylon configuration. This means the influence of changing the down-lead length in a narrow range on the overvoltage can be neglected
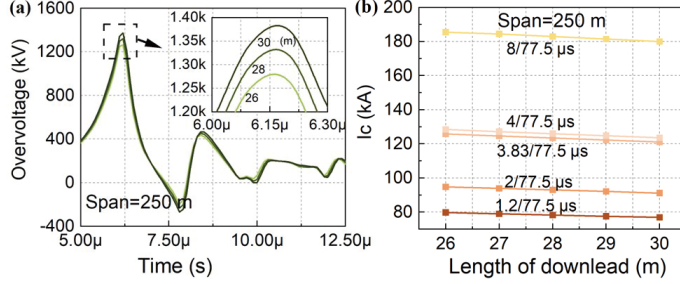
for this kind of pylon.

Fig. 3.1: (a) The U_L waveforms when lightning strikes on 'Y' pylon with different down-lead lengths. (b) The critical current (I_c) against the different down-lead lengths with varied T_f. Source: **J1** [83].

3.1.2 Filling Material Effect

As mentioned before, an appropriate insulation dielectric should be selected for filling the space inside the hollow cross-arm. The dielectric property of the filling material is related to the shunt capacitances of the down-lead, therefore, affecting the surge impedance and velocity of propagation of the down-lead. The influence of dielectric properties of filling material on tower lightning performance should be taken into consideration when determining the filling material.

A. Parasitic Capacitance

The variation of the relative permittivity (k) of the filling material will change the surge impedance and parasitic capacitance between phase conductors and down-leads simultaneously. When filling materials with different dielectric constants are adopted, the transient overvoltage affected by the parasitic capacitance values is studied first. Assuming the surge impedance of each down-lead segment is unchangeable, the EMT model with filling material permittivity from 2 to 6 are built to obtain the U_L when stroke lightning with different T_f and T_t, and the results are shown in Fig. 3.2. The dark and light-colored columns exhibit similar heights, revealing that the variation of parasitic capacitance along with the filling material permittivity change has little effect on the generated overvoltage. Figure 3.2(b) shows that the U_L is almost invariant with an increasing T_t, and it confirms the previous conclusion that the duration of the T_t is independent of the pylon lightning performance [96].

B. Lightning Propagation Velocity Affected By Filling Material Permittivity

The lightning propagation speed can be adjusted by changing the filling material. As aforementioned, an increase in the permittivity will lead to an increase in down-lead capacitance, while the inductance remains the same value. According to the (2.22), the
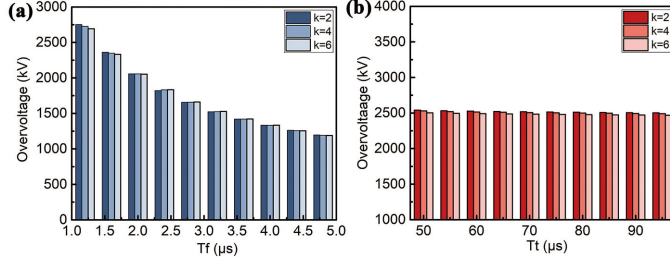
41

Fig. 3.2: When the permittivity k of filling materials changes, the variation of the parasitic capacitance on the transient overvoltage of U_L with different (a) T_f and (b) T_t lightning striking.

surge traveling speed is decreased when the cross-arm is filled with materials of high permittivity. The stroke current propagation speed in segment (1) with different filling material permittivity is shown in Fig. 3.3(a) blue line.

C. Surge Impedance Affected By Filling Material Permittivity

In the same way, the surge impedance of down-lead segment (1) as a function of different filling material permittivity is depicted in Fig. 3.3(a) green line. The increase of the permittivity of the filling material will cause a longer propagation time of the transient surge along the tower down-lead, which means a lower efficiency of conducting lightning current to the ground, causing a higher transient overvoltage on the top of the tower. However, an increase in the permittivity also increases the mutual coupling effect and decreases the surge impedance, which is beneficial for limiting the lightning overvoltage. Thus, which factor plays a leading role with different k needed to be identified. The I_c values stay almost unchangeable with the permittivity increasing as shown in Fig. 3.3(b). It can be concluded that the effect of the propagation velocity deduction and the surge impedance decreasing caused by the rise of k offset each other, showing that the filling material permittivity does not influence the I_c.
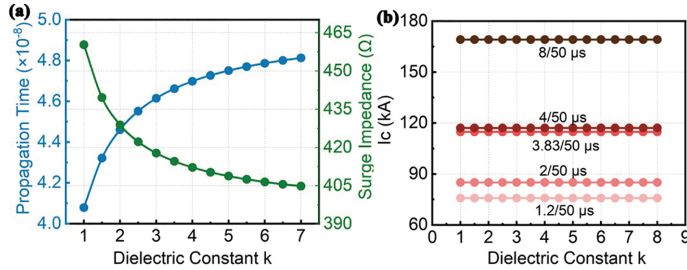

Fig. 3.3: (a) The lightning propagation time per meter and the impedance of the down-lead segment (1) with different k of filling materials. (b) The $I_c - k$ curve of the pylon at different T_f. Source: **J1** [83].

3.1.3 Composite Cross-Arm Radius

Initially, the cross-arm is cone-shaped with a top radius of 0.125 m and a bottom radius of 0.45 m. Considering the effect of the different cross-arm radii on I_c, the initial radius is scaling at a ratio range from 0.25 to 2 to investigate the impact of the cross-arm radius on the lightning performance, and the corresponding propagation velocity and surge impedance of the down-lead segment (1) are shown in Fig. 3.4(a). We can conclude that the radius factor plays a similar role to the permittivity of the filling materials, and it also has little impact on the I_c according to Fig. 3.4(b). Based on this conclusion, the radius of the cross-arm can be adjusted to guarantee there is sufficient insulation strength to avoid puncture without I_c being affected. Therefore, the Ph.D. research does not consider the cross-arm puncture issue.
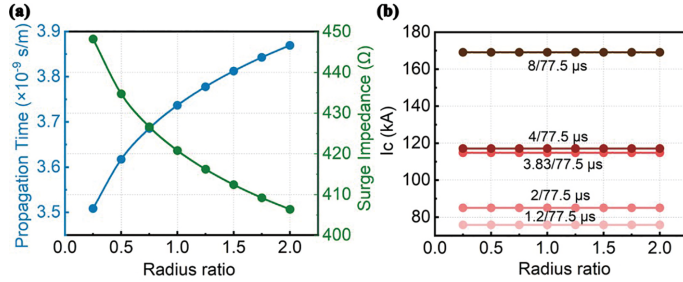
Fig. 3.4: (a) The lightning propagation time and surge impedance of down-lead segment (1) changing with the different scaling ratios of the cross-arm. (b) The relationship between I_c and cross-arm scaling ratio. Source: **J1** [83].

3.2 Vertical Down-Lead Optimization

3.2.1 Multiple Down-Lead System

For the vertical down-leads inside the pylon mast, changing its configuration may lead to a reduction of surge impedance and increase the I_c. Two vertical down-leads inside the pylon body can be connected to form an 'H' frame, and the corresponding surge impedance will be decreased due to the increase of the equivalent radius [51]. If multi-bundled conductors are used as the vertical down-leads, the total surge impedance will be further decreased [78], which can be an optimization scheme for the down-lead system.

A. Surge Impedance of Vertical Down-Leads

For vertical down-leads with n number of conductors, the whole impedance $Z_{T,n}$ is composed of two parts: self impedance $Z_{T,kk}$ and mutual impedance $Z_{T,kl}$ ($k \neq l$),

and the total surge impedance value $Z_{T,n}$ is the arithmetic mean of two parts.

$$Z_{T,n} = \frac{1}{n}(Z_{T,11} + Z_{T,12} + \cdots Z_{T,1n}) \tag{3.1}$$

$$Z_{T,kk} = 60(\ln \frac{2\sqrt{2}h}{a} - 1) \tag{3.2}$$

$$Z_{T,kl} = 60(\ln \frac{2\sqrt{2}h}{S_{kl}} - 1) \tag{3.3}$$

Where S_{kl} is the spacing between the kth and l^{th} cylinders. $Z_{T,n}$ can be rewritten as the form of the surge impedance of a single cylinder with an equivalent radius r_e.

$$Z_{T,n} = 60(\ln \frac{2\sqrt{2}h}{r_e} - 1) \tag{3.4}$$

$$r_e = (2R)^{\frac{n-1}{n}} a^{\frac{1}{n}} \left(\prod_{i=1}^{n-1} \sin \frac{\pi i}{n}\right)^{\frac{1}{n}} \tag{3.5}$$

Where h is 16.5 m. The vertical conductors are arranged as regular polygons inside the pylon mast and the radius of the circumscribed circle is R of 0.5 m (Fig. 3.5(a)).
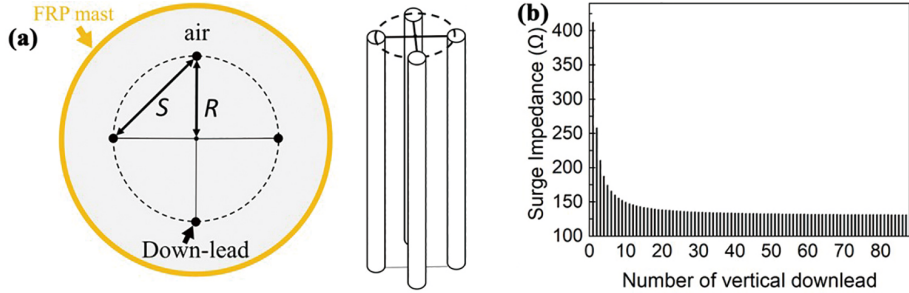
Fig. 3.5: (a) The vertical and front view of the bundle down-leads. (b) The surge impedance of vertical bundle down-leads with the down-lead number increasing. Source: **J1** [83].

In fact, the equivalent radius r_e of the multi-down-lead system is the geometric mean radius of the bundle down-leads, r_e can also be expressed as [2, 97]:

$$r_e = (aS_{11}S_{12}\cdots S_{1n})^{\frac{1}{n}} \tag{3.6}$$

The relationship between the down-lead number and surge impedance is depicted in Fig. 3.5(b). With the number of vertical down-leads increasing, the $Z_{T,n}$ decreases sharply with the range of n from 1 to 10, and then the surge impedance is almost unchangeable as the number of down-lead continues to increase. When the conductor

number n exceeds 87 ($n > [\pi/arcsin(r/R)]$), due to $R \gg a$, the bundle down-leads turn to be a hollow cylinder. At this time, the part of the equation (3.5) is

$$\sqrt[n]{\left(\prod_{i=1}^{n-1} \sin \frac{\pi i}{n} \right)} \approx 0.5 \tag{3.7}$$

Meanwhile, $r_e \approx R + a$, and the total impedance $Z_{T,n}$ can be reformulated as (3.8). The difference between the calculated results obtained by (3.4) and (3.8) is only 0.87 %.

$$Z_{T,n} = 60(\ln \frac{2\sqrt{2}h}{R+a} - 1) \tag{3.8}$$

B. Simulation Verification

To verify the correction of the equation (3.4), the COMSOL RF-module is employed to simulate the surge impedance of the vertical bundle down-leads. Two identical bundled down-leads with a certain center-to-center distance r_d are paralleled built, and the relationship between the impedance of the parallel-bundle Z_{pd} and the equivalent radius of each bundle down-leads r_e conforms to the following equation:

$$Z_{pd} = \frac{1}{\pi} \sqrt{\frac{\mu_0}{\varepsilon_0 \varepsilon_r}} \cosh^{-1} \left(\frac{r_d}{r_e} \right) \tag{3.9}$$

The process of module building is the same as the case of simulating the impedance of the overhead down-leads in chapter 2.2.2. Figure 3.6 depicts the vertical view of the E-field cloud chart of the bundle down-leads with a 3 MV transient overvoltage applied. The simulated and calculated values for the equivalent radius and surge impedance of the vertical multi-downleads are illustrated in Fig. 3.7(a) and (b), respectively. Through the comparison, the largest difference between the simulation and theoretical results is only 2.87 %.

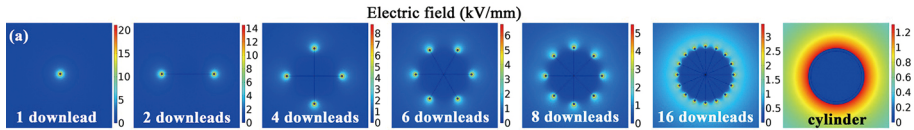**Fig. 3.6:** The top view of the electric field (kV/mm) distribution of the bundle down-leads with 3 MV applied voltages. Source: **J1** [83].

C. Corona Inside Pylon Mast

Because the vertical down-lead inside the hollow FRP mast is exposed to the air, the corona may occur on the surface of the vertical down-lead when a flash of lightning flows through it. In general, the triple conjunction point of the pylon joint where
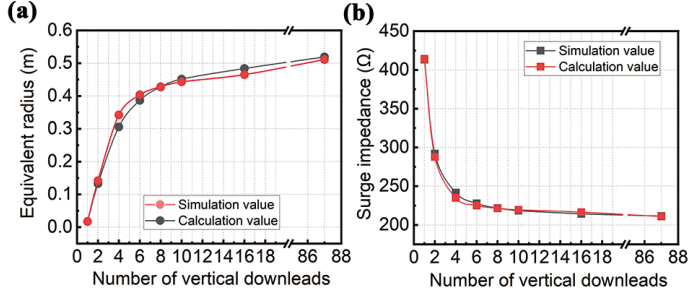
Fig. 3.7: The comparison of (a) the r_e and (b) $Z_{T,n}$ results from simulation and calculation. Source: **J1** [83].

filling material, down lead, and air meet, is a vulnerable region that may be subject to corona aging [98]. When determining the down-lead configuration, it is necessary to take corona occurrence into account. Thus, the corona effect inside the pylon joint is explored by finite element simulation combined with the EMT simulation.

First, the corona inception E-field E_{co} on the vertical down-lead surface should be determined, which can be expressed by (3.10) in standard atmospheric conditions according to CIGRE brochure [63].

$$E_{co} = 2.3(1 + \frac{1.22}{a^{0.37}}) \tag{3.10}$$

For the bundle down-lead with each conductor radius a of 17.5 mm, the corona inception electric gradient is 3.27 kV/mm. Then, the critical threshold voltage able to trigger the corona on the bundle down-lead surface can be simulated by COMSOL software. As illustrated in Fig. 3.8(a), the corona inception voltage experience a rise with the number of the down-lead increasing. Finally, the lightning current amplitude (I_{corona}) through the down-lead that can induce the corona at the triple conjunction point is obtained in PSCAD and shown in Fig. 3.8(b). Meanwhile, the I_c to cause back-flash as the function of the down-lead conductor number is also shown in Fig. 3.8(b). At this time, the lower value of the I_{corona} and I_c determines the critical current for the safe operation of the tower. It can be found that as the number of the down-lead increases from 1 to 16, the corresponding I_{corona} increases gradually to be close to the I_c. When the multi-down-leads form a hollow cylinder ($n > 87$), the I_{corona} jumps as high as 300 kA. It is unlikely to cause the corona at the triple conjunction. Thus, a metal cylinder employed as the mast has enough high inception E-field to avoid the potential corona risk on the mast surface.

3.2.2 Radius Extension of Vertical Down-Lead

The pylon steel pole can be further optimized by expanding the radius to decrease its surge impedance. In the initial design, the pylon mast radius is 0.5 m. As the radius
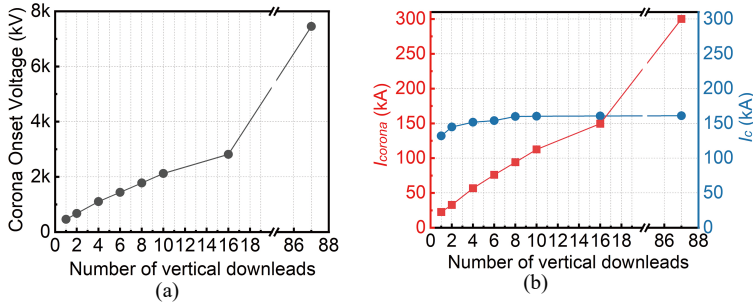
Fig. 3.8: (a) The corona inception voltage as a function of the multi-conductor number. (b) The I_{corona} and I_c as the number of down-lead increases. Source: **J1** [83]

gradually increases up to 1.5 m, the surge impedance is shown in Fig. 3.9(a), and the corresponding I_c (3.83/77.5 μs) increases from 163 kA to 176 kA.
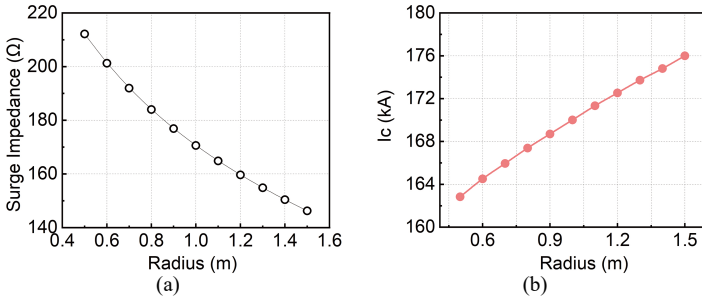
Fig. 3.9: (a) The surge impedance of the pylon mast as the radius increases. (b) I_c of the Y-shaped pylon as a function of the mast radius. Source: **J1** [83].

3.3 Filling Material Selection

After the optimization of the pylon, the steel pole with a radius of 1.5 m is employed as a vertical pylon body. However, the filling material selection for the cross-arm is still pending. The previous research indicates that the influence of permittivity can be ignored when selecting the filling material. Heat Resistant Glass Fiber Reinforced Epoxy Resin (H-GFRP) has already been determined to be used as the hollow cross-arm shell. Then, a variety of polymers or composites which are the most commonly used insulation materials in electrical engineering are investigated as candidates including cross-linked polyethylene (XLPE), silicone rubber (SIR), H-GFRP, and polyurethane foam (PUF), and an appropriate one will be finally determined from the perspectives of electrical strength and thermal stability.

3.3.1 Electrostatic Field Inside Filling Material

The presence of the filling materials should restrict the cross-arm internal E-field lower than the safety operation level. First, a full-scale Y composite pylon is built in COMSOL. The pylon is set up in a sphere air region with the infinite element domain, and the model is meshed by $\sim$ 30,000,000 number of tetrahedral elements. The upper phase conductors are energized with the peak voltage of 420 kV/ $\sqrt{3} \times \sqrt{2}$ =343 kV [61], and the other two phases are applied 343 $\cos(\pm120°)$ kV separately. The copper down-lead is grounded and the floating potential is set on grading rings. The maximum internal field strengths of the four filling materials are shown in Table 3.1. The E-field distribution is associated with the permittivity difference between the filling material and the H-GFRP cross-arm shell. The smaller the dielectric constant difference, the more uniform the internal electric field distribution. That is the reason that the cross-arm filled with H-GFRP has the lowest value. Meanwhile, due to the air pore inside the PUF, the maximum long-term withstand E-field is air ionization E-field [99]. However, the surface E-field of the down-lead with PUF as filling material is higher than the threshold (Fig. 3.10). Thus, the PUF should be excluded, and H-GFRP is the preferred material.

Table 3.1: Filling material parameters and maximum E-field inside materials.

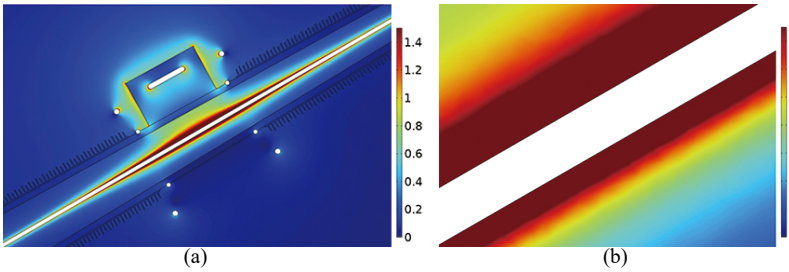| Material	Permittivity	Maximum E-field by simulation	Maximum withstand E-field
XLPE	2.3 [100]	2.83 kV/mm	3 kV$_{RMS}$/mm [61, 101]
SIR	3.73 [61]	2.50 kV/mm	3 kV$_{RMS}$/mm [61, 101]
H-GFRP	5.75 [61]	1.98 kV/mm	3 kV$_{RMS}$/mm [61, 101]
PUF	1 [102]	3.75 kV/mm	2.66 kV/mm [99]

Fig. 3.10: (a) The cross-section E-field distribution (kV/mm) of cross-arm filled with PUF, and (b) the local zoomed figure of the down-lead region.

3.3.2 Ampacity Verification of Down-Lead

Due to the presence of the filling materials, the ampacity of the down-lead should be verified to avoid aging even ablation of the filling material in the case of being struck

by lightning. The ampacity of the down-lead depends on the down-lead material and thermostability of filling materials. For the down-lead covered with the filling material, the current conduct capacity of the down-lead inside the cross-arm can be evaluated by referring to the method of cable ampacity verification [103]. Due to the very short lightning duration, the lightning current conduction through the down-lead inside the cross-arm can be regarded as the adiabatic short-circuit, the maximum ampacity is I_{AD}.

$$I = K_c S_A \sqrt{\ln \frac{\theta_f + \delta}{\theta_i + \delta} / t} \qquad (3.11)$$

$$I_{AD} = \sqrt{\frac{1}{t} \int_0^t I^2 \cdot dt} \qquad (3.12)$$

Where t is the whole duration of a lightning discharge, and the median value is about 200 ms [51]. K_c is a coefficient that is recommended to be 226 A$s^{1/2}/mm^2$ for copper [103]. θ_f is the transient maximum withstand the temperature of filling materials. According to [104], the transient withstand temperature is about 250 °C for XLPE, and > 300 °C for SIR and H-GFRP [105]. θ_i is the environmental temperature. According to the CIGRE brochure, the long-term operation-rated temperature of the phase conductor is about 70 °C [106]. Assuming the worst case is that the operating temperature of the filling material is 70 °C. δ is associated with the resistance temperature coefficient of copper. S_A is the cross-sectional area of the copper core (mm^2). Taking into account the scenario where a lightning flash lasts 200 ms, I_{AD} for XLPE is > 331 kA and > 364 kA for SIR/H-GFRP, and the corresponding probabilities are less than 8.6×10^{-6} and 3.1×10^{-6} flashes/100km-year. Thus, the down-lead dimensions and three kinds of filling materials meet both thermal and electrical requirements.

In fact, all XLPE, SIR, and H-GFRP satisfy the requirements of filling material. If the H-GFRP is used as the cross-arm shell and filling material, there is no interface issue due to the same material. Meanwhile, H-GFRP has good insulation, chemical resistance, and the highest long-term operating temperature ($\gg$300 °C [105]) with low dielectric loss and mechanical property. For these reasons, we choose the H-GFRP as the filling material [107].

3.4 Insulation Strength Between Conductor and Mast

When the steel cylinder replaces the hollow FRP body of the pylon, the probability of flashover between the pylon mast and the lower phase conductor should be considered. Therefore, whether there is enough insulation strength between the lower phase conductor and mast should be investigated. When the shield wire is struck by lightning, flashover may happen in two places of the pylon: place (1) is between the shield wire and the upper conductor (U_L), and place (2) is between the lower conductor and pylon mast (U_d). Flashover in place (2) between two grading rings can be seen as similar

to a discharge in an air gap [63]. Therefore, LPM used for the air gap can be used to determine whether the flashover happens in the region (2).

When the amplitude of the lightning current striking the tower top is a little lower than I_c (Fig. 3.11(a)), the U_d is about 1100 kV and no flashover happens on the place (2) (Fig. 3.11(b)). The voltage on the upper phase conductor is only an induced voltage of 700 kV. If the lightning current is 300 kA, the flashover happens at 6 μs (Fig. 3.11(d)). The overvoltage in place (2) is only slightly increased (Fig. 3.11(e)), but the upper phase voltage considerably increases to more than 6000 kV (Fig. 3.11(f)). That means once the overvoltage on the region (1) causes a backflash, the upper phase conductor will divert a huge lightning current to keep the region (2) from discharge. Thus, it indicates that the optimized pylon is sufficiently strong in the insulation to prevent the local flashover on the pylon body.
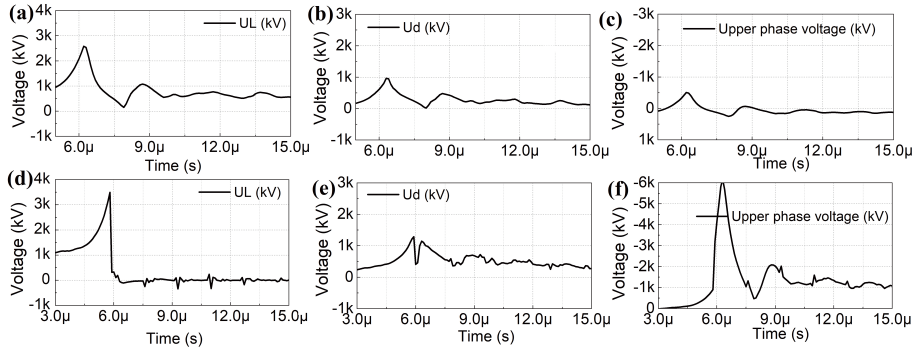
Fig. 3.11: When striking current (3.83/77.5 μs) is lower than I_c, (a) the overvoltage U_L shown in place (1), (b) the U_d waveform shown in place (2), and (c) the upper phase conductor voltage waveform. When the lightning current is 300 kA, (d) the U_L, (e) the U_d, and (f) the upper phase voltage waveforms with time. Source: **J1** [83].

3.5 Lightning Performance After Optimization

After the optimization of the down-lead and the selection of filling materials, the I_c and BFR are recalculated and shown in Table 3.2. Where I_c refers to the arithmetic mean of I_c considering a full phase angle. With a ground rod length of 12 m, the BFR decreases by an order of magnitude from 0.0228 to 0.0028 flashes/100km-year compared with the original design, which is 12.3% of the original design. Compared with the 400 kV Donau and Eagle pylons made of steel, the 'Y' pylon has the highest I_c and lowest BFR. In the following, the lightning performance comparison among the Y-shaped pylon and steel towers is analyzed from upper phase voltage at the striking moment, ground rod length, and lightning front time.

Table 3.2: Lightning performance of Y-shaped pylon, Donau, and Eagle towers.

Lightning Current Waveform	Tower	Electrode Length	I_c (kA)	N_L (flashes/100km-year)	BFR (flashes/100km-year)
CIGRE 3.83/77.5 μs	Y	3 m	125.9	28.1	0.0328
		9 m	168.1		0.0041
		12 m	175.6		0.0028
	Donau	3 m	115.9	38.9	0.0742
		9 m	159.8		0.0079
		12 m	167.8		0.0057
	Eagle	3 m	102.4	41.5	0.1718
		9 m	131.1		0.0367
		12 m	136.9		0.0273

A. Upper Phase Voltage

For a transmission tower with a voltage level above 220 kV, the phase voltage cannot be neglected when calculating the BFR [108, 109]. Assuming the upper phase voltage is $343\sin(t + \theta)$ kV and $t + \theta$ is the phase angle, the critical currents for Y-shaped, Donau, and Eagle towers (I_{cphase}) as a function of the phase angle are depicted in Fig. 3.12(a). Here, the I_c of the tower is represented by the arithmetic mean of the I_{cphase}. The I_{cphase} can be approximately expressed as a sine function.

$$I_{cphase} = \Delta I_c \left[-\sin(t + \theta) \right] + I_{c0} \tag{3.13}$$

Where I_{c0} is a constant value when the lightning strike time is the zero crossing point of the upper phase voltage, which is almost the same as I_c. ΔI_c is the fluctuation amplitude affected by the phase voltage. The ΔI_c and I_{c0} for three kinds of transmission towers are shown in Table 3.3. It can be concluded that the Y-shaped pylon is the most susceptible pylon to the phase voltage due to the highest ΔI_c, which is mainly attributed to the lower flashover withstand voltage of the cross-arm because the clearance for Y composite pylon is only 2.8 m compared with that of 3.2 m for steel towers. However, even in the worst case that the lightning strikes with the upper phase voltage reaching its crest, namely, the phase angle is 90 °, the Y-shaped pylon still has the highest critical current.

Table 3.3: ΔI_c and I_{c0} of Y-shaped pylon, Donau, and Eagle towers.

Electrode lengths	Y		Donau		Eagle	
	ΔI_c	I_{c0}	ΔI_c	I_{c0}	ΔI_c	I_{c0}
3 m	22.4	126.6	17	116.5	15.2	103.3
9 m	28.9	168.8	19.6	160.4	18.2	132
12 m	29.3	176.3	20.6	168.4	17.8	137.8

B. Ground Length Effect

With the ground rod increase, the corresponding I_c of the three towers has greatly increased with the electrode rod from 3m to 9 m, and then slightly increases with the 12 m rod as shown in Fig. 3.12(b). For all towers, the shorter the ground rod length, the lower the value ΔI_c, revealing that the higher ground impedance can restrict the influence of the phase voltage on the I_c.
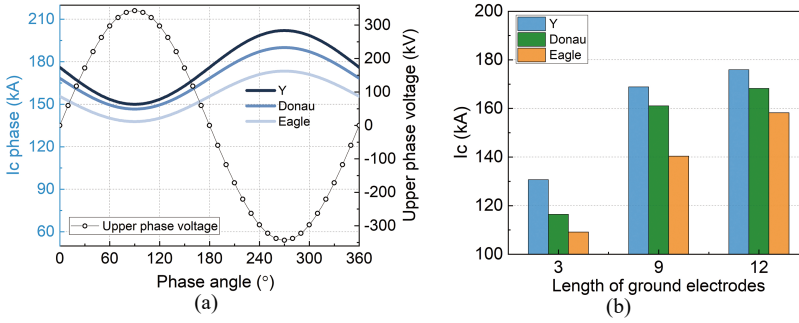
Fig. 3.12: (a) I_c of three types of towers as a function of the phase angle of the upper phase conductor. (b) The mean I_c of three types of towers with different ground electrode lengths.

C. Different Lightning T_f

Meanwhile, the lightning performance I_c and BFR as a function of T_f which ranges from 0.1 to 10 μs is investigated, and the I_c-T_f curve and BFR-T_f curve are depicted in Fig. 3.13(a) and (b), respectively. Taking the length of the grounding electrode as 12 meters as a concern, the Y composite pylon after optimization also shows the lowest BFR. It should be noted that with the extremely short T_f lower than 1.5 μs, the I_c of the Donau tower is slightly higher than that of the Y composite tower, while the BFR is lower than the Y pylon. This is because the N_L of the Y tower is about three-fourths of Donau's value due to its lower height and more compact pattern. Therefore, it can be concluded that the 'Y' composite tower with the optimal down-lead dimensions is very competitive with good lightning performance.

3.6 Summary

This chapter studies the potential multi-factors that may affect the lightning performance of the 'Y' composite pylon. Based on the results, the optimization scheme for the down-lead system and the filling material for the cross-arm are determined. By the means of transient simulation in PSCAD/EMTDC, many factors including the length, the configuration of down-lead, and the permittivity of filling materials on the
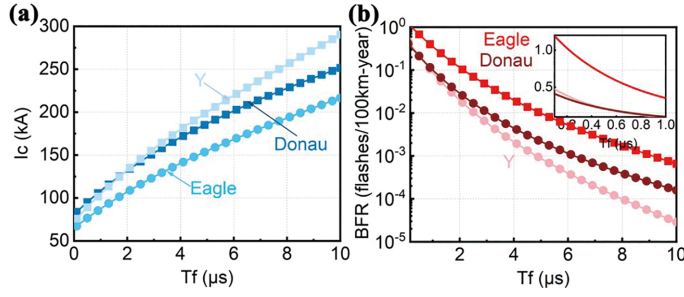
Fig. 3.13: (a) I_c and (b) BFR as a function of T_f for Donau, Eagle, and Y-shaped composite towers. Source: **J1** [83].

lightning performance are investigated. According to the research, the permittivity of filling materials has almost no influence on the I_c. However, the number and arrangement of the down lead are dominant factors in the lightning performance. Additionally, taking the electrostatic field and down-lead ampacity into consideration, H-GFRP is selected to fill the cross-arm. The final version of the optimized tower has a steel body with a 1.5 m radius. Finally, through the EMT simulation, the I_c with different T_f of the optimized Y pylon is computed. Meanwhile, the influences of upper phase voltage, ground rod length, and lightning front time on I_c are evaluated. With the optimal down-lead system, the lightning performance is largely improved and better than 400 kV Donau and Eagle pylons.

Chapter 4

Feasibility of Cable As Down-lead

Through a series of optimization measures, the Y-shaped pylon shows good lightning protection characteristics. Meanwhile, the insulation issues inside the cross-arm are solved by filling insulating materials into the cross-arm. However, the use of filling materials will complicate the manufacturing process, and reduce the mechanical stability of the pylon due to the higher cross-arm load imposed on the pylon joint. The gap between the cross-arm and bare conductor is filled by H-GFRP in response to inhibiting the electric field density on the surface of the down-lead. If the down-lead is only wrapped with a certain thickness of insulation material passing through a hollow cross-arm, the surface insulation problems on the down-lead may also be settled. In other words, cables have the potential to be used as down-lead. By doing so, the manufacturing process can be simplified, and the mechanical stress on the pylon joint will also be relieved. An additional benefit of this approach is that if insulation failure of the cable happens, it can be substituted and recycled. It can be a further optimization scheme for the down-lead inside cross-arms. Nevertheless, whether the hollow cross-arm within a cable can meet the insulation requirements is unclear. This special configuration involves possible insulation problems as follows.

- The partial discharge inside the cross-arm is non-allowable in a long-term operation. The interface partial discharge depends on multiple factors such as electrode configuration [110], applied voltage polarity and waveform [111, 112], material type [113], charge accumulation [114] and environmental conditions [115]. However, there is little systematic research concerning the insulation conditions of a hollow cross-arm with a cable passing through.

- With the cable as a down-lead, it is not clear if the composite tower has good lightning protection performance and adequate insulation to avoid cable puncture.

In this chapter, systematic research is carried out to verify the feasibility of using cable as the down-lead to ground the shield wire. Chapter 4.1 introduces the construction of the scaled cross-arm model and experimental platform. In chapter 4.2, the preliminary cable down-lead parameters are determined based on the corona onset characteristics of the cylinder. Considering the switching overvoltage condition, the cable parameters are re-calibrated shown in chapter 4.3. Then, the transient electromagnetic model of the down-lead system is built in PSCAD considering the impulse corona effect to simulate the internal overvoltage inside the cross-arm in chapter 4.4. Finally, the lightning performance of the pylon adopted with the cable as down-lead is analyzed, and the insulation strength of the cable at transient overvoltage is verified.

4.1 Experimental Setup

4.1.1 Building Scale Cross-Arm Model

In this chapter, the research employs FEM simulation and experiments to design the cable parameters as a down-lead according to the insulation requirements. The full-scale cross-arm model is too large to be built in the laboratory, therefore, the down-scaled model of cross-arm within the cable is built to study the internal insulation phenomenon. By analyzing the internal electric field environment inside the full-size cross-arms while the pylon is in operation, the design scheme for the down-scale model of the pylon can be determined. According to the FEM model for the pylon aforementioned in Chapter 3.3.1, the E-field distribution inside the cross-arm is obtained and the cross-section E-field view is shown in Fig. 4.1. The contour plot exhibits that the E-field intensity in the circumferential direction around the cable inside the cross-arm can be considered approximately uniform. The dielectrics between the down-lead and phase conductors are the cable layer, air, and cylinder H-GFRP layer. Thus, the cross-arm structure can be equivalent to two insulation coaxial cylinders with an air gap.
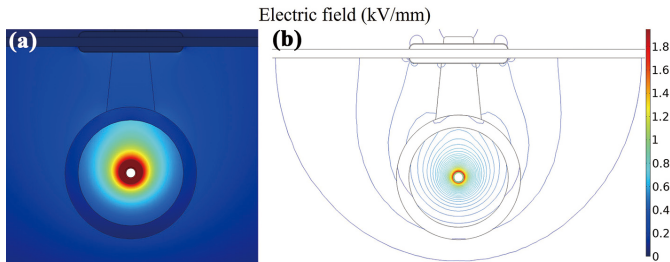

Fig. 4.1: (a) The E-field distribution and (b) contour plot of the cutting plane of the cross-arm. Source: **J3** [67].

For the scale model, two H-GFRP pipes purchased in Fengchuang Power Facilities Co., Ltd with different diameters are nested and fixed with their central axes coinciding.

4.1. Experimental Setup

The pipes are made of high thermal performance glass-fiber reinforced epoxy resin, and the thickness of each pipe wall is 2 mm. Copper tape is pasted on the external surface of the outer cylinder and the internal surface of the inner cylinder to resemble the down-lead and phase conductor, and all the copper edges are covered by insulation tapes to avoid undesired partial discharge (PD). The dimension parameters of a pair of typical pipes are shown in Fig. 4.2. In this experiment, four coaxial cylinders with different inner pipe radii r_1 of 15 mm, 16 mm, 20 mm, and 25 mm are built to test.

The electric field distribution inside the cross-arm is also affected by the external phase conductors, and the electric intensity generated by the phase conductor in the scaled model can be adjusted by pasting a metal coil on the external surface of the cross-arm. In practice, phase conductors are only placed on one side of the cross-arm, therefore, to resemble the real electric field environment generated by the phase conductor, different coating strategies that one to four quarter circumferential copper coatings on the external cylinders are tried on a pair of co-axial cylinders with R_1=22 mm, and r_1=16 mm. The corresponding E-field distribution depicted in Fig. 4.3(a)-(d) shows that the electric field distribution inside the scaled cross-arm with the fully circumferential cover of the copper is nearest to that of the real cross-arm.
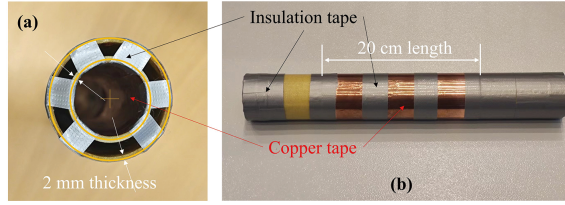
Fig. 4.2: The dimension parameters of the nested pipes from (a) side view and (b) front view.
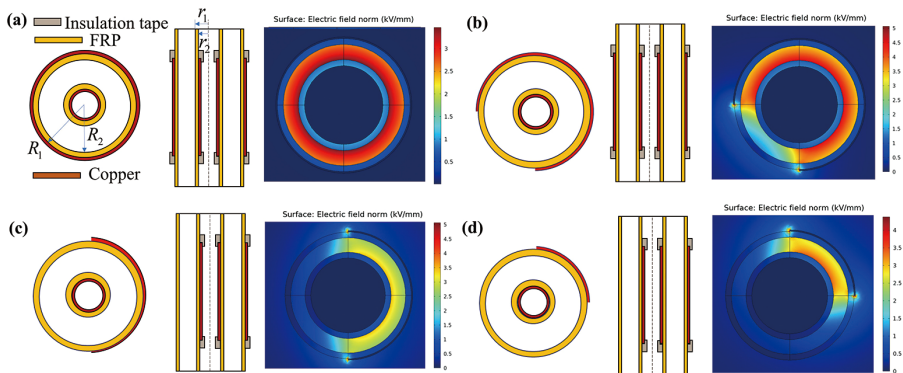
Fig. 4.3: (a)-(d) The schematic of the coaxial cylinder model pasted with 4, 3, 2, and 1 quarter circumference copper from the top view and front view, respectively, and the corresponding E-field distribution inside the coaxial cylinders. The cylinder parameters are R_1=22 mm, R_2=20 mm, r_1=16 mm, and r_2=14 mm, and the external copper is high voltage side with the 10 kV$_{RMS}$ applying.

4.1.2 Cross-Arm Corona Test Platform

A power frequency voltage is applied on the external surface of the outer pipe to test the onset threshold voltage of the inner cylinder as a function of the radius r_1. The circuit of the test setup is shown in Fig. 4.4. In order to make the test environment closer to reality where the cable is fixed inside the air-tight cross-arm to prohibit condensation on its surface, the coaxial cylinders are placed in a column chamber, and then tightening the bolts to seal it. A 50 Hz AC source connects to a charging resistor and links with the chamber. The bottom ending of the chamber is connected with the internal copper of the inner pipe. Then, the chamber end is grounded through a capacitor C_m, which is used to measure the charge across the coaxial cylinders and obtain the corona power. The source voltage and the voltage stressed on C_m are recorded by voltage probes.

Experimental setup · Schematic of experimental setup
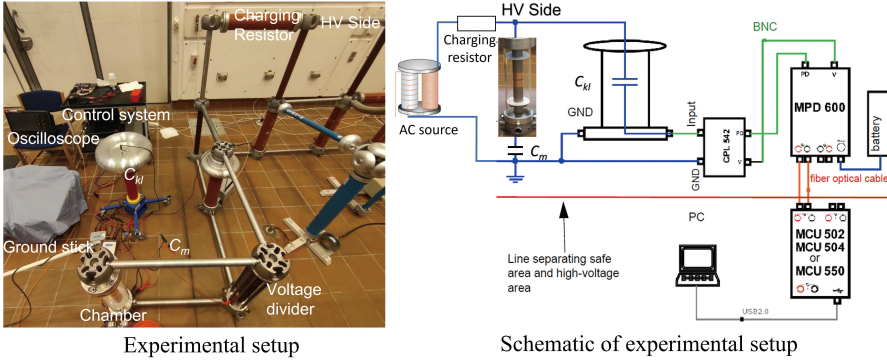
Fig. 4.4: The pictorial view and equivalent circuit of the PD measuring setup. Source: **J3** [67].

The partial discharge detector MPD 600 produced by OMICRON is employed to judge the corona onset. A coupling capacitor C_{k1} is linked with the high voltage side in parallel to synchronize the PD detection. Finally, the corona inception voltage is converted into corona inception field strength through the FEM simulation [116].

4.1.3 Lightning Test Platform

The lightning test platform is used to test the withstand voltage of the scale cross-arm as shown in Fig. 4.5. A fast-front negative impulse voltage is employed and loaded on the internal surface of the inner cylinder. The lightning test system can generate a maximum of 65 kV lightning voltage with $T_f = 1.2 \pm 20\% \, \mu s$ and $T_t = 50 \pm 20\% \, \mu s$ (Fig. 4.6). For the lightning test, the external surface of the outer cylinder is grounded. The trigger detection system can record the impulse signal in the chamber and judge whether a breakdown happens (Fig. 4.5(c)).
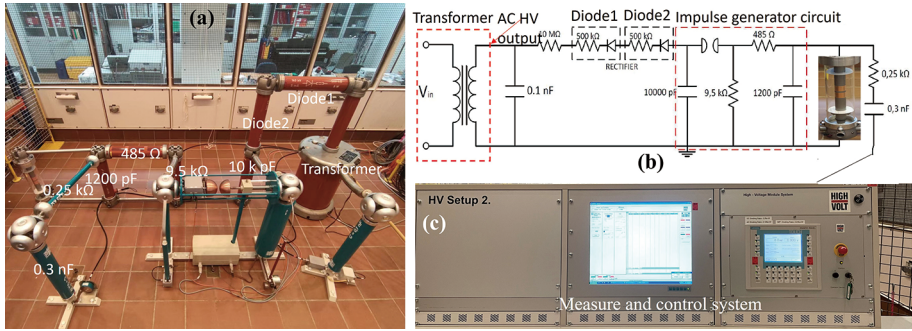
Fig. 4.5: (a) The lightning impulse generator system. (b) The equivalent circuit of the impulse generation system. (c) The control and detection system of the impulse generator. Source: **J3** [67].
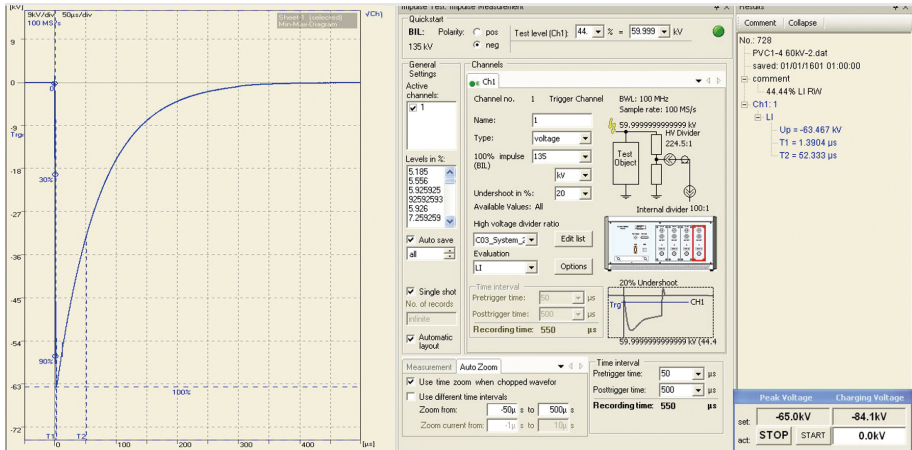
Fig. 4.6: The display interface of 65 kV lightning test waveform recorded on the coaxial cylinders.

4.2 Cable Design

In the cable down-lead design, the E-field density on the dielectric interface or inside the materials should be within the safety threshold to avoid insulation failure occurring. The criteria for the selection of cable should be stated:

(1) When the phase conductor operates at a rated voltage in the steady state, any corona is not allowed in any cross-arm regions.

(2) In the case of transient overvoltage such as lightning or switching surge, the corona inside the cross-arm will not cause permanent damage to the insulating material (ablation or breakdown).

4.2.1 Corona Onset E-field

The corona inception E-field for cable cover should be determined. The corona onset threshold for metal cylindrical electrodes has been extensively studied, and it is affected by multiple factors. An empirical formulation for the corona onset gradient E_c was first generalized by Peek [117].

$$\frac{E_c}{\delta_a} = E_0 \cdot m \cdot \left(1 + \frac{B}{(\delta_a \cdot r_1)^C}\right) \tag{4.1}$$

Where $E_0\ (kV_{peak}/cm)$ is the E-field gradient measured in a standard atmospheric environment. r_1 is the radius of the cylinder; m is a coefficient factor that is related to roughness or material type [113]. B and C are constants. δ_a is the relative air density:

$$\delta_a = \frac{3.92 P_a}{273 + T_c} \tag{4.2}$$

Where P_a is the air pressure in cm Hg, and T_c is the temperature in °C. The experimental temperature is 19 °C and δ_a is 0.9556. The formulas are derived from experiments based on metal coaxial cylinders. The cross-arm has the same configuration but the corona emanates from the composite surface rather than the metal surface. In this research, we employ high sensitive PD system to measure the corona inception of coaxial insulation cylinders and modify the parameters in equation (4.1).
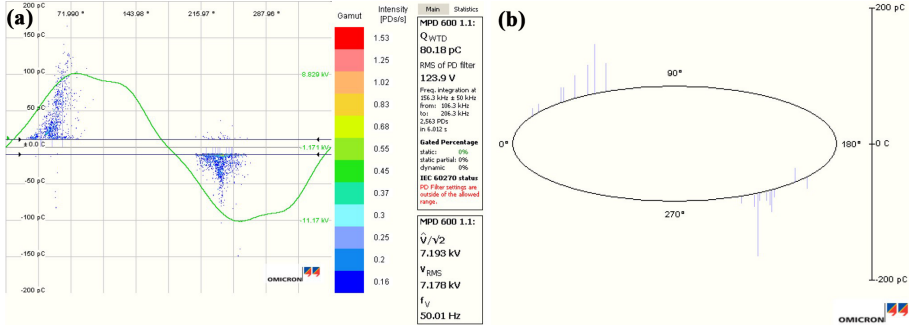
Fig. 4.7: (a) The typical PD pattern of corona onset with an applied voltage of 7.19 kV_{RMS}. (b) The PD phase in a whole period.

The typical corona PD signal pattern is shown in Fig. 4.7. The onset E-field for cylinders with radii r_1 of 16 mm, 17 mm, 20 mm, and 25 mm are 2.80 kV/mm, 2.78 kV/mm, 2.74 kV/mm, and 2.69 kV/mm. The corresponding coefficients in (4.1) can be obtained by curve fitting. The expression of E_{c0} is modified as follows in the standard atmospheric conditions.

$$E_{c0} = 2.459 \left(1 + 0.745/\sqrt{r_1}\right)) \tag{4.3}$$

The corona inception E-field values on the cable cover/metal cylinder with different radii are plotted in Fig. 4.8, and the coefficients of $E_c - r_1$ curve resulting from the previous reference are shown in Table 4.1. It is demonstrated that the corona inception E-field curve pattern on the dielectric material is similar to the curve for metal with the same coaxial cylinder configuration. However, the corona onset values on H-GFRP are a little lower than the value on metal cylinders, which may be primarily attributed to the roughness of the H-GFRP. The essence of the corona is air ionization at the interface subjected to a certain E-field intensity. The determinants for corona inception on cylinders are the curvature and material roughness m.
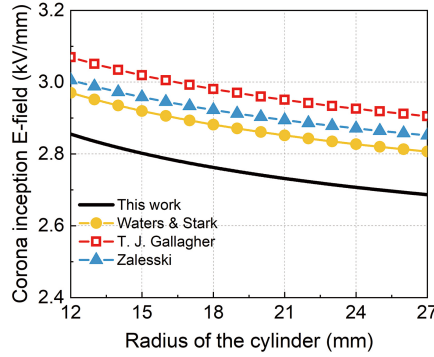
Fig. 4.8: The corona inception E-field against the cylinder radius in standard atmospheric conditions. Source: **J3** [67].

Table 4.1: The coefficients in (4.1) from the previous research on steel cylinders. Source: **J3** [67].

Reference Authors	$E_0 m$	B	C
Waters & Stark [118]	2.38	0.67	0.4
T. J. Gallagher [119]	2.45	0.65	0.38
Zalesski [112]	2.45	0.613	0.4

4.2.2 Cable Radius Determination

We employ the full-size pylon simulation in COMSOL to obtain the relationship between the cable radius and the surface electric field magnitude. The down-lead cable core radius is a fixed value of 1.75 cm, and different thicknesses of the insulation layer are selected. The maximum E-field strength occurs on the surface of the cable below the upper phase conductor due to the short diameter of the cross-arm in this region [61]. As the radius of the cable increases, the surface E-field strength displays a logarithmic downward trend in Fig. 4.9. Combined with the onset E-field results, there is no corona inception on the operation condition when the cable radius is beyond 4.22 cm. The corresponding E-field cloud chart inside the cross-arm is displayed in Fig. 4.10.
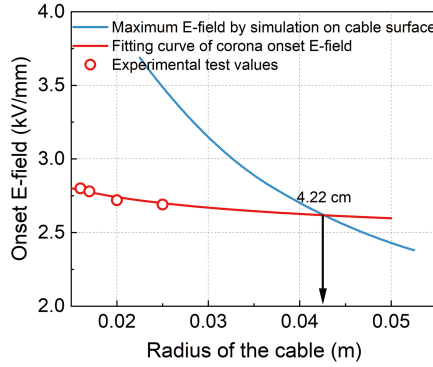
Fig. 4.9: The onset E-field of corona and the maximum E-field on the cable surface at different cable radii.
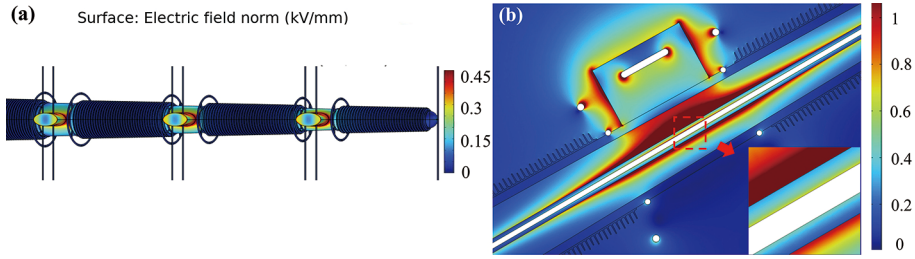
Fig. 4.10: (a) The volume E-field norm of the cross-arm. (b) The cross-section E-field of the cross-arm with a cable radius of 4.22 cm. Source: **J3** [67].

4.3 Switching Overvoltage Condition

In a transmission power system, transient overvoltage induced by switching operation is inevitable. The switching surge values are varied from the scenarios [120]. In transmission line systems, pre-insertion resistor circuit breakers along with the use of suitable surge arrestors can be adopted to mitigate switching overvoltage in the range of 1.5 p.u. to 2.0 p.u. [121, 122]. Here, 2 p.u. rated voltage is stressed on the upper phase conductor to compute the surface electric field on the cable surface. Of particular concern is that PD induced by the switching surge normally lasts a few milliseconds [123]. For the selection of an appropriate cable, the instantaneous corona is allowed as long as it does not cause serious damage to the material. Thus, the damaging effect of the instantaneous corona should be taken into consideration.

4.3.1 Corona Power Loss

AC test platform is used to test the corona power loss of the cross-arm scale model. The applied voltage ranges from 1 to 2.5 times the PD onset voltage. Due to the pres-

ence of the insulation cylinders, this kind of corona discharge belongs to dielectric barrier discharge (DBD). In general, the Charge-Voltage Lissajous plot is commonly used to estimate the power consumption [124]. The charge Q flows through the cylinders can be acquired by

$$Q = V_m \cdot C_m \tag{4.4}$$

Where V_m is the voltage stressed on the externally connected capacitor C_m. The current through the capacitor is given by

$$I_m(t) = C_m \frac{dV_m(t)}{dt} \tag{4.5}$$

I_m is the current through the C_m, and the value is the same as the current through the coaxial cylinders. Thus, the instantaneous power loss is

$$P(t) = V_a(t) \times I_m(t) = V_a(t) \times C_m \frac{dV_m}{dt} \tag{4.6}$$

Where V_a is the voltage across the coaxial cylinders.

$$\bar{P} = \frac{1}{T} \int_0^T V_a(t) C_m \frac{dV_m}{dt} dt = \frac{1}{T} \int V_a(t) C_m dV_m$$
$$= \frac{1}{T} \oint V_a dQ_m = S / T \tag{4.7}$$

The closed integration of the instantaneous V_a and dQ_m is the enclosed area S of the $Q - V$ Lissajous curve. Then the area inside the closed Lissajous curve divided by the 50 Hz AC cycle period (T) is equal to the corona power.

Through the investigation, it can be found that the power loss exhibits an initial stable and then exponential rise (Fig. 4.11), and it would not jump immediately to a destructive level when the E-field slightly exceeds the onset value. This phenomenon is highly associated with the physical process of discharge. Originally, the faint corona starts with the gas E-field beyond the inception gradient, and the charge accumulates on the dielectric surface to form a reversed E-field to offset the initial field strength, and as a result, the discharge extinguishes due to insufficient electric field maintenance. The charge on the surface of the insulation dielectric accumulates instantaneously while dissipating slowly. Thus, it is difficult to discharge continuously after one discharge with an unchangeable applied voltage. From a macro perspective, the discharge shows intermittent filamentous discharge. As shown in Fig. 4.12(a), the pulse on the waveform of V_m reflects the intermittent discharge only occurs at the crest of the applied voltage (V_{crest}), which matches with the picture of discrete discharge (Fig. 4.12(b)). This discharge period refers to period 1 in this manuscript.

If the applied voltage V_a increases further, the discharge restarts until the applied voltage reaches its peak value. As the V_a increases from V_i to V_{crest}, the discharge
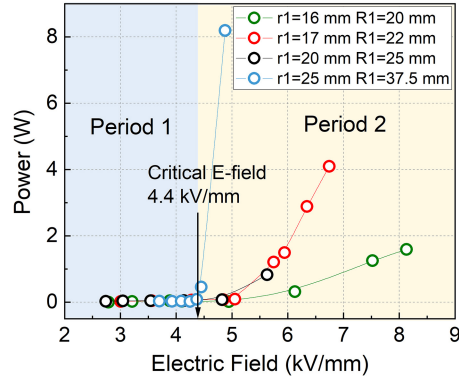
Fig. 4.11: The corona power consumption as a function of E-field strength. Source: **J3** [67].

will be triggered continuously although each discharge lifetime is very short (1–10 ns) [125] due to the charge accumulation. In this process, the discharge occurs at the rising edge of the $|V_a|$ as shown in Fig. 4.12(c), and the numerously filamentary discharges fill the air gap in Fig. 4.12(d). This process is defined as period 2.
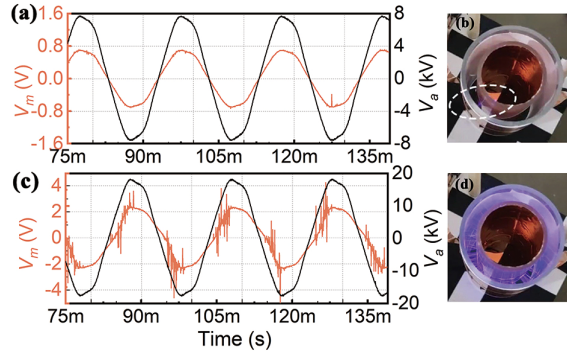
Fig. 4.12: The V_a and V_m waveforms in the discharge (a) period 1 and (c) period 2. The photo of discharge of (b) period 1 and (d) period 2. Glass cylinders are used to visualize the discharge process. Source: **J3** [67].

4.3.2   Cable Parameter Resetting

As the corona power loss remains at a lower level in period 1, the PD in this stage has an insignificant impact on the H-GFRP material. However, the corona loss in period 2 will rise exponentially with the increase of E-field. The critical E-field for distinguishing the two periods is about 4.4 kV/mm (Fig. 4.11). When the E-field on the cable surface is within 4.4 kV/mm under switching operation, the insulation design meets the safe operation requirements. Keeping the radius of the cable core constant (17.5 mm) and changing the thickness of the insulation layer of the cable, the maximum

E-field on the cable surface as the function of the radius is shown in Fig. 4.13 when the applied phase voltage on the phase conductor is 2.0 p.u. of rated voltage. Combined with the experimental results of the corona power loss, the cable will operate in a safe condition with a radius at least of 4.35 cm.
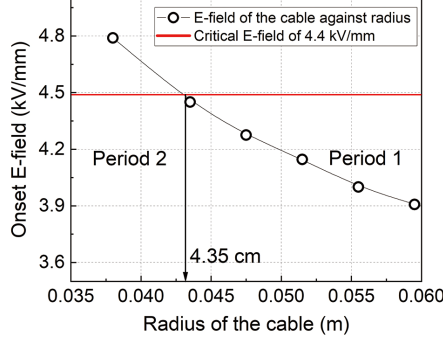
Fig. 4.13: The maximum E-field along the surface of the cable by simulation as a function of the radius with 2 times of rated phase voltage. Source: **J3** [67].

4.4 Lightning Performance

4.4.1 Impulse Corona Effect On Down-Lead Surge Impedance

As the hollow cross-arm is adopted in this chapter, the corona inside the cross-arm induced by lightning striking should be considered. The occurrence of the corona changes the self-capacitance of the down-lead. Thus, the surge impedance of the inclined down-leads needs to be recalculated. For the inclined down-lead segments, the surge impedance Z_c is determined by capacitance C and inductance L of the down-lead. The corona sheath on the surface of the down-lead only affects its capacitance but not inductance [51, 126]. For the capacitance of the down-lead, the value directly depends on the magnitude and the change rate of the applied voltage. According to the previous work [127, 128], the capacitance is dq/dV, and the $Q-V$ curve gives the regulation of the capacitance development. Neglecting the effect of the thickness of the hollow cross-arm, the value of C is a piecewise function. In the case of V_a below the inception voltage V_i, C is considered as a geometric capacitance, C_{geo}.

$$C_{geo} = 2\pi\varepsilon_0 / \int_{x_i}^{x_{i+1}} \ln\left[\frac{2(16.5 + x\tan 30°)}{a/\cos 30°} - 1\right] dx \qquad (4.8)$$

When the increased voltage is above the corona threshold voltage to emanate the streamer from the conductor, the capacitance of the down-lead will be correspondingly increased. According to Grey model [128], the capacitance is expressed as (4.9).

$$C = C_{geo}\eta(V/V_i)^{\eta-1} \qquad (4.9)$$

Fig. 4.14: The dynamic capacitance of the down-lead segment with the lightning striking. Source: **J3** [67].

Where coefficient η is given by $1.121 + 6.8a$ for negative polarity. However, the shell of the cross-arm will restrict the expansion of the streamer radius and there is an upper limit of the dynamic capacitance value C_{cor}. Where b is the radius of the cross-arm.

$$C_{cor} = 2\pi\varepsilon_0 / \int_{x_i}^{x_{i+1}} \ln\left[\frac{2(16.5 + x\tan 30°)}{b/\cos 30°} - 1\right]dx \qquad (4.10)$$

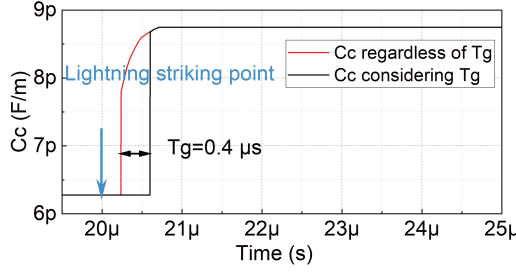In general, when an air gap is subjected to a fast-rising impulse voltage of sufficient amplitude, it takes a certain time to generate the first breakdown initiating electron before causing the collapse across the gap. It is called statistical time lag, t_g [129]. The statistical time lag for the corona onset in lightning case ranges from 0.4 μs to 0.8 μs [130]. Assuming t_g is 0.4 μs and the lightning striking moment in the PSCAD setting starts at 20 μs, the C for the cable down-lead with and without the t_g is shown in Fig. 4.14. When the lightning current is close to I_c, the corona sheath will fill the cross-arm immediately and the capacitance reaches its limited value. Therefore, the constant impedance $Z = \sqrt{L/C_{cor}}$ can be approximated for the cable down-lead modeling, and the velocity of propagation v should be recalculated correspondingly as $v = 1/\sqrt{LC_{cor}}$.

4.4.2 I_c and BFR

Considering the upper phase voltage impact, the lightning performances of the Y-shaped pylon with the cable as a down-lead inside the hollow cross-arm are obtained by EMT simulation. Taking the pylon with a 12 m length ground electrode as an example, in a power period, the I_{cphase} and the upper phase voltage against the upper phase angle are shown in Fig. 4.15. The arithmetic mean of I_{cphase} is represented by I_c due to the almost same value, and the lightning performances of the Y pylon with different ground rod lengths are shown in Table 4.2. Compared with the case that the cross-arm is filled with insulation materials, the I_c is slightly increased, indicating that the corona sheath inside the cross-arm induced by lightning has limited impact, which is similar to the effect of the filling materials discussed in Chapter 3. Although

4.4. Lightning Performance
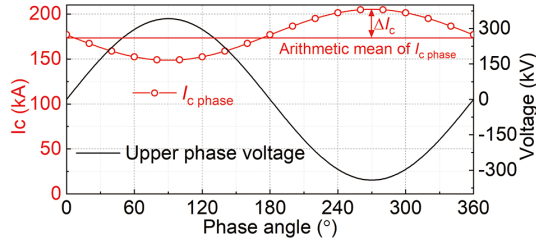
Fig. 4.15: The relationship between I_c and the upper phase voltage.
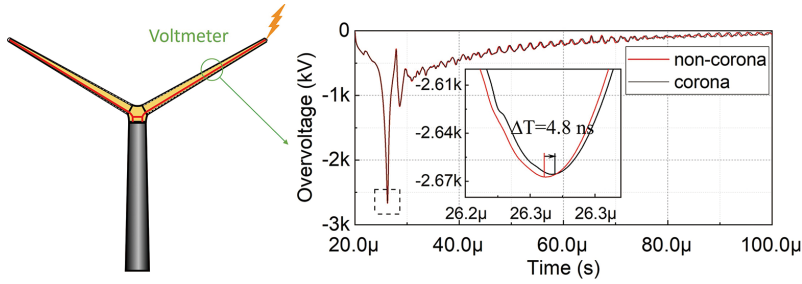
Fig. 4.16: The schematic of the voltmeter position, and the voltage waveform recorded in the middle of the cable down-lead.

the occurrence of a corona decreases the surge impedance, the corona slows down the lightning surge propagation velocity simultaneously. The corona sheath expands the equivalent radius of the down-lead and enhances the mutual coupling effect with the phase conductors and shield wires, resulting in about a 2 kA rise of I_c.

Table 4.2: Lightning performance of Y-shaped pylon with the cable as down-lead.

Lightning Current Waveform	Electrode Length	ΔI_c (kA)	I_c	BFR (flashes/100km-year)
CIGRE 3.83/77.5 μs	3 m	23.2	127.5	0.0300
	9 m	27.9	170.1	0.0038
	12 m	28.3	177.6	0.0027

The effect of the corona on the propagation of lightning surge can be revealed on the overvoltage waveform. With a lightning magnitude of I_c striking on the top of the pylon, the voltage waveform in the middle of the down-lead recorded by the voltmeter is shown in Fig. 4.16. The pylon model without the corona effect has been modeled for comparison. The simulation results clearly show that the corona effect pushes back the wavefront and decreases its steepness and crest value. With the lower propagation velocity, there is a slight time delay of about 4.8 ns.

4.5 Verification of cable insulation

During the operation of the composite pylon, the cable should have sufficient insulation strength to avoid puncture in lightning scenarios. Therefore, the insulation strength of the cable cover should be validated. As seen in Fig. 4.12, the corona only occurs at the rising edge of the voltage waveform. For the lightning voltage, the rising edge (T_f) is only several microseconds. Additionally, the corona in the gap between the cross-arm shell and cable cover belongs to the low-temperature plasma [131, 132]. Thus, the thermal effect of the corona in such extremely short duration on the dielectric strength is not considered.

4.5.1 Transient E-field Inside Cable

When the tower is struck by lightning, the phenomenon inside the cross-arm is divided into three stages. Figure 4.17(a) shows that stage 1 is from the striking moment to the occurrence of corona beneath the clamps, when the stroke current amplitude is I_c. For the cable with a radius of 4.35 cm, the corona inception E-field is 2.69 kV/mm according to the curve in Fig. 4.9, and the corresponding minimum voltage to trigger corona is attained to be 534.3 kV through the FEM simulation. At this moment, the E-field cloud chart of the cross-arm is shown in Fig. 4.18, illustrating that the intense electric field strength is primarily applied to the air gap and the maximum E-field magnitude inside the cable outer layer is about 1.69 kV/mm.
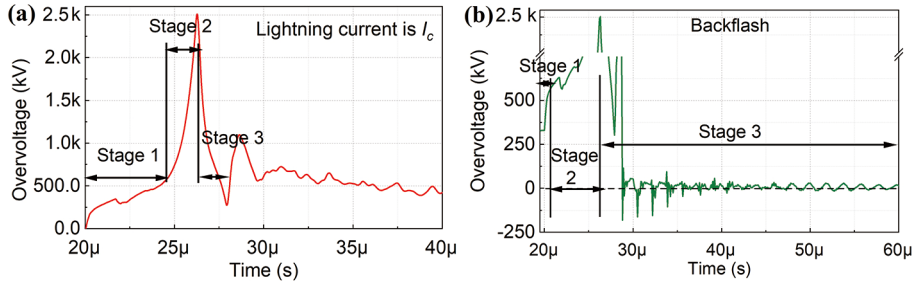
Fig. 4.17: The transient voltage waveform stressed between the cable down-lead and the upper phase conductor (a) when the lightning amplitude is I_c, and (b) when the backflash happens.

Stage 2 corresponds to the transient voltage rising from 534.3 kV to its crest. In this stage, the hollow cross-arm is filled with corona. When the discharge happened in the gap, numerous streamer discharges start from the cable surface randomly. When the streamer bridges the air gap, a large number of charges will accumulate on the inner surface and form a reverse electric field. Conversely, it extinguishes the discharge in the local area. As the voltage increases, this transient equilibrium will be broken and the process described before will continuously repeat.
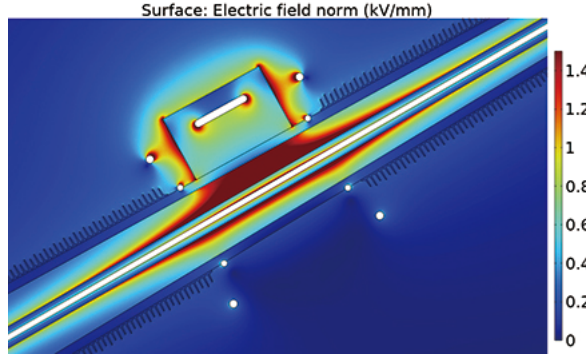
Fig. 4.18: The transient E-field cloud chart of the cross-arm before corona inception in lightning case. Source: **J3** [67].

When the lightning begins to fall, the gap in the cross-arm will go through stage 3. In this stage, the accumulated charge on the cross-arm inner surface decays along with the lightning voltage decreasing and keeps the internal field strength of the gap to zero. At this time, there is no filamentary discharge although the stressed voltage is higher than the corona inception voltage.

When the lightning stroke causes the backflash, the transient voltage waveform inside the cable is shown in Fig. 4.17(b). When the backflash happens, the phase-to-downlead overvoltage plunges and fluctuates since the cable and the upper phase voltage have the same potential. Before backflash moment, the transient voltage reaches its peak value of 2.51 MV, and the value is the same as in the case that lightning current is I_c without causing backflash in Fig. 4.17(a). Thus, in the two cases, the worst condition occurs at the transition point between stages 2 and 3, where the air gap E-field is zero and the maximum voltage stressed between the cable and phase conductor is about 2.51 MV. The E-field cloud chart at this moment is shown in Fig.4.19. It can be seen that the high electric field intensity area appears inside the cable H-GFRP layer with a maximum amplitude of 10.34 kV/mm, and the E-field distribution in the radial direction is slightly non-uniform.

4.5.2 Estimation of H-GFRP Insulation Strength

First, the lightning test with 1.2/50 μs bi-exponential impulse voltage is performed on the scale cross-arm with R_1=20 mm and r_1=16 mm. The lighting test system can detect the breakdown signal of the test object and display it in the interface. 'o.k' in the 'state' column denotes that no breakdown occurs on the test object (Fig. 4.20). The detection system shows that no puncture happens. As the inception voltage of this scaled cross-arm is 10.4 kV, the gap E-field can be treated as zero when the applied impulse voltage reaches its crest value of 65 kV. At this moment, the E-field distribution is shown in Fig. 4.21. The maximum E-field appears inside the small pipe with a value

of 20.49 kV/mm, which is higher than the required criterion.
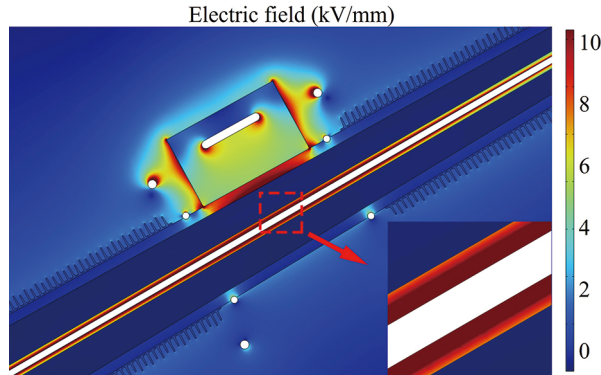
Fig. 4.19: The E-field cloud of the cross-arm with 2.51 MV is stressed as the gap E-field is zero. Source: **J3** [67].
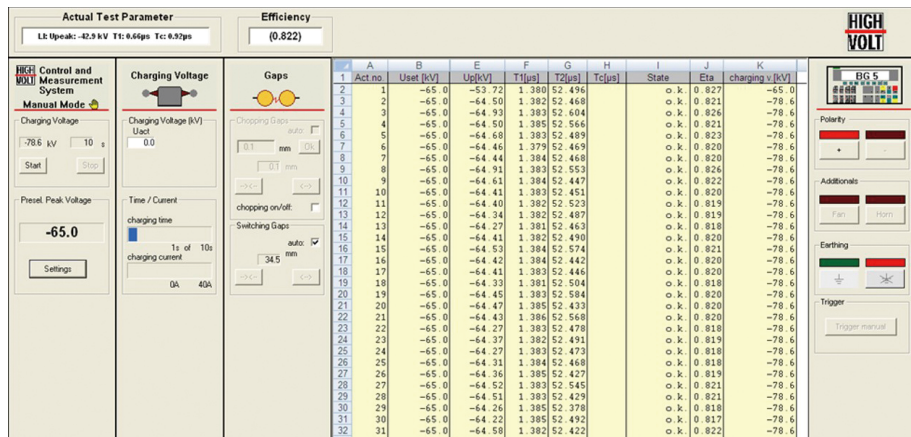
Fig. 4.20: The display window of the lightning test system. There are 30 times impulse tests on the H-GFRP cylinder.

The strength of the dielectric highly relates to the material thickness and electrode shape. To validate the insulation strength of the cable, the thickness effect of the cable layer should also be taken into consideration. The withstand E-field of the H-GFRP materials with a thickness of 2.6 cm should be tested under a quasi-uniform electric field. However, since the laboratory condition hardly can provide the breakdown test for such thickness materials, instead the H-GRFP withstand E-field using impulse voltage is evaluated by doing the breakdown test for H-GRFP cylinder with 2 mm thickness combined with a prediction based on the relationship between the breakdown E-field and the thickness.

The critical breakdown E-field of the H-GFRP pipe with a thickness of 2 mm under impulse voltage is tested. A 65 kV impulse voltage is performed on a single H-GFRP pipe (r_1 is 20 mm, r_2 is 18 mm), and the dielectric is exposed to a maximum E-field magnitude of 32.5 kV/mm (Fig. 4.22). A lightning test on the tube is repeated 30 times and the trigger detection system shows that no puncture happens, revealing that the withstand E-field of the H-GFRP cylinder with the thickness of 2 mm is at least 32.5 kV/mm.
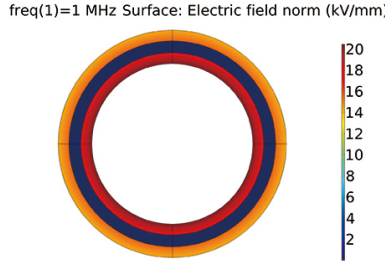
Fig. 4.21: The E-field cloud chart of the scaled cross-arm with 65 kV lightning voltage stressed on. Source: **J3** [67].
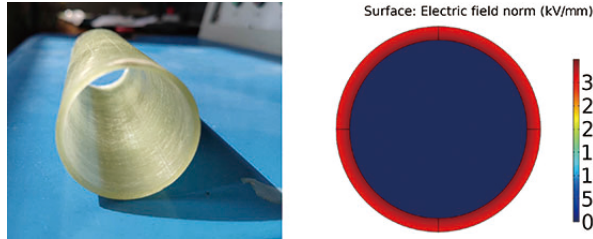
Fig. 4.22: The electric field distribution inside the H-GFRP pipe when it is performed lightning strength test.

Then we evaluate the breakdown strength of the H-GFRP with a thickness of 2.6 cm. For GFRP material, the breakdown E-field E_b with different thickness t_n obeys the following formula [107, 133]:

$$E_b = a t_n^b \tag{4.11}$$

Where a and b are coefficients. Referring to the measurements with the same electrodes (Fig. 4.23(a)) and test voltage waveform in reference [107, 134], a and b are 54.9 kV and -0.27 under impulse voltage. When the thickness of the H-GFRP changes from 2 mm to 2.6 cm, the breakdown E-field strength is about 22.78 kV, which is 50 % that of the value at a thickness of 2 mm (Fig. 4.23(b)). According to this trend, the breakdown strength of the H-GFRP in this research can be assessed to no less than 16.25 kV/mm at 2.6 cm thickness, which is higher than the maximum E-field strength

of 10.34 kV/mm of cable during lightning stroke obtained by simulation. That means the H-GFRP material is a promising material and has adequate insulation margin as the insulation layer for the cable down-lead.

(a)

FRP (G-10) tube   Silver paint electrodes

Breakdown path

Silver paint electrodes

HV

(b)

E. Tuncer et. al.
IEEE T. Appl. Supercon. 2007, 17(2): 1513-1516.

— Eb-thickness curve
○ Fitting data

[2 mm, 45.53 kV]

a=54.9 kV   b=-0.27

[26 mm, 22.78 kV]

Eb (kV/mm)
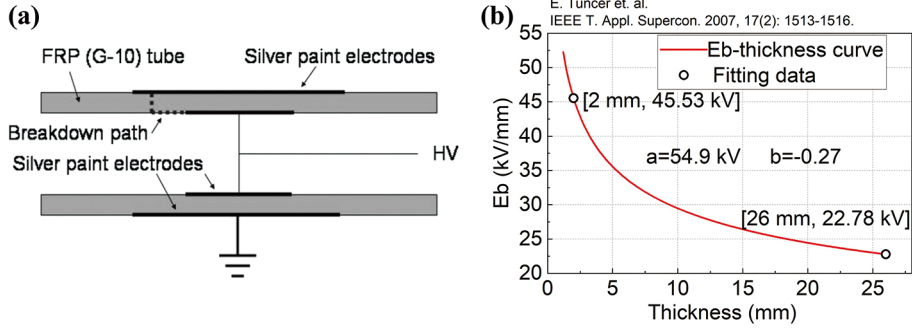
Thickness (mm)

Fig. 4.23: (a) The electrode arrangement for H-GFRP (G-10) tube and breakdown path [134]. (b) The GFRP breakdown E-field magnitude versus the thickness under slightly uneven electric field distribution using impulse voltage [107].

4.6 Summary

In this chapter, the feasibility of the cable as a down-lead for a Y-shaped composite pylon has been investigated from the perspectives of electrical insulation and lightning protection performance. The corona onset E-field on the H-GFRP surface as the function of cable radius is studied with 50 Hz AC voltage applied and the expression is given based on Peek's formulas for coaxial cylinder structure. A cable with a core radius of 1.75 cm and an insulation thickness of above 2.47 cm is determined as the down-lead, with which there is no corona inside the cross-arm under steady-state operation. Considering the switching overvoltage condition (2 p.u.), the corona power consumption as a function of the E-field is studied, and the results show that the power loss would not increase sharply with the E-field less than 4.4 kV/mm. Based on this, the cable down-lead radius is reset to 4.35 cm. After the cable parameter determination, the lightning performance of the pylon with the cable as down-lead is analyzed by PSCAD/EMTDC. I_c values with different phase voltages are obtained, and BFR is calculated to be 0.0027 flashes/100 km a year for the pylon with a 12 m ground rod. Meanwhile, there is a slight time delay and a crest value decrease observed in the transient voltage of the cable due to the impulse corona. Finally, the cable insulation strength has been investigated when the backflash happens. The maximum E-field magnitude inside the cable is 10.34 kV/mm, which is lower than the estimated withstand value of 16.25 kV/mm of the H-GFRP with 2.6 cm thickness. Therefore, the cable down-lead meets the insulation requirements. In summary, the cable with appropriate parameters as down-lead inside the hollow cross-arm is a feasible strategy for the composite tower.

Chapter 5

Formula Expression of Lightning Performance

In high voltage engineering, empirical formulas are commonly used for the assessment of the lightning performance of transmission towers. In this way, the I_c or BFR for towers can be obtained by simple calculation even hand calculation without the resort to the simulation software [82], and the cumbersome modeling process is saved. The fast calculation based on these formulas plays an important role in the tower screening, precheck of some solutions, and verifying behavior in some special terrain.

As discussed in the Introduction, the demand for new transmission lines has brought various forms of transmission towers. The integration of cross-arm and insulator and bifurcation framework have become a trend in the design of towers such as the Y-shaped tower in this Ph.D. research. Aiming at the bifurcation configuration, it is necessary to propose new formulas to evaluate the lighting performance. In this chapter, some traditional formulas for the expression of the critical current of transmission steel towers have been reviewed. Then, new empirical formulas based on the lattice diagram method have been proposed to assess the lightning performance of the tower with a bifurcation framework. Furthermore, the formulas are improved to extend their application scope and are compatible with conventional lattice towers.

Of particular concern is that in the previous chapter, two down-lead schemes that solid cross-arm with a conductor passing through and a hollow cross-arm with cable inside are discussed. In fact, the I_c under the two down-lead schemes are very close and the maximum difference is no more than 1 %. Thus, the critical current of the Y composite pylon can be formulized based on either one ground mode. Here, the down-lead passing through a cross-arm filled with FRP is chosen to deduce the empirical formulas.

5.1 Existing Empirical Formulas

To date, there are two most commonly used empirical methods for the estimation of lightning performance. Lumped parameter method [135] and lattice diagram method based on distribution parameters of circuit [63, 136]. Aiming at traditional steel frame towers, they tend to show a good prediction regarding the lightning response.

5.1.1 Lumped Parameter Method

Lumped parameter method is recommended by the State Grid of China and is based on the component equivalent of lumped parameters. This method considers the coupling between paralleled conductors, and the height of the phase wire (h_s). Normally, it is recommended to apply for a tower height lower than 40 m [137]. When the lightning strikes at the top of the tower, the tower top potential U_{top} is

$$U_{top} = \gamma I \left(R_{\mathrm{i}} + \frac{L}{T_f} \right) \tag{5.1}$$

At the same time, the induced potential of the phase conductor (U_c) is

$$U_c = k_c U_{\mathrm{top}} - Ih_c(1 - k_c)/T_f \tag{5.2}$$

Then, the critical current I_c of a tower can be determined by equation (5.3) [138].

$$I_c = \frac{U_L}{(1 - k_c)(\gamma R_i + \gamma L/T_f + h_s/T_f)} \tag{5.3}$$

Where k_c is the coupling coefficient between the shield wire and upper phase conductor. L is the total inductance of the lattice tower. For a Y-shaped pylon, $L = L_c + L_t$. Where L_c and L_t are the inductances of the down-lead inside the cross-arm and the pylon mast. The ratio of the lightning current flowing the tower-footing impedance (i_R) to the stroke current (I) is defined as the shunt coefficient γ [137].

However, the precision of this method highly depends on the shunt coefficient, which is varied from the lightning waveform, footing resistance, tower configuration, the pylon distance, and the number of shield wires. For traditional towers with different voltage levels, the determination of this parameter is based on operating experience. For a Y-shaped pylon, the γ at varied T_f and R_0 is explored through EMT simulation with the current dependence ground model adopted [82]. It can be found that this coefficient is highly susceptible to these two factors as depicted in Fig. 5.1. For new towers, especially those in the concept stage, it is difficult to get accurate γ in different scenarios. Thus, this method is only restricted to towers under specific conditions.
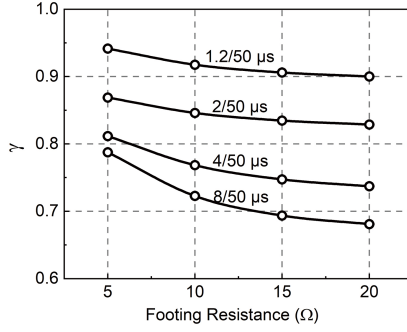
Fig. 5.1: The γ obtained by EMT simulation for Y-shaped pylon with different R_0 and T_f. Source: **C3** [82].

5.1.2 Lattice Diagram Method

The lattice diagram method is a distributed parameter method suggested by CI-GRE TB 839 and considers the wave traveling process along one pole between the shield wire and ground impedance. This method assumes that there is no reflection at the conjunction point of the shield wire and tower body and only discontinuity at the ground position considered [51]. In addition, the lightning waveform is substituted by a triangle front (T_f) and a constant tail. The critical current I_c is written by

$$I_c = V_{TT}/K_{TT}K_{SP} \tag{5.4}$$

V_{TT} is the voltage on the shield wire when lightning strikes the tower, which is equal to the sum of U_L and induced voltage on the conductor U_c.

$$U_c = kV_{TT} - h_c(1 - k_c)I_c/T_f \tag{5.5}$$

Where h_c is the height of the upper phase conductor. K_{TT} and K_{SP} are

$$K_{TT} = R_e + \frac{Z_g - 2R_i}{Z_g + 2R_i}\frac{L}{T_f} \tag{5.6}$$

$$R_e = \frac{R_i Z_g}{Z_g + 2R_i} \tag{5.7}$$

$$K_{SP} = 1 + \alpha_R(1 + \alpha_T)\left[(1 - \frac{2T_s}{T_f}) - \alpha_R\alpha_T(1 - \frac{4T_s}{T_f}) - \cdots\right] \tag{5.8}$$

The ground potential rise (GPR) is

$$GPR = V_{TT}R_e/K_{TT} \tag{5.9}$$

Where L is the inductance of the down-lead or lattice tower, and T_s is the travel time on the span. α_T is the reflection coefficient at the point of tower footing impedance

and pylon body, and α_R is the reflection coefficient at the point of transmission line and adjacent towers.

Compared with the aforementioned two methods, this method is suitable for any tower height and a full range of T_f. The derivation process is based on the actual surge traveling, which produces results closer to the practice values even with simple forms. Thus, this method is widely used for overvoltage analysis and lightning performance assessment [51, 63].

5.2 Novel Empirical Formulas

For the two methods, the special configuration of the 'Y' tower has never been considered in all methods, and whether these empirical methods can apply to new types of pylons with acceptable errors is still unclear. Furthermore, for some special scenarios, such as return stroke, existing empirical formulas are unable to precisely describe the overvoltage and ground potential rise. There is a lack of research concerning updating these methods over the years. Thus, it is necessary to improve and propose new empirical formulas to accomplish fast estimation for the novel composite pylon.

5.2.1 Simplification of Pylon Model

Although the simulation results are of high accuracy, too many components and electromagnetic phenomena are not conducive to formula expression and fast assessment. The formula expression should be as simple as possible on the premise of acceptable accuracy. Here, the influence of the modeling modes mentioned in Chapter 2 and Chapter 3 on the precision of the lightning transient performance is discussed, and then ignoring the factors with low influence degree. In this section, the influence degree of the coupling effect and parasitic capacitance are discussed. Based on the complete EMT model for the pylon in Chapter 3, the modules of coupling, and parasitic capacitance in PSCAD are removed step by step. Compared the simplified model results with the complete model results, the impact of these simplifications on accuracy is evaluated. Finally, we will obtain a simplified down-lead model for deriving empirical formulas.

A. Coupling Effect and Parasitic Capacitance Simplification

The mutual coupling effect and the parasitic capacitances are removed from the equivalent circuit separately. The recorded voltage on the connection point of shield wire and down-lead with first and subsequent strokes are shown in Fig. 5.2. Without coupling and parasitic capacitance, the overvoltage amplitude increases slightly by 4.2 %, and the waveforms are almost coincident. It can be concluded that the coupling effect and the capacitances between the phase conductors and down-lead are not significant. The reason for weak coupling is that the space angle between the two down-lead

is 120°, and the magnetic flux derived from one down-lead through another one is limited. Besides, the maximum coupling distance between them is more than 20 m. For the parasitic capacitances, though their values are much higher than that of steel lattice towers, they are still too small (tens of pF) to impact the overvoltage.
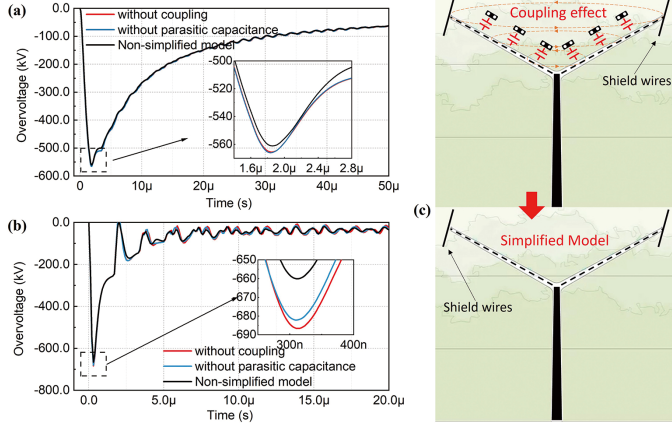
Fig. 5.2: The overvoltage waveform on the top of the pylon with (a) the first stroke and (b) subsequent stroke when coupling effect and parasitic capacitance is no longer considered. (c) The schematic of the simplified pylon model without coupling effect and parasitic capacitance.

B. Down-lead Simplification

For a single down-lead modeling, there are considered four short transmission lines and each connection point is a discontinuity. The complicated lightning surge traveling process is almost impossible for hand calculation. However, the surge impedance variation of each segment is limited, and the formula expression of the model can be realized by reducing the number of segments. Figure 5.3 depicts the overvoltage waveform on the top of the towers with time. As the number of the down-lead segments decreases, the overvoltage amplitude decreases gradually. The maximum error of the crest voltage of one segment is about 1.52 % compared with four segments. The error derived from a simplification of the down-lead can cause a decrease in the transient voltage, which offsets the errors of removal of coupling and parasitic capacitance, leading to a limited net error. Therefore, the surge impedance Z_c of the Y pylon down-lead can be represented by

$$Z_c = 60 \ln \left(2h/r \right) \tag{5.10}$$
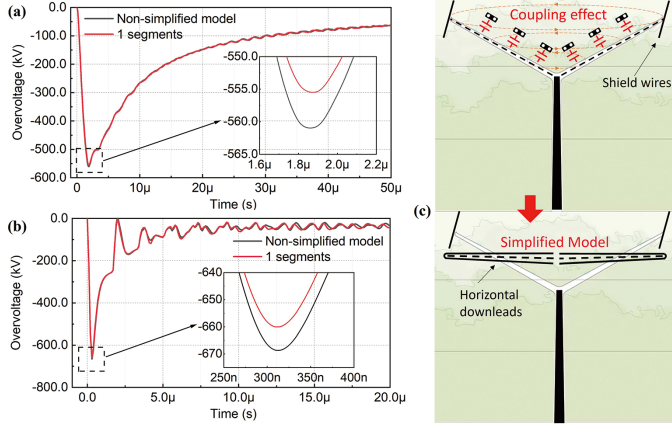
Fig. 5.3: The overvoltage conditions at the top of the pylon with (a) first and (b) subsequent striking when the down-leads are modeled as different segments. (c) The schematic of the simplified pylon model with horizontal cross-arm.

C. Simplified Equivalent Circuit

At this time, the simplified down-lead model is determined, which is composed of two horizontal down-leads connecting with the steel mast as shown in Fig. 5.4(a). Taking the shield wires and ground impedance into consideration, the equivalent circuit of the pylon is depicted in Fig. 5.4(b). Based on the equivalent circuit, the empirical formulas for evaluating the transient response to lightning striking are deduced in the following part.
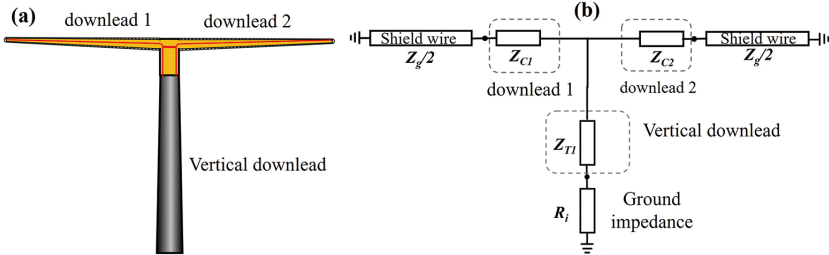
Fig. 5.4: (a) The schematic of the simplified pylon. (b) The equivalent circuit of the down-lead system of the Y-shaped pylon. Where Z_g is the surge impedance of shield wires, and Z_{T1} is the surge impedance of the mast.

5.2.2 Empirical Formula Derivation

The newly proposed method is also based on the lattice diagram method, and the specific bifurcation configuration is considered in the inference process. The Y structure means the multi-discontinuities are introduced in the equivalent circuit, leading to

a complex surge traveling. To facilitate the formula expression, here are four assumptions suggested.

(1) The effect of the reflection from adjacent towers is neglected.

(2) Setting the ground impulse impedance R_i to a constant value. The value can be given as (2.31).

(3) The down-lead inside the cross-arm is treated as a horizontal part, taking its geometric center position as the height. The H-GFRP composite material is neglected, and its surge impedance is $Z_c = 60\ln(2h/r)$. The lattice diagram for the surge traveling process of a Y-shaped pylon is illustrated in Fig. 5.5.
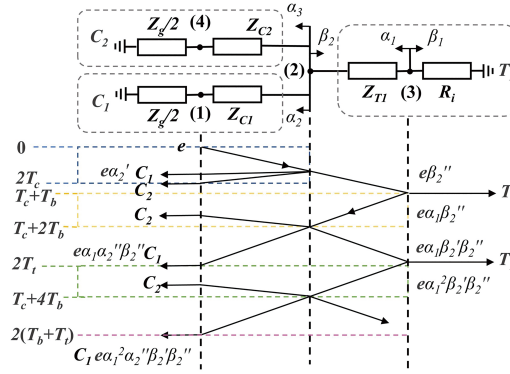
Fig. 5.5: The lattice diagram for the surge traveling of the Y-shaped pylon. Discontinuity points (1) and (4) are the connection points of shield wires and down-leads, (2) is the joint of the pylon, and (3) is the connection point between the mast and the soil. C_1 and C_2 are the cross-arms, and T_1 is the pylon body. Source: **J2** [80].

(4) We follow the assumptions of the previous empirical formula: $Z_g = 2 \times Z_{C1}$ [51]. Z_{C1} is the surge impedance of the down-lead inside the cross-arm. At this time, $e = Z_g \times I/4$, and the surge reflection and refraction at (1) and (4) are ignored.

The reflection α and refraction coefficient β are then determined. When the lighting current flows point (2) from the cross-arm side to the pylon body side, the reflection coefficient is defined as α_2', and α_2'' for the refraction coefficient. While the current flows through the point (2) from the mast side to the cross-arm side, the reflection coefficient is defined as β_2', and β_2'' for the refraction coefficient [80].

$$\alpha_2' = \frac{Z_{k2} - Z_{C1}}{Z_{k2} + Z_{C1}} \tag{5.11}$$

$$\beta_2' = \frac{Z_{k1} - Z_{T1}}{Z_{k1} + Z_{T1}} \tag{5.12}$$

$$\alpha_2'' = \frac{2Z_{k1}}{Z_{k1} + Z_{k2}} \tag{5.13}$$

$$\beta_2'' = \frac{2Z_{k2}}{Z_{k2} + Z_{T1}} \tag{5.14}$$

This case is a two-outgoing line system. We found that the cross-arm C_2 has no impact on the overvoltage on the C_1 in this circuit. If the branch of C_1 is not considered. The lattice process can be further simplified and generalized for traditional tower cases as Fig. 5.6 shows. Where Z_{k1} and Z_{k2} are given in Table 5.1.
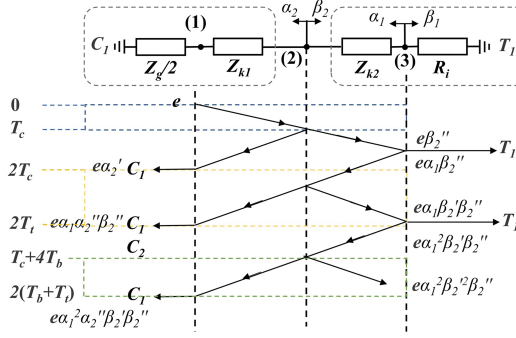
Fig. 5.6: The lattice diagram applied for both Y-shaped pylon and traditional towers. Source: **J2** [80].

Table 5.1: Tower component surge impedance.

Parameter	Y pylon	Steel towers
Z_{k1}	$Z_{C1}/2$	Z_{C1}
Z_{k2}	$Z_{C1}Z_{T1}/(Z_{C1}+Z_{T1})$	Z_{T1}

It should be noted that Z_{C1} for the traditional tower is the surge impedance of the metal cross-arm supporting the shield wires. The crest tower top voltage is [80]:

$$V_{TT} = Z_g K_{TT} I_c / 4 \tag{5.15}$$

$$K_{TT} = 1 + \alpha_2' \left(1 - \frac{2T_c}{T_f}\right) + \sum_{n=3}^{\infty} \alpha_2''^{n-2}\alpha_2''\beta_2''^{n-3}\beta_2'' \left\{1 - \frac{2\left[T_t + (n-3)T_b\right]}{T_f}\right\} \tag{5.16}$$

Where T_t, T_c, and T_b are travel time from top to bottom, traveling time in the cross-arm, and time in the pylon body, respectively. The ground potential voltage is given by [80]:

$$GPR = Z_g G_{TT} I_c / 4 \tag{5.17}$$

$$G_{TT} = \sum_{n=1}^{\infty} \alpha_1^{n-1}\beta_2'^{n-1}\beta_2''(1 + \alpha_1)\left[1 - \frac{2(n-1)T_b}{T_f}\right] \tag{5.18}$$

Where n is the number of the voltage on the cross-arm in the process of surge traveling. As K_{TT} and G_{TT} are infinite coefficients, they cannot be fully expressed by empirical formulas. Thus, (5.16) and (5.18) should be replaced by finite expressions. The real values and absolute values of the individual components of K_{TT} and G_{TT} are shown in Fig. 5.7 and Fig. 5.8. It can be seen that the absolute values of the K_{TT} parts exhibit an attenuation trend. The sum of the first n parts is also shown in Fig. 5.7(b). As we can see, when the $n \geq 4$, the value of K_{TT} reaches a constant status for all three kinds of towers. Thus, the attenuation trend mainly depends on the equivalent circuit and it will not be affected by the coefficients in the formulas. The same is true with the case of ground potential rise (Fig. 5.8). Thus, the first four terms are given as the expressions of K_{TT} and G_{TT}.
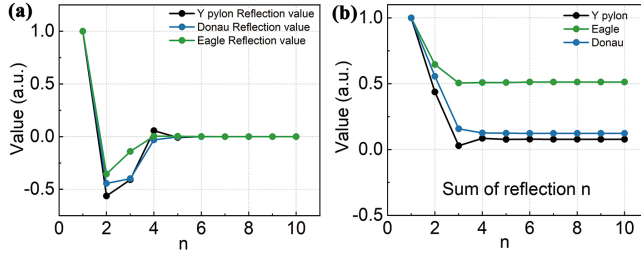
Fig. 5.7: (a) The real and absolute value of parts in K_{TT}. (b) The sum of the first n parts in K_{TT}. Source: **J2** [80].
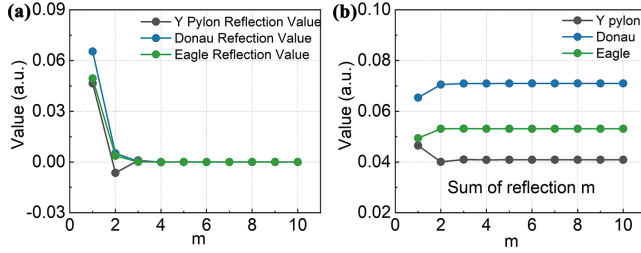
Fig. 5.8: (a) The real and absolute value of parts in G_{TT}. (b) The sum of the first n parts in G_{TT}.

5.3 Comparison of Two Lattice Diagram Methods

In this section, the lightning performances of the Y-shaped pylon, as well as traditional Donau and Eagle towers by simulation and empirical formulas, are compared. The EMT simulations of three towers are performed under the frequency-dependence ground model and taking the results as the reference, U_L and GPR results are obtained by simulation and calculation with the first and subsequent strokes terminating on the top of towers (Fig. 5.9). For the first stroke, new and original methods show similar

predictions. However, there are large differences in results between the two methods for subsequent lightning striking. The new method shows lower errors compared with the original one. That means the new method is more accurate when the T_f is extremely short.
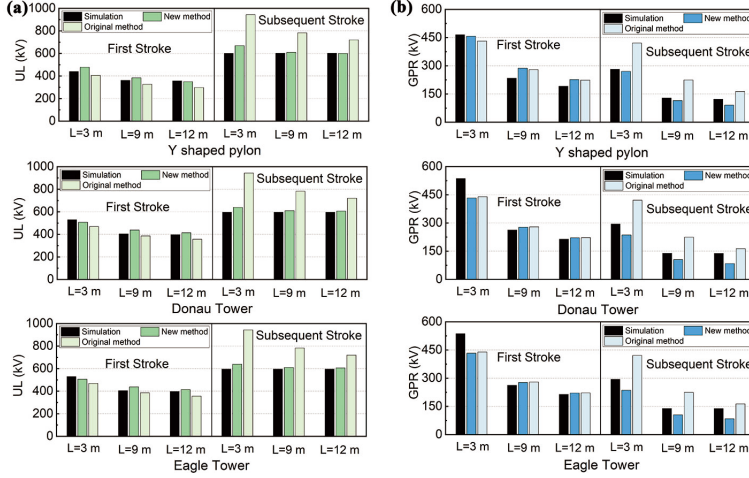
Fig. 5.9: The comparison of GPR and U_L Y-shaped pylon, Donau, and Eagle towers obtained by PSCAD simulation, original method, and New method at first and subsequent strokes.

We also perform a comparative study on the two kinds of methods to obtain the critical current (I_c) with a full range of T_f. According to the lognormal distribution, when T_f exceeds 12 μs, the cumulative backflash probability is calculated to be less than 1×10^{-6}, which can be neglected. Thus, I_c values corresponding to T_f in the range of 0.1-12 μs have been investigated. The I_c against T_f curves of three kinds of towers with electrode lengths of 3 m, 9 m, and 12 m are illustrated in Fig. 5.10(a)-(c).

The calculation results from the new method fit well with the simulation results. It is noteworthy that the error becomes larger when the T_f is very short or long. However, the probability of lightning front time appearing in this interval is very low. Thus, we introduce the concept of the confidence lattice interval. For example, 95% confidence interval means the 95% probability of lightning with T_f in this range. Taking the I_c obtained by EMT simulation as the standard reference, the calculation errors of the newly proposed method and CIGRE method are calculated. Then, averaging the errors of I_c at different T_f, the mean errors corresponding to different confidence intervals are listed in Table 5.2. It can be seen that the new method can evaluate the I_c of both composite and steel towers accurately. The maximum errors for Y-shaped pylon and steel towers are 9.49 % and 12.75 % in a 97.5 % confidence interval. However, for the Y-shaped pylon, the estimation errors of the original CIGRE method are quite larger than that of the new method. The new method has higher precision and wider application scope in the prediction of lightning performance. Additionally, there is
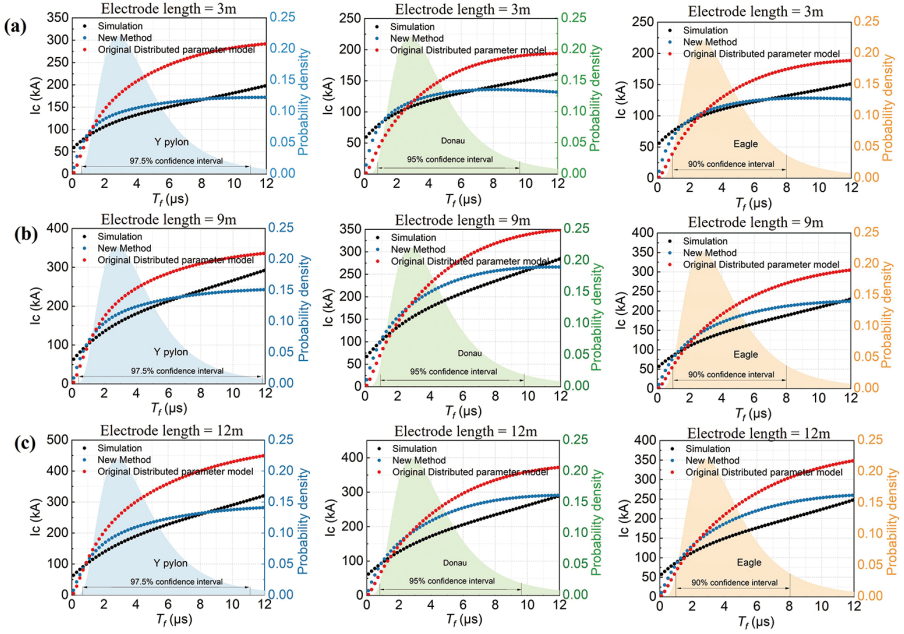
Fig. 5.10: The simulation, new and original method results for Y-shaped pylon, Donau, and Eagle towers with the T_f range 0.1-12 μs with the tower electrode length of (a) 3 m, (b) 9 m, and (c) 12 m, respectively.

another advantage of the new method that it has high accuracy with the T_f in the range of 1-6 μs, in which the lightning is most likely to occur. It verifies that it would be highly advantageous for the new method applied to the Y-shaped and conventional lattice towers.

Table 5.2: Calculation errors under different T_f confidence intervals (%)

Confidence Interval	T_{f1} (μs)	T_{f2} (μs)	Electrode Length	New method Y	New method Donau	New method Eagle	Original method Y	Original method Donau	Original method Eagle
97.5 %	0.70	11.4	3 m	7.99	6.08	5.22	52.14	23.64	25.42
			9 m	8.45	11.63	12.75	28.13	28.81	34.75
			12 m	9.49	10.28	10.64	50.07	25.63	31.72
95 %	0.83	9.65	3 m	7.99	4.66	3.81	52.24	23.02	24.36
			9 m	7.64	13.61	14.53	29.69	28.72	33.95
			12 m	9.95	11.56	12.12	51.32	26.10	30.97
90 %	1	7.97	3 m	9.52	4.20	3.03	51.73	21.01	21.96
			9 m	8.02	15.52	15.61	30.96	27.46	31.85
			12 m	12.12	13.23	12.72	52.63	25.18	28.91

Furthermore, the BFR values at the full range of T_f of the new and original lattice

methods are calculated and listed in Table 5.3. First, T_f in the range of 0-12 μs is discretized to $n = 120$ points, and increment ΔT is 0.1 μs. Then, the probability of occurrence of lightning with different T_f should be determined. According to (2.8), the corresponding probability of each T_f is $f(T_f)\Delta T$. Finally, the total BFR considering the T_f range can be obtained by

$$BFR=0.6N_L \sum_{i=1}^{n} \left\{ [f(T_f)\Delta T] [1 - P_c(I_c(T_f))] \right\} \tag{5.19}$$

We also employ the EMT model combined with the Monte Carlo procedure to obtain the BFR [139, 140]. Retaining the previous EMT model and flashover judgment described in Chapter 2, 10 thousand sets of lightning currents are randomly generated whose T_f and I_c accord with the statistical distribution in (2.8). Then, this series of data are input into the PSCAD model, and the flashover and non-flashover results can be plotted in Fig. 5.11(a)-(c) for three towers with different ground rods.
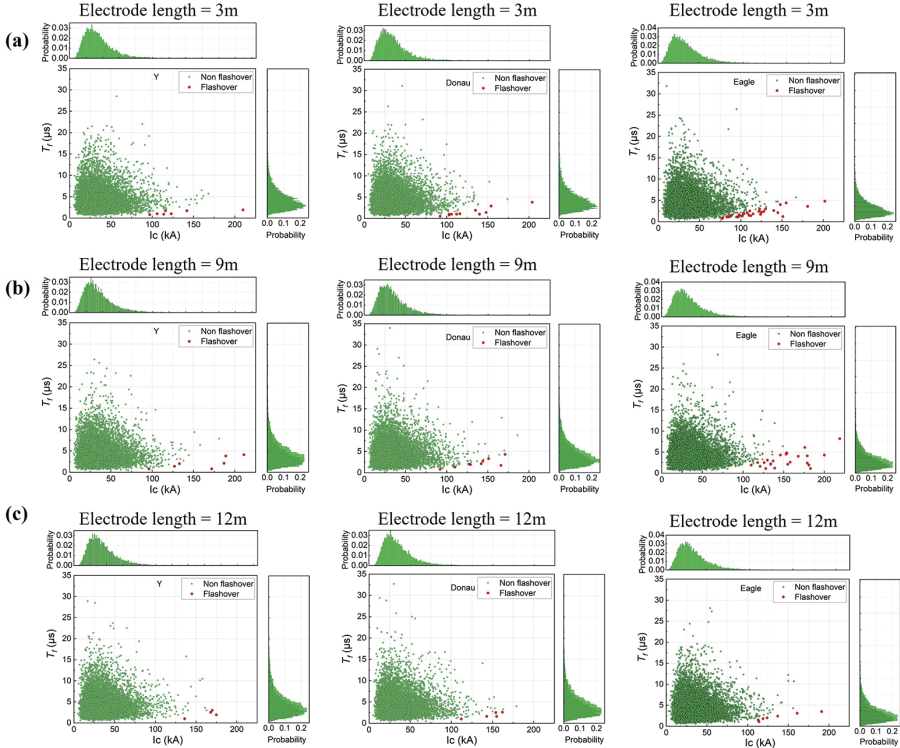
Fig. 5.11: The statistics of flashover caused by 10000 set random lighting currents for Y-shaped pylon, Donau, and Eagle towers with the tower electrode length of (a) 3 m, (b) 9 m, and (c) 12 m, respectively.

The BFR results from the simulation using the Monte Carlo procedure are given in Table 5.3. Taking the simulation results using the Monte Carlo procedure as the stan-

dard reference, the BFR obtained by the new method is closer to the simulation values when compared with the original method, especially for three kinds of towers adopted with the ground rod of 3 m. In comparison with the error shown in Table 5.2, both two methods show relatively large errors, which can be attributed to the randomness of the generated lightning data.

Table 5.3: Calculation of BFR (flash/100 km per year)

Length of electrodes	Tower	Original method	New method	Monte Carlo method
3 m		0.0128	0.0510	0.0379
9 m	Y	0.0058	0.0062	0.0084
12 m		0.0025	0.0033	0.0070
3 m		0.1890	0.0711	0.0903
9 m	Donau	0.0353	0.0108	0.0202
12 m		0.0234	0.0082	0.0166
3 m		0.2950	0.1374	0.1407
9 m	Eagle	0.0660	0.0288	0.0446
12 m		0.0531	0.0242	0.0369

5.4   Summary

This chapter presents the new empirical formulas for lightning performance of composite and steel towers. The configuration of two horizontal cross-arms connected with the vertical mast is formulated in the deviation process. The new method is derived from the lattice diagram method, and it is converted to common forms which are applicable to both Y-shaped pylons and lattice towers. Compared with the original empirical formulas recommended by CIGRE, the new method has higher calculation accuracy in the estimation of I_c, GPR, and U_L, especially with the subsequent lightning striking. Furthermore, we also investigate the two methods' accuracy at a full range of T_f. With the T_f range from 0.7 to 11.4 μs (97.5% confidence interval), the new method applied on a Y-shaped pylon with a maximum error of no more than 12.75 %, compared with that of 52.14 % from the traditional method. Finally, the comparison of BFR results get from the empirical formulas and the Monta Carlo procedure is performed. The results of the new method are closer to those of the Monte Carlo algorithm at different ground conditions, which verifies the high accuracy of this new method.

Chapter 6

Conclusions

This chapter summarizes the outcomes of the Ph.D. project - *Design of an Internal Down-Lead System for a 400 kV Composite Tower and Investigation of Lightning Performance*. The main contributions are highlighted, and the research perspectives are discussed at the end of this chapter.

6.1   Summary

In *Chapter 1*, the state of the art of composite pylon and its lightning performance have been discussed in four aspects, i.e., (1) development, structure, and application of composite towers in recent decades, (2) manufacturing and material selection for components of the composite tower, (3) down-lead mode of the existing composite tower, and (4) lightning protection performance of composite towers. As seen from the discussion, the composite towers are quite different from traditional towers, and the design of down-lead of Y-shaped composite pylon studied in this project is absent and there is little research regarding the assessment of its backflash rate. It is necessary to determine the ground mode for the composite pylon and carry out systematic research on the lightning performance. Accordingly, research objectives have been outlined:

(1) Building EMT model in PSCAD/EMTDC for a Y-shaped composite pylon, and getting the I_c and BFR of the pylon with two separated down-leads through pylon cross-arm and body;

(2) Optimizing the down-lead system and pylon configuration to improve its lightning performance;

(3) Discussion of the feasibility of a cable as down-lead for the composite tower;

(4) Proposing empirical formulas for fast assessment of lightning performance for the composite pylon in practical engineering.

In *Chapter 2*, the integral formulas for the oblique down-lead impedance are proposed and verified by simulation. The modeling of the down-lead system of the Y-shaped pylon has been established considering the impact of the mutual coupling ef-

fect between two down-leads and parasitic capacitances. In addition, the modeling for 400 kV traditional steel Donau and Eagle towers is also presented. The comparison results concerning I_c and BFR indicate that the lightning performance of a Y-shaped pylon with two separated down-lead is inferior to these steel towers. It is necessary to optimize the composite pylon down-lead system to obtain higher I_c.

In *Chapter 3*, the down-lead system is optimized and filling materials for cross-arm are selected. Without modifying the pylon body structure, various factors that may affect I_c are studied. For down-leads above the pylon joint, the radius and dielectric properties of filling materials change the surge impedance, lightning conducting speed, and parasitic capacitances simultaneously, but the net effect is zero. In addition, the down-lead part below the joint, namely mast, is replaced by a steel column, which is an effective way to increase I_c. After determining the down-lead system, the H-GFRP is chosen to fill the cross-arms. The down-lead ampacity and local flashover probability on the steel mast are evaluated and there is adequate insulation strength to guarantee the safe operation of the composite pylon. By doing so, the lightning performance of the optimized pylon is largely increased, which is better than that of 400 kV Donau and Eagle pylons.

In *Chapter 4*, aiming at lightweight and easily assemble, the feasibility of cable as a down-lead is explored. The scaled model for the cross-arm is built and used for experiments. Combined with EMT and FEM simulation, the corona onset threshold, and corona power loss are studied, which provide the basis for the design of the cable parameters. With cable through the cross-arm, the I_c is slightly increased compared with the scenario in the cross-arm filled with FRP. Meanwhile, the probability of cable puncture is also investigated by FEM simulation, the results indicate that there is adequate insulation margin to avoid puncture happens.

Finally, in *Chapter 5*, two existing empirical expressions for estimation of the transmission towers are reviewed and the accuracy of their application for a Y composite pylon is discussed. Through the simplification of the tower modeling, new empirical formulas are presented based on the lattice diagram method. This improved method takes the 'Y' pattern of the down-lead system into consideration and can be extended to traditional steel towers. Compared with the lattice diagram method proposed in the CIGRE brochure, the new method exhibits higher precision. The Monte Carlo procedure is employed to verify its superiority.

In summary, the ground method that the internal down-lead system for the Y-shaped composite pylon is proven to be applicable in this Ph.D. research. In order to improve the lightning performance, the steel column is adopted as the pylon mast. To strengthen the mechanical stability and make the assembly easier, the cable is competent as the down-lead going through the hollow cross-arm. In addition, empirical formulas are proposed to estimate the critical current of the composite pylon. The Ph.D. research provides design ideas and optimization schemes of the down-lead for composite towers, which will be of great importance for the development and application of composite towers.

6.2   Main Contributions

Based on the research outcomes of this Ph.D. project, the main contributions are summarized as follows:

A. EMT modeling for 'Y' shape pylon to evaluate the down-lead system

- The down-lead system of the 'Y' shape pylon has a different configuration compared with traditional steel towers. For inclined down-lead, there are no existing empirical formulas to calculate its surge impedance. Here, integral form formulas are proposed and validated by FEM simulation;

- The Y-shaped pylon has two separated down-leads inside the cross-arm. The mutual coupling effect between the two down-leads is established. Meanwhile, the parasitic capacitances between the phase conductor and the down-leads are considered. Based on that, the critical current of the composite pylon with the initial design of the down-lead system is simulated, and the BFR results of the Y-shaped pylon are higher than that of traditional steel towers. The down-lead system should be improved to enhance the pylon lightning performance.

B. Optimization scheme of down-lead

- To improve the lightning performance of the composite pylon, multiple potential factors affecting lightning protection performance have been evaluated, especially the effect of the filling materials for cross-arm. The permittivity of the filling material and the cross-arm radius can affect the surge impedance as well as the lightning conducting velocity along the down-lead simultaneously, but the net effect is insignificant. Thus, in the design of the cross-arm, the dimensions and permittivity of the filling material will not affect the lightning protection performance;

- For the down-lead inside the pylon mast, the lightning performance is gradually improved from two separate vertical down-leads to multi-conductors to a steel column. Steel mast replacing the down-lead conductors is the optimal form of the grounding mode.

C. The feasibility of the cable as the down-lead is proved

- In the design of the cable parameters, without changing the cable core radius, the surface potential can be reduced by adjusting the thickness of the cable insulation layer. By the means of FEM simulation combined with a partial discharge measurement on a scaled cross-arm model, the minimum thickness of the cable layer is determined;

- The corona power loss on the surface of the cable with transient switching overvoltage has been studied. Due to the surface charge accumulation and extremely short duration of discharge, the corona power is very low at the beginning, then

sharply increases along with the applied voltage increasing. Based on this special phenomenon, the cable parameters are reset to ensure the sufficient insulation margin;

- Considering the corona sheath inside the hollow cross-arm, the I_c of the pylon with cable as down-lead is simulated. Meanwhile, the E-field strength stressed on the cable during the whole process of being struck by lightning is analyzed and the cable insulation strength is verified.

D. Proposing empirical formulas for I_c with higher accuracy

- The new empirical formulas are derived based on the lattice diagram method and assumptions proposed in the CIGRE brochure. Compared with the original CIGRE method, the new expression considers the influence of the 'Y' pattern of the down-lead on the surge traveling process, which improves the calculation accuracy;

- In order to simplify the expression, tower components have been simplified to different degrees. Making use of the characteristics that different simplification effects offset each other, the high accuracy is retained even with simplified formulas;

- These formulas for the Y-shaped pylon can be extended to traditional towers with higher accuracy compared with the original lattice diagram method.

6.3 Research Perspectives

The entire Ph.D. work demonstrates the design, optimization, and validation for the down-lead system of the Y-shaped transmission pylon, and proposes highly accurate formulas to assess the critical current of the composite pylon. To improve the application of the Y-shaped composite pylon, some extended work based on the present thesis is worth to be carried out in the future from the following aspects:

- In this Ph.D. project, all the insulation tests are performed on a scale cross-arm model. Meanwhile, the test voltage magnitude in a high voltage laboratory is much lower than in the real case. The insulation strength test such as the lightning withstand voltage test on a full-scale cross-arm is more convincing to verify the composite tower insulation strength.

- For the cable as a down-lead, the electrothermal effect of the transmission lines should be considered. According to (4.1) and (4.2), the thermal emission by the phase conductors may disturb the balance of temperature and pressure inside the cross-arm, resulting in changes in the corona onset voltage. It is necessary to do further research regarding the operation temperature and pressure inside the cross-arm, and the corresponding corona inception E-field.

- In this Ph.D. project, the air is insulation dielectric when the cable passes through the hollow cross-arm. To restrict the partial discharge impact, other insulation gases with excellent insulation properties and high arc suppression capability can be the alternatives to fill the hollow cross-arm. Accordingly, the partial discharge characteristic under different filling gas will be changed. The insulation strength of the cross-arm and thermal effect on the materials at overvoltage conditions should be re-investigated.

- In this Ph.D. project, the appropriate material from the existing materials is mainly selected from the perspective of insulation as the filling material. In fact, the weight and mechanical strength should be taken into consideration. It is worth preparing a comprehensive insulation material used as the cross-arm filling material or down-lead cover, which possesses high electrical insulation, thermal stability, lightweight, and mechanical properties. With the upgrading of material properties, the contradiction between high performance and the miniaturization of pylon can be fundamentally solved.

- In the long-term operation, the aging characteristics of the composite material should be studied under the simultaneous action of mechanical load and electrothermal coupling. The life prediction model for this pylon should be built. Based on those studies, the operation and maintenance strategy of the composite pylon can be given.

Bibliography

References

[1] P. N. Mikropoulos and T. E. Tsovilis, "Estimation of lightning incidence to overhead transmission lines," *IEEE Transactions on Power Delivery*, vol. 25, no. 3, pp. 1855–1865, 2010.

[2] J. A. Martinez-Velasco, *Power system transients: parameter determination*. CRC press, 2017.

[3] M. Brignone, F. Delfino, R. Procopio, M. Rossi, and F. Rachidi, "Evaluation of power system lightning performance, part i: Model and numerical solution using the pscad-emtdc platform," *IEEE Transactions on Electromagnetic Compatibility*, vol. 59, no. 1, pp. 137–145, 2017.

[4] H. Ritchie and M. Roser, "Energy production and consumption," https://ourworldindata.org/energy-production-consumption, 2020.

[5] C. Teng, Y. Zhou, L. Zhang, Y. Zhang, X. Huang, and J. Chen, "Improved electrical resistivity-temperature characteristics of insulating epoxy composites filled with polydopamine-coated ceramic particles with positive temperature coefficient," *Composites Science and Technology*, vol. 221, p. 109365, 2022.

[6] Europacable, "Electricity transmission of tomorrow," https://europacable.eu/energy-infrastructure/.

[7] ENTSO-E, "Completing the map power system needs in 2030 and 2040," https://tyndp.entsoe.eu/, 2021.

[8] CIGRE WG 22.14, *High voltage overhead lines. Environmental concerns, procedures, impacts and mitigations*. CIGRE Technical Brochure 147, 1999.

[9] CIGRE B2, *Overhead Lines*. CIGRE Green Books, 2017.

[10] Q. Wang, *Experimental investigation on electrical behaviors of an innovative 400 kV double-circuit composite tower*. PhD thesis, 2018.

[11] BYSTRUP, "Power pylons of the future: European composite pylon," https://www.compositepylon.com/, 2019.

References

[12] Q. Wang, T. Jahangiri, C. L. Bak, F. F. da Silva, and H. Skouboe, "Investigation on shielding failure of a novel 400 kV double-circuit composite tower," *IEEE Transactions on Power Delivery*, vol. 33, no. 2, pp. 752–760, 2018.

[13] M. Sarmento and B. Lacoursiere, "A state of the art overview: Composite utility poles for distribution and transmission applications," in *2006 IEEE/PES Transmission and Distribution Conference and Exposition: Latin America*, 2006, pp. 1–4.

[14] R. Stewart, "Pultruded poles carry power," *Reinforced plastic*, vol. 1, pp. 20–24, 2003.

[15] C. Bhowmik and P. Chakraborti, "Study of strength and stability of a composite transmission tower," *Proceedings of the Institution of Civil Engineers-Engineering and Computational Mechanics*, vol. 173, no. 1, pp. 30–36, 2020.

[16] E. C. Corporation, "Tranmission towers," https://www.ebertcomposites.com/transmission-towers.php.

[17] E. C. Corporation, "Fiberglass utility poles," https://www.ebertcomposites.com/fiberglass-utility-poles.php.

[18] H.-m. Li, S.-c. Deng, Q.-h. Wei, Y.-n. Wu, and Q.-q. Xiang, "Research on composite material towers used in 110 kV overhead transmission lines," in *2010 International Conference on High Voltage Engineering and Application*, 2010, pp. 572–575.

[19] R. T. Inc., "Transmission," https://www.rspoles.com/solutions/portfolio/transmission.

[20] T. Jahangiri, Q. Wang, F. F. Da Silva, and C. L. Bak, *Electrical Design of a 400 kV Composite Tower*. Springer, 2020.

[21] Tennet, "Tennet officially commissions randstad 380 kV north ring," https://www.tennet.eu/tinyurl-storage/detail/tennet-officially-commissions-randstad-380-kv-north-ring/.

[22] Z. G. Datsios, P. N. Mikropoulos, T. E. Tsovilis, and S. I. Angelakidou, "Effect of concentrated tower grounding system modeling on the minimum backflashover current and bfr of 150 and 400 kV overhead transmission lines," in *2018 IEEE International Conference on High Voltage Engineering and Application (ICHVE)*, 2018, pp. 1–4.

[23] Y. Ghugal and U. Salunkhe, "Analysis and design of three and four legged 400 kV steel transmission line towers: Comparative study," *International Journal of Earth Sciences and Engineering*, vol. 4, no. 06, pp. 691–694, 2011.

[24] Z. G. Datsios, A. I. Ioannidis, T. A. Papadopoulos, and T. E. Tsovilis, "A stochastic model for evaluating the lightning performance of a −400 kV HVDC overhead line," *IEEE Transactions on Electromagnetic Compatibility*, vol. 63, no. 5, pp. 1433–1443, 2021.

[25] D. Olason, T. Ebdrup, K. Pedersen, F. Da Silva, and C. L. Bak, "A comparison of the lightning performance of the newly designed eagle pylon and the traditional donau pylon, based on tower geometry," in *International Colloquium on Lightning and Power Systems (CIGRE)*, 2014.

[26] J. A. Martínez-Velasco and F. Castro-Aranda, "Modeling of overhead transmission lines for lightning overvoltage calculations," *Ingeniare. Revista chilena de ingenieria*, vol. 18, no. 1, pp. 120–131, 2010.

[27] M. Selvaraj, S. Kulkarni, and R. Rameshbabu, "Performance analysis of a overhead power transmission line tower using polymer composite material," *Procedia Materials Science*, vol. 5, pp. 1340–1348, 2014.

[28] Creative Composites Group, *Distribution & Transmission Poles Engineered To Outperform*, 1999.

[29] A. Alhayek, A. Syamsir, A. B. M. Supian, F. Usman, M. R. M. Asyraf, and M. A. Atiqah, "Flexural creep behaviour of pultruded GFRP composites cross-arm: A comparative study on the effects of stacking sequence," *Polymers*, vol. 14, 2022.

[30] X. Yang, Q. Wang, H. Wang, S. Zhang, and Z. Peng, "Transient electric field computation for composite cross-arm in 750 kV AC transmission line under lightning impulse voltage," *IEEE Transactions on Dielectrics and Electrical Insulation*, vol. 23, no. 4, pp. 1942–1950, 2016.

[31] C. Zachariades, S. M. Rowland, I. Cotton, V. Peesapati, and D. Chambers, "Development of electric-field stress control devices for a 132 kV insulating cross-arm using finite-element analysis," *IEEE Transactions on Power Delivery*, vol. 31, no. 5, pp. 2105–2113, 2016.

[32] X. Yang, Q. Wang, H. Wang, S. Zhang, and Z. Peng, "Transient electric field computation for composite cross-arm in 750 kV AC transmission line under lightning impulse voltage," *IEEE Transactions on Dielectrics and Electrical Insulation*, vol. 23, no. 4, pp. 1942–1950, 2016.

[33] A. L. Amir, M. R. Ishak, N. Yidris, M. Y. M. Zuhri, and M. R. M. Asyraf, "Potential of honeycomb-filled composite structure in composite cross-arm component: a review on recent progress and its mechanical properties," *Polymers*, vol. 13, no. 8, p. 1341, 2021.

[34] A. Amir, M. Ishak, N. Yidris, M. Zuhri, and M. Asyraf, "Advances of composite cross arms with incorporation of material core structures: Manufacturability, recent progress and views," *Journal of Materials Research and Technology*, vol. 13, pp. 1115–1131, 2021.

[35] Y. Liu, L. Li, H. Liu, M. Zhang, A. Liu, L. Liu, L. Tang, G. Wang, and S. Zhou, "Hollow polymeric microsphere-filled silicone-modified epoxy as an internally insulated material for composite cross-arm applications," *Composites Science and Technology*, vol. 200, p. 108418, 2020.

[36] H. Liu, A. Liu, Y. Liu, L. Li, Z. Xie, Z. Guo, and X. Li, "Electrical and hydrolysis-resistance properties of silicone-modified resin/microsphere syntactic foam for composite cross-arms insulation application," *IEEE Transactions on Dielectrics and Electrical Insulation*, vol. 28, no. 1, pp. 248–256, 2021.

[37] T. Jahangiri, "Electrical design of a new, innovative overhead line transmission tower made in composite materials," 2018.

[38] N. Mavrikakis, P. Mikropoulos, and K. Siderakis, "Evaluation of field-ageing effects on insulating materials of composite suspension insulators," *IEEE Transactions on Dielectrics and Electrical Insulation*, vol. 24, no. 1, pp. 490–498, 2017.

[39] V. Moreno and R. Gorur, "Effect of long-term corona on non-ceramic outdoor insulator housing materials," *IEEE Transactions on Dielectrics and Electrical Insulation*, vol. 8, no. 1, pp. 117–128, 2001.

[40] M. Ehsani, H. Borsi, E. Gockenbach, J. Morshedian, and G. Bakhshandeh, "An investigation of dynamic mechanical, thermal, and electrical properties of housing materials for outdoor polymeric insulators," *European polymer journal*, vol. 40, no. 11, pp. 2495–2503, 2004.

[41] V. Moreno and R. Gorur, "Effect of long-term corona on non-ceramic outdoor insulator housing materials," *IEEE Transactions on Dielectrics and Electrical Insulation*, vol. 8, no. 1, pp. 117–128, 2001.

[42] T. Jahangiri, C. L. Bak, F. da Silva, and B. Endahl, "Electric field and potential distribution in a 420 kV novel unibody composite cross-arm," in *Proceedings of the Nordic Insulation Symposium*, no. 24, 2015.

[43] W. Shaowu, L. Xidong, W. Liming, G. Zhicheng, K. Cholryong, H. Lengceng, S. Qinghe, Y. Jun, W. Jingqin, and C. Xueqi, "Influence of shed profile on the outdoor insulation performance of polymeric insulators," in *Proceedings of the 6th International Conference on Properties and Applications of Dielectric Materials (Cat. No.00CH36347)*, vol. 2, 2000, pp. 785–789 vol.2.

[44] T. IEC, "60815-3. selection and dimensioning of high-voltage insulators intended for use in polluted conditions-part 3: Polymer insulators for a.c." *International Electrotechnical Commission: Worcester, MA, USA*, 2008.

[45] W. Ma, B. Luo, Z. Su, Z. Dang, Z. Guan, X. Liang, U. Astrom, D. Wu, E. Long, and H. Sun, "Preliminary recommendations on the suitable shed profile for HVDC station insulators with silicone rubber housing," in *2006 International Conference on Power System Technology*, 2006, pp. 1–4.

[46] P. N. Mikropoulos and T. E. Tsovilis, "Estimation of the shielding performance of overhead transmission lines: The effects of lightning attachment model and lightning crest current distribution," *IEEE Transactions on Dielectrics and Electrical Insulation*, vol. 19, no. 6, pp. 2155–2164, 2012.

[47] A. Piantini and J. M. Janiszewski, "The use of shield wires for reducing induced voltages from lightning electromagnetic fields," *Electric power systems research*, vol. 94, pp. 46–53, 2013.

[48] P. N. Mikropoulos and T. E. Tsovilis, "Interception probability and shielding against lightning," *IEEE Transactions on Power Delivery*, vol. 24, no. 2, pp. 863–873, 2009.

[49] T. K. Sørensen, J. Holbøll, and S. Mikkelsen, "Composite based EHV AC overhead transmission lines," *Technical University of Denmark, Department of Electrical Engineering*, 2010.

References

[50] Y. Huangfu, S. Wang, G. Wang, W. Xu, and H. Zhang, "Modeling and insulation performance analysis of composite transmission line tower under lightning overvoltage," *IEEE Transactions on Magnetics*, vol. 51, no. 3, pp. 1–4, 2015.

[51] A. R. Hileman, *Insulation coordination for power systems*. CRC Press, 1999.

[52] Y. Huangfu, S. Wang, and X. Tao, "Transient lightning impulse performance analysis for composite transmission line tower," *IEEE Transactions on Electromagnetic Compatibility*, vol. 57, no. 5, pp. 1103–1111, 2015.

[53] Y. Huangfu, S. Wang, X. Tao, S. Wang, B. Yang, G. Wang, and Y. Zhang, "Surge voltage and environmental electromagnetic field analysis for HV composite transmission tower under lightning strokes," in *2014 IEEE International Symposium on Electromagnetic Compatibility (EMC)*, 2014, pp. 445–450.

[54] A. Borghetti, C. A. Nucci, and M. Paolone, "An improved procedure for the assessment of overhead line indirect lightning performance and its comparison with the IEEE Std. 1410 method," *IEEE Transactions on Power Delivery*, vol. 22, no. 1, pp. 684–692, 2006.

[55] V. Cooray, "Calculating lightning-induced overvoltages in power lines. A comparison of two coupling models," *IEEE Transactions on Electromagnetic Compatibility*, vol. 36, no. 3, pp. 179–182, 1994.

[56] M. Paolone, F. Rachidi, A. Borghetti, C. A. Nucci, M. Rubinstein, V. A. Rakov, and M. A. Uman, "Lightning electromagnetic field coupling to overhead lines: Theory, numerical simulations, and experimental validation," *IEEE Transactions on Electromagnetic Compatibility*, vol. 51, no. 3, pp. 532–547, 2009.

[57] J. Paulino, C. Barbosa, I. Lopes, and W. Boaventura, "Assessment and analysis of indirect lightning performance of overhead lines," *Electric Power Systems Research*, vol. 118, pp. 55–61, 2015.

[58] F. Mahmood, N. A. Sabiha, and M. Lehtonen, "Probabilistic risk assessment of MV insulator flashover under combined AC and lightning-induced overvoltages," *IEEE Transactions on Power Delivery*, vol. 30, no. 4, pp. 1880–1888, 2015.

[59] F. Napolitano, F. Tossani, A. Borghetti, and C. A. Nucci, "Lightning performance assessment of power distribution lines by means of stratified sampling Monte Carlo method," *IEEE Transactions on Power Delivery*, vol. 33, no. 5, pp. 2571–2577, 2018.

[60] J. Chen and M. Zhu, "Calculation of lightning flashover rates of overhead distribution lines considering direct and indirect strokes," *IEEE Transactions on Electromagnetic Compatibility*, vol. 56, no. 3, pp. 668–674, 2014.

[61] T. Jahangiri, Q. Wang, C. L. Bak, F. F. da Silva, and H. Skouboe, "Electric stress computations for designing a novel unibody composite cross-arm using finite element method," *IEEE Transactions on Dielectrics and Electrical Insulation*, vol. 24, no. 6, pp. 3567–3577, 2017.

References

[62] M. R. Alemi and K. Sheshyekani, "Wide-band modeling of tower-footing grounding systems for the evaluation of lightning performance of transmission lines," *IEEE Transactions on Electromagnetic Compatibility*, vol. 57, no. 6, pp. 1627–1636, 2015.

[63] CIGRE WG C4.23, "Procedures for estimating the lightning performance of transmission lines – new aspects," 2021.

[64] J. Takami and S. Okabe, "Observational results of lightning current on transmission towers," *IEEE Transactions on Power Delivery*, vol. 22, no. 1, pp. 547–556, 2007.

[65] T. Jahangiri, C. L. Bak, F. F. da Silva, and B. Endahl, "Determination of minimum air clearances for a 420 kV novel unibody composite cross-arm," in *2015 50th International Universities Power Engineering Conference (UPEC)*, 2015, pp. 1–6.

[66] J. Wang, Z. Peng, H. Wu, H. Deng, H. Liu, and C. Wang, "Electric field calculation and grading ring design for 330 kV terminal tower with composite cross-arms," in *2016 IEEE International Conference on Dielectrics (ICD)*, vol. 1, 2016, pp. 346–349.

[67] K. Yin, G. Zhu, Y. Shi, H. Zhang, F. F. da Silva, C. L. Bak, and X. Chen, "Feasibility of cable through a hollow cross-arm as down-lead for a 400 kV y-shaped composite pylon," *Electric Power Systems Research*, 2022.

[68] M. Brignone, F. Delfino, R. Procopio, M. Rossi, and F. Rachidi, "Evaluation of power system lightning performance—part ii: Application to an overhead distribution network," *IEEE Transactions on Electromagnetic Compatibility*, vol. 59, no. 1, pp. 146–153, 2017.

[69] A. Yamanaka, N. Nagaoka, Y. Baba, M. Saito, and T. Miki, "Lightning strike to a tall grounded object: Part 1. circuit modeling with direction dependence," *IEEE Transactions on Electromagnetic Compatibility*, vol. 61, no. 3, pp. 727–735, 2019.

[70] W. Jia and Z. Xiaoqing, "Double-exponential expression of lightning current waveforms," in *The 2006 4th Asia-Pacific Conference on Environmental Electromagnetics*, 2006, pp. 320–323.

[71] F. H. Silveira and S. Visacro, "Lightning performance of transmission lines: Impact of current waveform and front-time on backflashover occurrence," *IEEE Transactions on Power Delivery*, vol. 34, no. 6, pp. 2145–2151, 2019.

[72] A. Borghetti, F. Napolitano, C. A. Nucci, and F. Tossani, "Influence of the return stroke current waveform on the lightning performance of distribution lines," *IEEE Transactions on Power Delivery*, vol. 32, no. 4, pp. 1800–1808, 2017.

[73] R. B. A. K. Berger and H. Kroninger, "Parameters of the lightning stroke," *ELECTRA*, pp. 23–37, 1975.

[74] R. B. Anderson, "Lightning parameters for engineering application," *Electra*, vol. 69, pp. 65–102, 1980.

[75] CIGRE WG C4.407, *Lightning parameters for engineering application*. CIGRE Technical Brochure 549, 2013.

References

[76] M. A. Sargent and M. Darveniza, "Tower surge impedance," *IEEE Transactions on Power Apparatus and Systems*, vol. PAS-88, no. 5, pp. 680–687, 1969.

[77] C. F. Wagner and A. R. Hileman, "A new approach to the calculation or the lightning perrormance or transmission lines iii-a simplified method: Stroke to tower," *Transactions of the American Institute of Electrical Engineers. Part III: Power Apparatus and Systems*, vol. 79, no. 3, pp. 589–603, 1960.

[78] T. Hara and O. Yamamoto, "Modelling of a transmission tower for lightning-surge analysis," *IEE Proceedings-Generation, Transmission and Distribution*, vol. 143, no. 3, pp. 283–289, 1996.

[79] M. Ishii, T. Kawamura, T. Kouno, E. Ohsaki, K. Shiokawa, K. Murotani, and T. Higuchi, "Multistory transmission tower model for lightning surge analysis," *IEEE Transactions on Power Delivery*, vol. 6, no. 3, pp. 1327–1335, 1991.

[80] K. Yin, M. Ghomi, H. Zhang, F. F. da Silva, C. L. Bak, and Q. Wang, "Lightning transient response of bifurcation structure pylon and its empirical expression with high accuracy and general application," *International Journal of Electrical Power & Energy Systems*, 2022.

[81] X. Zhang, Y. Zhang, and X. Xiao, "An improved approach for modeling lightning transients of wind turbines," *International Journal of Electrical Power & Energy Systems*, vol. 101, pp. 429–438, 2018.

[82] K. Yin, M. Ghomi, F. F. Da Silva, C. L. Bak, H. Zhang, Q. Wang, and H. Skouboe, "Lightning performance and formula description of a y-shaped composite pylon considering the effect of tower-footing impedance," in *2021 35th International Conference on Lightning Protection (ICLP) and XVI International Symposium on Lightning Protection (SIPDA)*, vol. 1, 2021, pp. 1–6.

[83] K. Yin, M. Ghomi, H. Zhang, F. F. da Silva, C. L. Bak, Q. Wang, and H. Skouboe, "The design and optimization of the down-lead system for a novel 400 kV composite pylon," *IEEE Transactions on Power Delivery*, pp. 1–11, 2022.

[84] A. Deri, G. Tevan, A. Semlyen, and A. Castanheira, "The complex ground return plane a simplified model for homogeneous and multi-layer earth return," *IEEE Transactions on Power Apparatus and Systems*, vol. PAS-100, no. 8, pp. 3686–3693, 1981.

[85] J. R. Carson, "Wave propagation in overhead wires with ground return," *The Bell System Technical Journal*, vol. 5, no. 4, pp. 539–554, 1926.

[86] A. Mousa, "The soil ionization gradient associated with discharge of high currents into concentrated electrodes," *IEEE Transactions on Power Delivery*, vol. 9, no. 3, pp. 1669–1677, 1994.

[87] M. Ghomi, H. Zhang, C. L. Bak, F. F. da Silva, and K. Yin, "Integrated model of transmission tower surge impedance and multilayer grounding system based on full-wave approach," *Electric Power Systems Research*, vol. 198, p. 107355, 2021.

References

[88] L. Grcev, "Modeling of grounding electrodes under lightning currents," *IEEE Transactions on Electromagnetic Compatibility*, vol. 51, no. 3, pp. 559–571, 2009.

[89] "Ieee guide for improving the lightning performance of transmission lines," *IEEE Std 1243-1997*, pp. 1–44, 1997.

[90] D. Kind, M. Kurrat, and T. H. Kopp, "Voltage-time characteristics of air gaps and insulation coordination — survey of 100 years research," in *2016 33rd International Conference on Lightning Protection (ICLP)*, 2016, pp. 1–8.

[91] P. Chowdhuri, A. Baker, G. Carrara, W. Chisholm, K. Feser, S. Grzybowski, A. Lux, and F. Newnam, "Review of research on nonstandard lightning voltage waves," *IEEE Transactions on Power Delivery*, vol. 9, no. 4, pp. 1972–1981, 1994.

[92] T. Shindo and T. Suzuki, "A new calculation method of breakdown voltage-time characteristics of long air gaps," *IEEE Transactions on Power Apparatus and Systems*, vol. PAS-104, no. 6, pp. 1556–1563, 1985.

[93] F. Rizk, "A model for switching impulse leader inception and breakdown of long air-gaps," *IEEE Transactions on Power Delivery*, vol. 4, no. 1, pp. 596–606, 1989.

[94] K. Yin, M. Ghomi, F. F. Silva, C. L. Bak, H. Zhang, and Q. Wang, "The effect of frequency-dependent soil electrical parameters on the lightning response of a 'Y-'shaped composite pylon for 400 kV transmission lines," 2021.

[95] T. Jahangirl, C. L. Bak, F. M. F. da Silva, B. Endahl, and J. Holbøll, "Assessment of lightning shielding performance of a 400 kV double-circuit fully composite pylon," in *Cigré Session 2016*, 2016, pp. C4–205.

[96] J. Gholinezhad and R. Shariatinasab, "Time-domain modeling of tower-footing grounding systems based on impedance matrix," *IEEE Transactions on Power Delivery*, vol. 34, no. 3, pp. 910–918, 2019.

[97] V. Dan, "A rational choice of bundle conductors configuration," in *Proceedings of 1998 International Symposium on Electrical Insulating Materials. 1998 Asian International Conference on Dielectrics and Electrical Insulation. 30th Symposium on Electrical Insulating Ma*, 1998, pp. 349–354.

[98] S. Ilhan and A. Ozdemir, "380 kV corona ring optimization for AC voltages," *IEEE Transactions on Dielectrics and Electrical Insulation*, vol. 18, no. 2, pp. 408–417, 2011.

[99] E. Kuffel, W. Zaengl, and J. Kuffel, "High voltage engineering fundamentals second edition," in *Reprinted*, 1986.

[100] J. Yang, R. Huang, and D. Zhang, "A field-circuit coupled method to accurately determine intrinsic complex permittivity of XLPE insulation material," *IEEE Transactions on Dielectrics and Electrical Insulation*, vol. 15, no. 2, pp. 334–341, 2008.

[101] V. Peesapati, C. Zachariades, Q. Li, S. M. Rowland, I. Cotton, P. R. Green, F. Allison, and D. Chambers, "3D electric field computation of a composite cross-arm," in *2012 IEEE International Symposium on Electrical Insulation*, 2012, pp. 464–468.

References

[102] S. Ivashov, A. Zhuravlev, V. Razevig, M. Chizh, T. Bechtel, L. Capineri, and B. Thomas, "Frequency influence in microwave subsurface holography for composite materials testing," in *2018 17th International Conference on Ground Penetrating Radar (GPR)*, 2018, pp. 1–4.

[103] J. María and D. CAPELLA, "Study of the behaviour of a n-metal cable screen subject to an adiabatic short-circuit," in *9th Int. Conf. Insul. Power Cables*, 2015, pp. 1–4.

[104] S. S. M. Ghoneim, M. Ahmed, and N. A. Sabiha, "Transient thermal performance of power cable ascertained using finite element analysis," *Processes*, vol. 9, no. 3, p. 438, 2021.

[105] A. B. MORGAN, "Fire risks with fiber-reinforced polymer (FRP) composites," https://dsiac.org/articles/fire-risks-with-fiber-reinforced-polymer-frp-composites/, 2019.

[106] CIGRE WG 22.12, "The thermal behaviour of overhead conductors," 2002.

[107] E. Tuncer, I. Sauers, D. R. James, and A. R. Ellis, "Electrical insulation characteristics of glass fiber reinforced resins," *IEEE Transactions on Applied Superconductivity*, vol. 19, no. 3, pp. 2359–2362, 2009.

[108] H. Zhang, M. Ghomi, Q. Wang, F. F. da Silva, C. L. Bak, K. Yin, and H. Skouboe, "Comparison of backflashover performance between a novel composite pylon and metallic towers," *Electric Power Systems Research*, vol. 196, p. 107263, 2021.

[109] P. Malicki, A. Mackow, and M. Kizilcay, "Estimating the lightning performance of a multi-circuit transmission tower," in *2016 33rd International Conference on Lightning Protection (ICLP)*, 2016, pp. 1–4.

[110] S. Hedtke, P. Xu, M. Pfeiffer, B. Zhang, J. He, and C. M. Franck, "HVDC corona current characteristics and audible noise during wet weather transitions," *IEEE Transactions on Power Delivery*, vol. 35, no. 2, pp. 1038–1047, 2020.

[111] B. Zhang and F. Xiao, "Simulation of impulse corona on HVDC overhead transmission lines with background DC space charges by method of characteristics," *IEEE Transactions on Power Delivery*, vol. 37, no. 3, pp. 2032–2039, 2022.

[112] P. N. Mikropoulos and V. N. Zagkanas, "Threshold inception conditions for positive DC corona in the coaxial cylindrical electrode arrangement under variable atmospheric conditions," *IEEE Transactions on Dielectrics and Electrical Insulation*, vol. 22, no. 1, pp. 278–286, 2015.

[113] J.-R. Riba, W. Larzelere, and J. Rickmann, "Voltage correction factors for air-insulated transmission lines operating in high-altitude regions to limit corona activity: a review," *Energies*, vol. 11, no. 7, p. 1908, 2018.

[114] H. K. Meyer, F. Mauseth, M. Husoy, and A. Pedersen, "Surface charging of dielectric barriers under positive lightning impulse stress," in *2017 IEEE Conference on Electrical Insulation and Dielectric Phenomenon (CEIDP)*, 2017, pp. 802–806.

References

[115] Y.-P. Liu, S.-H. You, F.-C. Lu, Q.-F. Wan, X.-M. Bian, and L.-M. Wang, "500 kV EHV bundle conductors' corona onset voltage calculation and analysis in corona cage at different altitudes," *IEEE Transactions on Power Delivery*, vol. 27, no. 4, pp. 2090–2097, 2012.

[116] Q. Li, S. M. Rowland, and R. Shuttleworth, "Calculating the surface potential gradient of overhead line conductors," *IEEE Transactions on Power Delivery*, vol. 30, no. 1, pp. 43–52, 2015.

[117] F. W. Peek, "The law of corona and the dielectric strength of air-IV the mechanism of corona formation and loss," *Transactions of the American Institute of Electrical Engineers*, vol. XLVI, pp. 1009–1024, 1927.

[118] R. Waters and W. Stark, "Characteristics of the stabilized glow discharge in air," *Journal of Physics D: Applied Physics*, vol. 8, no. 4, p. 416, 1975.

[119] T. Gallagher and I. Dudurych, "Model of corona for an emtp study of surge propagation along HV transmission lines," *IEE Proceedings-Generation, Transmission and Distribution*, vol. 151, no. 1, pp. 61–66, 2004.

[120] C. L. Bak, W. Wiechowski, K. Søgaard, and S. D. Mikkelsen, "Analysis and simulation of switching surge generation when disconnecting a combined 400 kV cable/overhead line with shunt reactor," *IPST2007*, 2001.

[121] R. R. Annadi and C. S. Patsa, "Statistical switching overvoltages of 1200 kV UHV AC transmission line," *Journal of The Institution of Engineers (India): Series B*, vol. 103, no. 1, pp. 189–195, 2022.

[122] A. K. Pathania and I. Kour, "Role of controlled switching on transmission line for SOV mitigation-a review," *International Journal of Pure and Applied Mathematics*, vol. 118, no. 16, pp. 579–597, 2018.

[123] H.-T. Wu, C.-Q. Jiao, X. Cui, X.-F. Liu, and J.-F. Ji, "Transient electromagnetic disturbance induced on the ports of intelligent component of electronic instrument transformer due to switching operations in 500 kV GIS substations," *IEEE Access*, vol. 5, pp. 5104–5112, 2017.

[124] R. Wang, Y. Yang, S. Chen, H. Jiang, and P. Martin, "Power calculation of pulse power-driven DBD plasma," *IEEE Transactions on Plasma Science*, vol. 49, no. 7, pp. 2210–2216, 2021.

[125] H. Conrads and M. Schmidt, "Plasma generation and plasma sources," *Plasma Sources Science and Technology*, vol. 9, no. 4, p. 441, 2000.

[126] F. A. Rizk, "Negative impulse ground wire corona parameters for backflash evaluation of high voltage transmission lines," *IEEE Transactions on Power Delivery*, pp. 1–1, 2021.

[127] F. Xiao and B. Zhang, "Transient overvoltage on HVDC overhead transmission lines with background DC space charges and impulse corona," *IEEE Transactions on Power Delivery*, vol. 36, no. 5, pp. 2921–2928, 2021.

[128] E. Stracqualursi, R. Araneo, and A. Andreotti, "The impact of different corona models on FD algorithms for the solution of multiconductor transmission lines equations," *High Voltage*, vol. 6, no. 5, pp. 822–835, 2021.

[129] T. Tanaka, "Internal partial discharge and material degradation," *IEEE Transactions on Electrical Insulation*, no. 6, pp. 899–905, 1986.

[130] J. He, X. Zhang, P. Yang, S. Chen, and R. Zeng, "Attenuation and deformation characteristics of lightning impulse corona traveling along bundled transmission lines," *Electric power systems research*, vol. 118, pp. 29–36, 2015.

[131] N. Spyrou and J. d. Amorim, "Atmospheric pressure DBD low-temperature plasma reactor for the treatment of sugarcane bagasse," *IEEE Transactions on Plasma Science*, vol. 47, no. 3, pp. 1583–1592, 2019.

[132] G.-M. Xu, Y. Ma, and G.-J. Zhang, "DBD plasma jet in atmospheric pressure argon," *IEEE Transactions on Plasma Science*, vol. 36, no. 4, pp. 1352–1353, 2008.

[133] H. Kim and F. Shi, "Thickness dependent dielectric strength of a low-permittivity dielectric film," *IEEE Transactions on Dielectrics and Electrical Insulation*, vol. 8, no. 2, pp. 248–252, 2001.

[134] D. R. James, I. Sauers, A. R. Ellis, E. Tuncer, K. Tekletsadik, and D. W. Hazelton, "Breakdown and partial discharge measurements of some commonly used dielectric materials in liquid nitrogen for hts applications," *IEEE Transactions on Applied Superconductivity*, vol. 17, no. 2, pp. 1513–1516, 2007.

[135] C. Muliang, W. Jian, D. Yeqiang, W. Huayun, and W. Ziqiang, "A new method on calculation of lightning trip rate of 35 kV or under overhead distribution lines in ungrounded neutral point system," in *2018 IEEE International Conference on High Voltage Engineering and Application (ICHVE)*, 2018, pp. 1–4.

[136] S. Sekioka, M. I. Lorentzou, and N. D. Hatziargyriou, "Approximate formulas for terminal voltages on the grounding conductor," *IEEE Transactions on Electromagnetic Compatibility*, vol. 56, no. 2, pp. 444–453, 2014.

[137] J. Lei, S. Liang, Z. Shi-pu, X. Peng, S. Donghui, and S. Wei, "Investigation on the lightning withstand level of transmission line considering power frequency voltage," *High Voltage Engineering*, vol. 32, no. 11, pp. 111–114, 2006.

[138] Q. Wang, X. Liang, Y. Shen, S. Liu, Z. Zuo, and Y. Gao, "Lightning flashover characteristics of a full-scale AC 500 kV transmission tower with composite cross arms," *Engineering*, 2022.

[139] H. Hu, M. Fang, Y. Zhang, L. Jing, and F. Hu, "Dynamic lightning protection method of electric power systems based on the large data characteristics," *International Journal of Electrical Power & Energy Systems*, vol. 128, p. 106728, 2021.

[140] I. Gonos, L. Ekonomou, F. Topalis, and I. Stathopulos, "Probability of backflashover in transmission lines due to lightning strokes using Monte-Carlo simulation," *International journal of electrical power & energy systems*, vol. 25, no. 2, pp. 107–111, 2003.